**STATE UNIVERSITY OF PONTA GROSSA
SECTOR OF AGRICULTURAL SCIENCES AND TECHNOLOGY
POSTGRADUATE PROGRAM IN ENGINEERING AND
MATERIALS SCIENCE**

ANA LUÍSA TERASAWA SENRA

IN SITU STUDY OF AISI 304 AND AISI 430 STAINLESS STEEL USING

SYNCHROTRON LIGHT

**PONTA GROSSA
2019**

ANA LUÍSA TERASAWA SENRA

IN SITU STUDY OF AISI 304 AND AISI 430 STAINLESS STEEL USING SYNCHROTRON LIGHT

Dissertation presented as a partial requirement to obtain the title of Master in Engineering and Materials Science at the State University of Ponta Grossa.
Concentration Area: Materials Processing and Characterisation.

Advisor:
Prof Dr Osvaldo Mitsuyuki Cintho

Co-advisor:
Dr John Jairo Hoyos Quintero

PONTA GROSSA
2019

Ficha Catalográfica
Elaborada pelo Setor de Tratamento da Informação BICEN/UEPG

ANA LUÍSA TERASAWA SENRA

IN SITU STUDY OF AISI 304 AND AISI 430 STAINLESS STEEL USING SYNCHROTRON LIGHT

Dissertation presented as a partial requirement to obtain the title of Master in Engineering and Materials Science at the State University of Ponta Grossa. Concentration Area: Materials Processing and Characterisation.

Ponta Grossa, Twenty-ninth of July 2019.
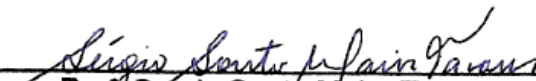
_____
Prof. Osvaldo Mitsuyuki Cintho (Advisor)
Doctor of Metallurgical Engineering
State University of Ponta Grossa (UEPG)

_____
Prof. Márcio Ferreira Hupalo
Doctor of Metallurgical Engineering
State University of Ponta Grossa (UEPG)

_____
Prof. Sérgio Souto Maior Tavares
Doctor of Metallurgical and Materials Engineering
Fluminense Federal University (UFF)

I dedicate to my mother, Gisele, for encouraging and supporting me, and for making my dreams come true; and to my star, my father, Ailton, who is no longer present in my life, but is my spiritual foundation.

ACKNOWLEDGEMENTS

"No matter what are the obstacles and difficulty. If we are possessed of an unshakable determination, we can overcome them regardless of the circumstances".

Unknown Author

ABSTRACT

The cryogenic deformation has been extensively studied due to the possible improvements of generated properties, such as an increase in mechanical resistance and ductility. The gains occur as a consequence of the partial suppression of dynamic recovery, which produces microstructural refining and increases microstrain, due to an increase of internal defect density. Two stainless steels, AISI 304 and AISI 430, were used for the study under four strain-rates. The XTMS experimental station allowed tensile tests simultaneously to X-ray diffraction, providing *in situ* information of phenomena and microstructural changes that occur during deformation. The analysis of fracture surfaces was essential to understand the ductile-brittle transition phenomenon on AISI 430 steel, which indicated conditions at the threshold of the ductile-brittle transition. An additional strain rate was used to overcome the transition point. The mechanical results showed that the decrease in temperature has a similar effect on the increase in strain rate, and these changes generated an increase in tensile strength for AISI 430 steel. However, the four initials strain rates, there was no significant impact on the mechanical result, but when the fracture surface was analysed, there was a competition between the cleavage and ductile fracture mechanisms. For the AISI 304 steel, at cryogenic temperature, it was possible to verify a change in the shape of the stress-strain curve, with loss of ductility and increase of resistant, being an effect of the martensitic transformation. For the AISI 304 steel, phase transformation at room temperature occurs with higher strain than for the cryogenic temperature, due to the effect of the adiabatic heating, which stabilises austenite. The microstrain in the austenite planes decreased during the plastic deformation, indicating the presence of dynamic recovery. For the AISI 430, the crystallite size indicated that at cryogenic temperature there was greater microstructural refining.

Keywords: Cryogenic deformation, martensitic transformation, ductile-brittle transition, strain rate, X-ray diffraction.

RESUMO

A deformação criogênica tem sido amplamente estudada devido às possíveis melhorias de propriedades geradas, como aumento de resistência mecânica e ductilidade. As melhorias ocorrem em consequência da supressão parcial da recuperação dinâmica, a qual gera refino microestrutural e aumento da microdeformação, os quais ocorrem devido ao aumento da densidade de defeitos internos. Para o estudo foram utilizados dois aços inoxidáveis, AISI 304 e AISI 430, sob quatro taxas de deformação. A estação experimental XTMS do LNLS do CNPEM permitiu a realização de testes de tração simultaneamente à difração de raios X, fornecendo informações *in situ* dos fenômenos e alterações microestruturais que ocorrem durante a deformação. As análises das superfícies de fratura foram essenciais para entender o fenômeno de transição dúctil frágil no AISI 430, o que indicou condições no limiar da transição dúctil-frágil. Uma taxa de deformação adicional foi utilizada a fim de ultrapassar o ponto de transição. Os resultados mecânicos mostraram que a redução na temperatura tem efeito similar ao aumento na taxa de deformação, sendo que estas alterações geraram um aumento na resistência à tração para o aço AISI 430. Entretanto, as quatro taxas de deformação utilizadas inicialmente não apresentaram grande impacto no resultado mecânico, mas quando analisada a superfície de fratura viu-se uma competição entre os mecanismos dúcteis de fratura e clivagem. Para o aço AISI 304, em temperatura criogênica, foi possível verificar a mudança na forma da curva de tensão-deformação, havendo perda de ductilidade e aumento de resistência, sendo um efeito da transformação martensítica. A transformação de fase em temperatura ambiente ocorre com maiores deformações do que para a temperatura criogênica, sendo esse o efeito do aquecimento adiabático o qual estabiliza a austenita. A microdeformação nos planos da austenita reduziu durante a deformação plástica, indicando a presença de recuperação dinâmica. Para o AISI 430, o tamanho de cristalito indicou que em temperatura criogênica houve maior refino microestrutural.

Palavras-chave: Deformação criogênica, transformação martensítica, transição dúctil-frágil, taxa de deformação, difração de raios X.

FIGURES LIST

TABLES LIST

EQUATIONS LIST

ACRONYMS AND TERMS LIST

AISI   American Iron and Steel Institute

BCC   Body-Centred Cubic Structure

BCT   Body-Centred Tetragonal Structure

CNPEM   Brazilian Centre for Research in Energy and Materials, from portuguese *Centro Nacional de Pesquisa em Energia e Materiais*

CPM   Metals Characterisation and Processing Laboratory, from portuguese *Caracterização e Processamento de Metais*

CT   Cryogenic Temperature

DBT   Ductile-Brittle Transition

DSI   Dynamic System Inc.

FCC   Face-Centred Cubic Structure

HCP   Hexagonal Close-Packed Structure

JCPDS   Joint Committee on Powder Diffraction Standards

LEDS   Low-Energy Dislocations Structures

LNLS   Brazilian Synchrotron Light Laboratory, from portuguese *Laboratório Nacional de Luz Síncrotron*

LNNano   Brazilian Nanothecnology Laboratory, from portuguese *Laboratório Nacional de Nanotecnologia*

MTR   Martensitic Transformation Rate

MVT   Martensite Volume Fraction

RT   Room Temperature

SEM   Scanning Electron Microscopy

SEM/FEG   Scanning Electron Microscopy with Field Emission Gun

SFE   Stacking Fault Energy

SPD   Severe Plastic Deformation

TRIP	Transformation Induced Plasticity
TWIP	Twinning Induced Plasticity
UTS	Ultimate Tensile Strength
UVX	Name of synchrotron light ring installed in Campinas. UVX represents the spectral range that ring encompasses, from ultraviolet to soft X rays
XRD1	A light line of Synchrotron ring, where the XTMS station is installed
XTMS	X-ray Scattering and Thermo-Mechanical Simulation Station. Station of the XRD1 line of Synchrotron ring, where the Gleeble® equipment is installed
WHR	Work-Hardening Rate
%RA	Percentage of Reduction in Area

SUMMARY

1 INTRODUCTION

The stainless steels are known due to the high corrosion resistance when compared to other types of steel. They are ferrous alloys that possess chrome quantities higher than 10.5%, which is responsible for the formation of the passivation layer making them "stainless". In these steels, it is possible to add other alloying elements in order to obtain specific characteristics. Such as adding carbon to improve sensitisation, which improves creep resistance, and adding sulphur or selenium to improve machinability.

Aside from the corrosion resistance, stainless steels are materials that show high strength, such as high stress, strain, ductility and resilience. They are widely marketed, having a range of applications, such as aerospace, automotive, chemical, petrochemical, food and pharmaceutical industries.

Several researchers in the last years have studied the cryogenic deformation because the processing of metals under this condition can provide improvement of resistance and/or ductility. Thus, allowing metals that are less commercially known and, in a certain way, cheap, to show improvement in properties. For the better improvement and understanding of processing, it is needed to analyse the processing parameters, such as strain and temperature.

The research group in cryogenic deformation of metallic materials of the Materials Engineering Department (DEMa) from the State University of Ponta Grossa (UEPG), which is directed by Professor Dr Osvaldo Mitsuyuki Cintho, is ongoing years of study of the behaviour and property improvement obtained through plastic deformation at low temperatures. Studies involve pure materials, like copper, aluminium and silver, and stainless steels, such as austenitic, ferritic and duplex; those being processed by rolling, uniaxial traction, equal channel angular extrusion and high-energy milling. It was aimed to improve the understanding of the phenomena involved in plastic deformation, like dynamic recovery, microstrain, crystallite size and the influence of variables such as stacking fault energy and temperature.

In this work, sought to analyse effects of the cryogenic deformation in AISI 304 and 430 stainless steel and also the influence of strain rate. These steels are widely known commercially and show corrosion resistance, as well as being able to have their mechanical properties enhanced due to the processing route. Some

studies aim to analyse these phenomena; however, they were done through conventional techniques, where the analysis is made after deformation, which might influence the time of recovery mechanisms.

However, the experimental station XTMS (X-ray Scattering and Thermo-Mechanical Simulation), connected to the synchrotron UVX of the LNLS (Brazilian Synchrotron Light Laboratory) of CNPEM (Brazilian Centre for Research in Energy and Materials), allows that thermo-mechanical tests can be done simultaneously with the X-ray diffraction measurements. Enabling the *in situ* studies during plastic deformation, obtaining the knowledge of the phenomena, with more precise results, reducing the information loss.

The synchrotron radiation provides a bigger intensity and parallelism of the incident beam, showing precise and highly reliable results, as well as providing fast data gathering, with three-second intervals. The information contained in the X-ray diffraction profiles for the AISI 304 and 430, such as crystallite size and microstrain were analysed in order to understand the influence of the strain rate and deformation temperature. Additional analysis complemented the obtained results at the XTMS station, like fracture surface analysis through field emission gun scanning electron microscopy (SEM-FEG) and optical microscopy.

2 OBJECTIVES

2.1 GENERAL OBJECTIVES

- Analyse the microstructural and mechanical behaviour of AISI 304 and 430 steel deformed under different strain rates at room and cryogenic temperatures.

2.2 SPECIFIC OBJECTIVES

- Study the effect of decreasing temperature in the AISI 304 and 430 stainless steel;

- Study the impact of the change in strain rate in the AISI 304 and 430 stainless steel;

- Evaluate the microstructural changes *in situ* through X-ray diffraction;

- Evaluate the fracture mechanisms that operate in the studied steels according to the temperature and strain rate changes;

- Analyse the temperature and strain rate effect on the martensitic transformation in the AISI 304 stainless steel;

- Analyse the effect of strain rate and temperature on the ductile-brittle transition on the AISI 430 stainless steel.

3 LITERATURE REVIEW

3.1 STAINLESS STEELS

Stainless steels are widely used in environments which require corrosion resistance, such as marine, automobile, food and pharmaceutical industries. The applications include a range of extremely different uses, including pressure vessels, heat exchangers, industrial oil pipes, chemical processing components, paper and cellulose industry components, furnace and boiler parts used in fossil fuel energy plants[1-3].

The oxidation resistance is the property that differentiates the stainless steels from other steels, the property occurs due to the chrome addition. Chrome grants passivation to iron alloys when presented in quantities higher than 10.5%. The passivation is granted through the formation of a film of an oxide, which is rich in chrome, invisible, and adherent, that forms in the presence of oxygen. Chrome added by itself in an alloy tends to close the austenitic field, favouring ferrite formation. However, when chrome is added in a steel containing nickel, there is a delay in the ferrite-austenite transformation kinetic, favouring the retention of retained austenite at room temperature. In stainless steels, carbon is usually presented in quantities that vary from 0.03% to 1.00% [1-6].

Other elements can be added in order to improve the efficiency of chrome in the formation of the passivation layer. Molybdenum, together with chrome, is very efficient in stabilising the passive film in the presence of chlorides. Nickel is an austenite phase stabiliser, and manganese, in low quantities, when associated with nickel is capable of improving the stabilisation. In small quantities, carbon improves the material's quenching capacity and grants mechanical strength when the steel is applied in high temperatures. However, carbon contents higher than the austenite solubility is harmful to the corrosion resistance, that is because carbon reacts with chrome, creating carbides and lowering chrome content in neighbouring regions, reducing corrosion resistance in these regions. Nitrogen is beneficial to austenitic stainless steels because it slows down the σ phase of chrome-molybdenum and hardens the steel; on the other hand, nitrogen is harmful to the mechanical strength properties of the ferritic stainless-steel class [6,7].

One of the most used classifications for stainless steels is based in the microstructure shown by them at room temperature and in the type of thermal treatment undergone to obtain the structure. In this way, we have the stainless-steel groups: martensitic, ferritic, austenitic, duplex and precipitation hardened. Depending on the chemical composition of the steel, the microstructure can be composed by the austenite and/or ferrite phases is that when there are both present, we have a duplex steel. The martensite phase occurs due to the chemical composition of the martensitic stainless steels, which falls in the austenitic field at temperatures around 1000º C and transforms into martensite on cooling. These steels have high hardenability, so the martensitic transformation occurs by oil or even air cooling. And the last class of stainless steels is characterised by the presence of precipitates that harden the material [2,3,8].

The mechanical properties and corrosion resistance differ between each of the stainless steels; in this way, one needs to evaluate the requirement for the application to select the correct steel. Typically, stainless steels are chosen due to the characteristics that they show, such as corrosion resistance, mechanical strength and ductility at room temperature, abrasion resistance, magnetic properties, thermal conductivity, electric resistivity, hardness, oxidation resistance and if they are adequate for cleaning procedures [6,9].

The stainless steels are often designated by the numbering system of the American Iron and Steel Institute (AISI), being that the majority of the stainless-steel classes have a three-digit designation: the series 200 and 300 are usually austenitic stainless steels, whereas the series 400 are ferritic or martensitic. Some numbering presents a suffix of one or two letters that show a specific composition modification[2,3].

3.1.1 Austenitic Stainless Steels

Austenitic stainless steels constitute the more prominent family of the stainless steels in terms of the number of alloys and uses. They present face-centred cubic structure (FCC), due to the use of austenitizers, such as nickel, manganese and nitrogen. Sulphur or selenium can be used to improve machinability. The chrome content generally goes from 16 to 26%; nickel, until around 35%; and manganese, until 15%. The steels from the 2xx series contain nitrogen, nickel until 7%, and manganese from 4 to 15.5%. The 3xx series contain bigger quantities of nickel and

manganese until 2%. Small amounts of nitrogen improve the mechanical strength of austenitic stainless steels, and the addition of manganese in some steels is used to substitute part of nickel. Table 1 presents the chemical compositions of some austenitic stainless steels from series 3xx [3,6,9].

Table 1 - Composition (% in weight) of some standard 3xx series austenitic stainless steels

	C	Mn	Si	Cr	Ni	P	S	Others
301	0.15	2.00	1.00	16.0-18.0	6.0-8.0	0.045	0.03	...
302	0.15	2.00	1.00	17.0-19.0	8.0-10.0	0.045	0.03	...
303	0.15	2.00	1.00	17.0-19.0	8.0-10.0	0.20	0.15 min	0.6 Mo
304	0.08	2.00	1.00	18.0-20.0	8.0-10.5	0.045	0.03	...
304H	0.04-0.10	2.00	1.00	18.0-20.0	8.0-10.5	0.045	0.03	...
304L	0.03	2.00	1.00	18.0-20.0	8.0-12.0	0.045	0.03	...
310	0.25	2.00	1.50	24.0-26.0	19.0-22.0	0.045	0.03	...
316	0.08	2.00	1.00	16.0-18.0	10.0-14.0	0.045	0.03	2.0-3.0 Mo
316L	0.03	2.00	1.00	16.0-18.0	10.0-14.0	0.045	0.03	2.0-3.0 Mo
321	0.08	2.00	1.00	17.0-19.0	9.0-12.0	0.045	0.03	5 x %C min Ti
347	0.08	2.00	1.00	17.0-19.0	9.0-13.0	0.045	0.03	10 x %C min Nb

Source: Adapted from Washco and Aggen (1990) [6].

The austenitic class is, essentially, non-magnetic in the annealed condition; if there were some δ ferrite in the microstructure, the material would exhibit some

magnetism. However, if there is phase transformation (austenite -> martensite), the α'-martensite is ferromagnetic and than would increase magnetism level [3,6-7].

These alloys generally show excellent cryogenic properties and satisfactory resistance at high temperatures. The austenitic stainless steels can be hardened through cold work, being that metastable austenitic stainless steels can develop bigger resistances and hardness than other stable types for certain deformations. The high work hardening of austenitic stainless steel is due to the low stacking-fault energy (SFE), close to 20mJ/m^2; its plastic deformation is characterised by partial dislocation dissociation and wide stacking fault formation [6-11].

The annealed AISI 304 stainless steel when submitted to tensile testing show yield strength between 200 to 250 MPa, fracture strength between 450 to 750 MPa, and elongation around 35% to 45%. These and other properties are shown in Table 2. One can note that this is not a steel class with high mechanical strength values, but the high ductility and toughness makes them attractive for materials selection [6,7].

Table 2 - Austenitic AISI 304 stainless steel properties, annealed in sheet shape.

Properties		AISI 304
Density		8.0 g/cm^3
Hardness		max. 92 HRB
Tensile Strength		515 MPa
Young Modulus		193 GPa
Elongation		40 %
Thermal Conductivity	At 100ºC	16.2 W/m.K
	At 500ºC	21.5 W/m.K
Specific Heat		500 J/Kg.K
Electric Conductivity		720 nΩ.m
Magnetic Permeability		1.02
Melting Temperature		1400-1450ºC

Source: Adapted from Washko and Aggen (1990)[6].

The austenitic stainless steels show bigger ductility and a little higher tensile strength when compared to other ferritic stainless steels due to the higher work-hardening rates [10]. In comparison to ferritic and martensitic stainless steels, the austenitic stainless steels show higher corrosion resistance. The austenitic stainless

steels are widely used for high-temperature applications, such as high-temperature heat exchangers [6,10].

This class of stainless steel is also used in temperatures below zero because these steels contain enough quantities of nickel and manganese to reduce M_s, the temperature where the process to transform austenite into martensite starts, and do not show the ductile-brittle transition (DBT) [6,9]. In this class, tensile strength increases as the temperature reduces; this occurs due to the higher martensitic transformation in low temperatures [6].

Keeping the steel in high temperatures for a certain amount of time can cause the material to become brittle, reducing its capacity to resist to corrosion, due to precipitation of secondary phases, such as carbides, sigma (σ) phase, chi (χ) phase and Laves phase [6,7,9]. The σ phase nucleates in a form incoherent with the matrix in high energy regions (grain boundaries or twin boundaries). The χ and Laves phases, however, can be coherent with the matrix. The σ and χ only show undesirable effects in austenitic stainless steels, and the Laves phase can cause considerable precipitation hardening [7].

In austenitic alloys containing high chrome and molybdenum content, the embrittlement through sigma σ phase is a problem, due to the fact that there is a small quantity of δ ferrite present in these alloys, which can suffer transformation to σ phase in the same way that it occurs in ferritic stainless steels and duplex under annealing and slow cooling [10]. It is predisposed to have δ ferrite (in low quantities) in alloys that contain silicon, molybdenum, titanium or niobium because these are ferrite stabilisers[12].

The microstructure to the austenitic stainless steels, when ideally processed, is a single phase with all the alloying elements in solid solution, there are no carbides, ferrite or other phases. If the steel has really a single phase, the steel will present a better corrosion resistance. If there are precipitates in the grain boundaries, the steel will be susceptible to intergranular corrosion, which can lead to catastrophic failure[8,9,13]. The carbides identified as $M_{23}C_6$, being that the M denotes the metallic atom of the carbide, which can be chrome, iron and molybdenum. Aside from intergranular corrosion, if the carbide is formed by chrome, there is chrome depletion in the material, and if it is reduced below 12%, it will reduce the stainless property of the steel [10,13]. The metastable carbide $M_{23}C_6$ show favourable precipitation kinetic

and is virtually unavoidable if the steel is held in the precipitation range (450-850ºC). However, for long ageing times, if we have a chemical composition with niobium and/or titanium, it can dissolve giving place to MC carbides, which are more stable. Another type of carbide that can be found is the M_6C, but its occurrence is lower than the $M_{23}C_6$ or can even not be present in the austenitic stainless steel depending on its composition and/or thermal treatment [7].

For the purpose of removing carbides from the material it is possible to perform a solution treatment which will dissolve the carbides, and along with the treatment, rapid cooling is needed to avoid precipitation. To avoid that chrome carbides form, some elements are added such as titanium (AISI 321), niobium or tantalum (AISI 347), which are strong carbide forming elements [7-10].

During deformation of austenitic stainless steels, the mechanism of deformation through martensitic transformation can occur, where the microstructure leaves the austenitic state and transforms into martensite [4,14,15]. Two types of martensite can form in austenitic stainless steels, ε-martensite (hexagonal close-packed - HCP) and α'-martensite (body-centred cubic - BCC) [7,11,13].

3.1.1.1 *Martensitic transformation*

Martensitic transformation is a non-diffusional phase transformation, where there is no lattice distortion, being that the reduction in Gibbs's free energy is the driving force for the transformation [4,14,15]. The martensitic transformation occurs through coordinated movement of atoms, where the atoms involved move in distances smaller than the lattice parameter. The lattice of the FCC structure is intimately related to the BCC and body-centred tetragonal (BCT) structure, as seen in Figure 1 (a) [4,15,16].

As is observed in Figure 1, the BCT structure belongs to an FCC lattice, where the Bain's deformation can distort the lattice forming a BCC structure. This deformation occurs in homogeneous form, where the BCC structure can be generated from an FCC structure through compression around 17% in the direction of one of the axes of the austenite cube ([001], for example) and uniform simultaneous expansion at around 12% along the perpendicular axis ([010] and [100]) [4,13,15].

Figure 1 - Transformation of a FCC lattice into BCC. The BCT cell is indicated in the FCC structure in (a), alone in (b). The Bain deformation transforms (b) into (c).
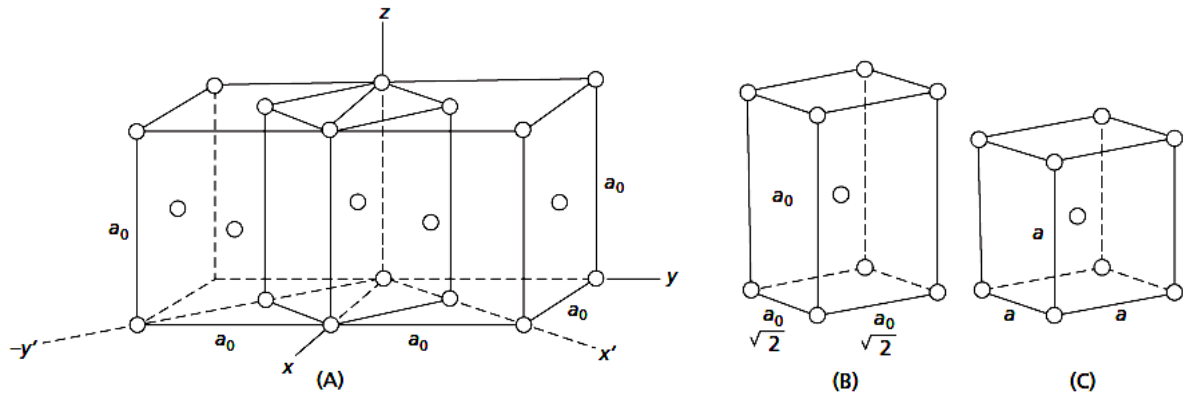
Source: Abbaschian, Abbaschian and Reed-Hill (2009)[16].

The Bain's deformation (B) show that the FCC to BCC transformation occurs with as little movement as possible; however, this distortion is not enough for the martensitic transformation to occur. Because, since there is no thermal activation, it must have interface continuity between the austenitic and martensitic phases so the dislocations can slide as the quantity of martensitic phase increases. The growth of the new phase happens through the movement of the interface between phases[4,15,16].

Figure 2 - Phenomenological theory of the martensite crystallography.
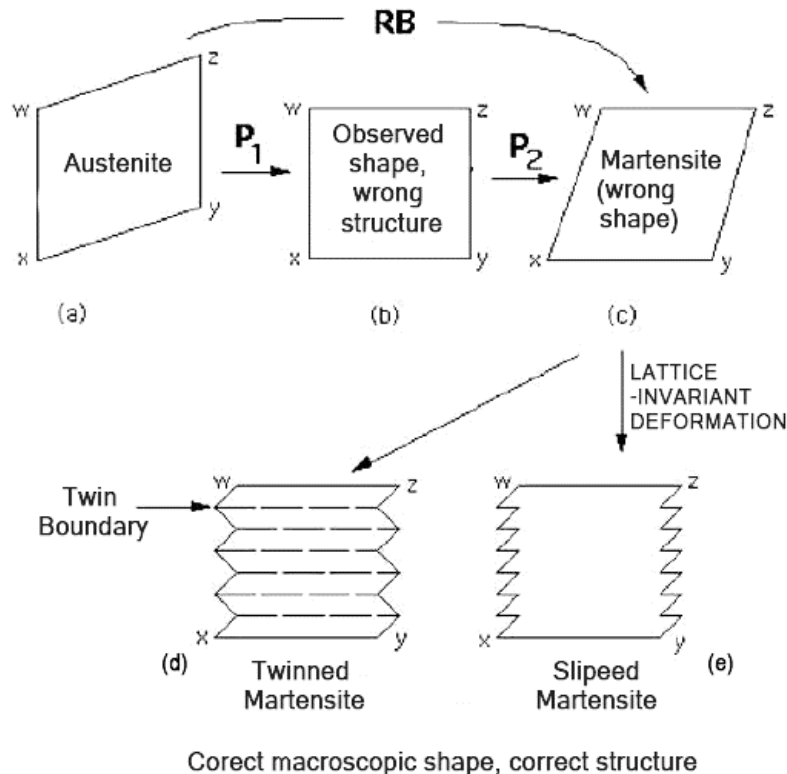
Source: Bhadeshia and Honeycombe (2006)[4].

However, in ferrous alloys, a coherent interface is not possible. In the best case, what can happen is for a semi-coherence to form between them with a totally coherent direction in the interface, called invariant line. For this line to have coherence, it is necessary to occur a rotation of the rigid body (R). In this way, a combination of B and R is needed, so the transformation of austenite into martensite can happen, as seen in Figure 2 (a) and (c). When the (P1) forms and the (P2) structure are correct, the invariant line can be seen microscopically in two forms, depending on which mechanism formed it, through twinning or dislocation motion, as seen in Figure 2 (d) and (e), respectively [4,15,16].

As the tension is applied, the martensite volume fraction increases. Being that as the deformation degree increases, the temperature decreases and/or the strain rate increases, the martensite volume fraction increases. The martensite formed commonly named stress-induced martensite in order to differentiate it from the one formed through fast cooling in medium and high carbon steels, also called athermic martensite [7,14]. High strain rates can suppress the martensite formation because of the adiabatic heating during the deformation [17,18]. Two types of martensite can form from austenitic stainless steel, ε-martensite (HCP) and α' (BCC), being that, according to Padilha (2004), the first one generates a volumetric contraction of 1.12% and the second one, volumetric expansion of 2.57% [7]. The occurrence of these phases varies according to the chemical composition, SFE, temperature, deformation mode and strain rate [7,11,13].

According to Mangonon and Thomas (1970) – study in AISI 304 stainless steel – the ε phase can form in low temperatures with or without deformation, on the other hand, α' phase needs strain for its formation, preferably, in the intersections with the ε phase with grain boundaries and twins. They also show evidence that ε-martensite can be an intermediary phase for α'-martensite formation [19,20]. The presence of α'-martensite causes an increase in mechanical strength, generating a higher yield strength, higher work hardening rate and higher hardness. However, ε-martensite does not show these mechanical property changes and, thus, its effect is not considered [7].

The transformation induced plasticity (TRIP) is an effect in austenitic stainless steels that comes from the martensitic transformation where high strength and toughness steels can be obtained [4,14,21-23]. The stacking fault energy (SFE) has

influence on the martensitic transformation, which will be favoured in case of the SFE is low, favouring the TRIP [24]. The martensitic transformation has the effect of increasing the work hardening rate and generating homogeneous deformation [4,14, 21-23].

It is convenient to show at this point the steels which we have twinning induced plasticity (TWIP). The mechanical twinning is a mechanism of plastic deformation that occurs due to shearing tensions, where the crystalline structure is preserved, but in the twin region, there is structure reorientation. This deformation mechanism will be approached in depth in item 3.2. The alloys are austenitic, and during mechanical deformation, they stay that way, the material accommodates the strain both through dislocation motion as well as through mechanical twinning in the $\{1\ 1\ 1\}\gamma\ <1\ 1\ 2>\gamma$ systems. The twins also contribute to the work hardening rate increase, due to the non-twinned austenite subdivision in fine regions. The TWIP steels show very low yield strength; however, the ultimate tensile strength is high. This occurs due to the significant work hardening coefficient, which results in a large quantity of uniform elongation [4]. With a medium SFE, the twinning induced plasticity mechanism will be favoured [24].

3.1.2 Ferritic Stainless Steels

In comparison to the austenitic class, the ferritic stainless steels show lower corrosion resistance, lower work hardening rate, however, shows better machinability and lower cost. The percentage in nickel is lower in ferritic stainless steels when compared to the austenitic ones, mainly because nickel is expensive, the ferritic show lower price. The ferritic class is composed by alloys that contain 10.5% to 30% chrome and can contain other elements, such as aluminium, titanium, niobium, molybdenum and silicon, which add particular characteristics to the alloy. In Table 3 are presented compositions of some standard ferritic stainless steels [6,10].

The ferritic stainless steels have a BCC structure and present magnetic behaviour [3,6]. Ferrite plus carbides compose its microstructure, and the ferrite phase stabilisation is reached due to the presence of chrome and other alloying elements, like titanium, niobium or zirconium [6,25]. These stabilising elements react with carbon and nitrogen to form carbides and nitrides, removing the interstitial atoms from a solid solution [25].

This class of stainless steel present high ductility and plasticity, yet, in high temperatures the steels lose resistance, and in low temperatures, there is ductility reduction [6,10]. This happens because with the decrease in temperature it is possible to observe the ductile-brittle transition in the fracture behaviour; this subject will be approached in item 3.4.3.

Table 3 - Composition (% in weight) of some standard ferritic stainless-steels.

	C	Mn	Si	Cr	Ni	P	S	Others
405	0.08	1.00	1.00	11.5-14.5	...	0.04	0.03	0.10-0.30 Al
409	0.08	1.00	1.00	10.5-11.75	0.50	0.045	0.045	6x %C min – 0.75 max Ti
430	0.12	1.00	1.00	16.0-18.0	0.75	0.04	0.03	...
430F	0.12	1.25	1.00	16.0-18.0	...	0.06	0.15 min	0.6 Mo
430FSe	0.12	1.25	1.00	16.0-18.0	...	0.06	0.06	0.15 min Se
434	0.12	1.00	1.00	16.0-18.0	...	0.04	0.03	0.75-1.25 Mo
436	0.12	1.00	1.00	16.0-18.0	...	0.04	0.03	0.75-1.25 Mo; 5 x %C min – 0.70 max Nb
439	0.07	1.00	1.00	17.0-19.0	0.50	0.04	0.03	0.15 Al; 12x %C min – 1.10 Ti
442	0.20	1.00	1.00	18.0-23.0	...	0.04	0.03	...
446	0.20	1.50	1.00	23.0-27.0	...	0.04	0.03	0.25 N

Source: Adapted from Washco and Aggen (1990)[6].

For the AISI 430 stainless steel, when annealed, it is expected a tensile strength of around 450 MPa, a minimum strain of 22% and hardness of a maximum of 88 HRB. These and other properties of the AISI 430 are presented in Table 4 [6].

The ferritic stainless steels, in comparison with the austenitic class, present a thermal expansion coefficient relatively smaller and higher thermal conductivity, these characteristics make the ferritic ones more resistant to thermal fatigue [10].

Table 4 - Properties of the AISI 430 ferritic stainless-steel, annealed in sheet shape.

Properties		AISI 430
Density		7.8 g/cm^3
Hardness		max. 88 HRB
Tensile Strength		450 MPa
Young Modulus		200 GPa
Elongation		22%
Thermal Conductivity	At 100ºC	26.1 W/m.K
	At 500 ºC	26.3 W/m.K
Specific Heat		460 J/Kg.K
Electric Conductivity		600 nΩ.m
Magnetic Permeability		600-1100
Melting Temperature		1425-1510 ºC

Source: Adapted from Washko and Aggen (1990) [6].

The sigma σ, chi χ and Laves phases mentioned in item 3.1.1 also occur in ferritic stainless steels. The nickel quantity in the ferritic class makes the formation of secondary austenite adjacent to the σ phase; this happens because the presence of nickel around σ phase, allied with the reduction of chrome and molybdenum, reduces the ferrite phase stability [13].

The precipitation of a chrome-rich phase, named α', leaves regions around it poor in chrome, which besides being harmful to corrosion resistance reduces the material's toughness. This is a phenomenon known as "475°C embrittlement". The α' phase can occur due to prolonged heating in temperatures close to 450°C in steels containing until 17% in weight of chrome. For steels with compositions higher the precipitation can occur through spinodal decomposition. This phase can be eliminated through heating at around 600°C, followed by rapid cooling [26,27].

Special care must be taken when rolling the AISI 430 steel, because it has a tendency to form roughness on the sheet surface, not allowing satisfactory finishing. This happens due to the crystallographic texture developed during the

thermomechanical processing, that is, during deformation there is a preference in aligning in specific directions, like {111} <110>, {001} <110> and {112} <110>. Lots of researches try to relate the appearance of roughness on the deformed sheet with the presence of texture, grain size and area reduction [28-36].

3.2 PLASTIC DEFORMATION MECHANISMS

Permanent plastic deformation can occur in different ways, through dislocation motion, mechanical twinning, phase transformation, diffusion and grain boundary sliding [37]. Usually, there will be two or more deformation mechanisms that are acting, only in certain cases, there will be only one of them occurring in bigger intensity. In normal conditions, plastic deformation occurs mainly through dislocation movement along well-defined crystallographic plans, called slip plans [14,38-40].

When dislocations interact directly among themselves and with other imperfections, or with internal tension fields, there is a reduction in dislocation's medium mobility. That said, it is necessary bigger tension to move the dislocations; this phenomenon is called work hardening. When the applied tension is enough to overcome those barriers, the plastic deformation will occur [14,38-40].

The internal energy of the material changes due to plastic deformation, part of the energy involved is dissipated in the form of heat, and a smaller part of it is stored within the material. This energy is associated with the crystalline defect generation during deformation, such as dislocations, vacancies, stacking faults, twins and interstitial defects, characterised by atoms imprisoned in interstices of the lattice during deformation [41].

The disposition and density of dislocations in materials are highly varied and depend on various parameters, such as deformation mode, strain rate, temperature, crystalline structure, stacking fault energy, grain size, and others [14,38,42-45].

The stacking faults can be generated by dissociation of unitary dislocations into partial dislocations, as shown schematically in Figure 3 [14]. The crystalline defect between two partials can be described as a stacking fault in crystals with FCC, HCP and diamond cubic structures. For a BCC structure, it cannot be treated in the same way; this is because a dislocation dissociates generating three or more partials, and thus, one cannot describe the region in between them as a stacking fault [46].

Figure 3 - Decomposition of a dislocation b_1 into two partials b_2 and b_3, separated by a d_0 distance.
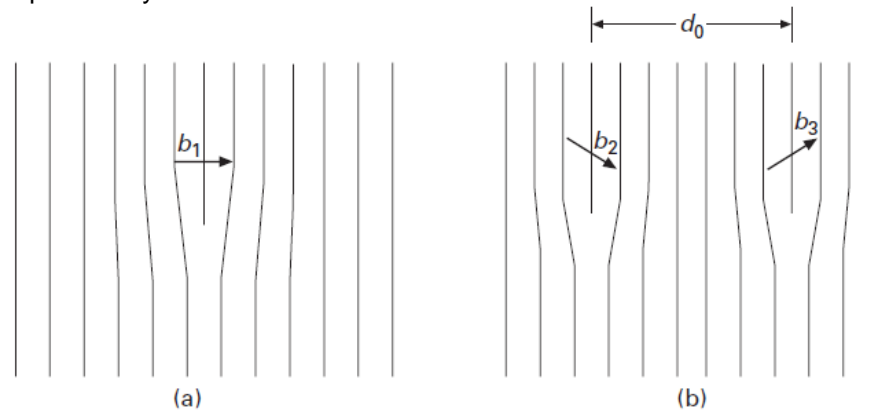
Source: Meyers and Chawla (2009)[14].

The SFE has a significant influence on dislocation distribution in a metal or alloy when work hardened. When the metal shows low SFE, the mobility of its dislocation pairs is low due to the fact that the partials are too far apart from one to another. With this, there is a difficulty to occur cross-slip and climb. The low mobility leaves an homogeneous distribution of dislocations in the structure, as seen in Figure 4 (a) [37,46].

Figure 4 - Schematic drawing of the plane arrangement of dislocations (a) homogeneously distributed in a cold worked grain, (b) cellular schematic arrangement.
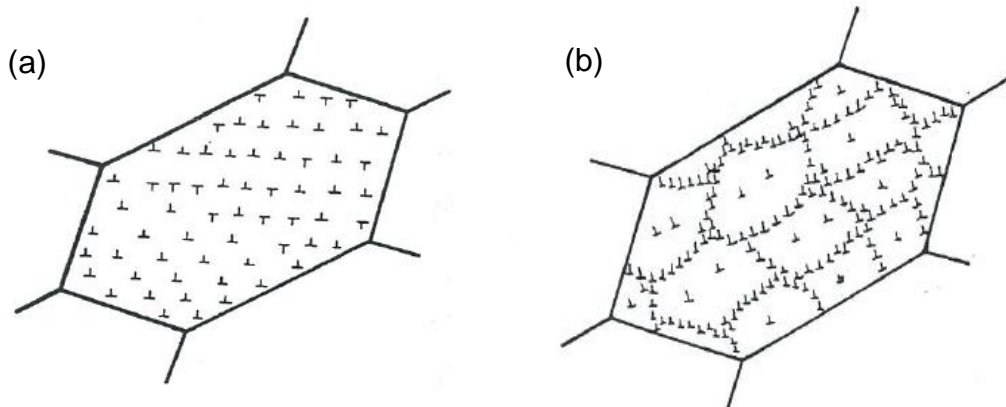
Source: Padilha and Siciliano Jr (2005) [37].

The partial dislocations are close to each other in metals with high SFE, making cross-slip and climb easier. In this way, there are dislocations with high mobility that tend to annihilate and rearrange themselves with neighbouring dislocations with different signals. Then, materials with high SFE tend to have a heterogeneous dislocation distribution, as shown in Figure 4 (b) [37,46]. The heterogeneous distribution of dislocations forms what is named as dislocation cells.

A metal with low SFE will show more significant dislocation density than metal with high SFE for a certain degree of deformation [37].

The FCC and low SFE metals, for example, the austenitic phase, tend to show a more homogeneous distribution of dislocations, as shown in Figure 4 (a). However, high SFE metals, above 60 mJ/m^2, like the ferritic BCC phase, have a heterogeneous dislocation distribution, as shown in Figure 4 (b) [37].

In situations where the motion of planes is difficult, the mechanical twinning acts as an alternative way of plastic deformation. This occurs in materials that show little slip systems, or during plastic deformation in low temperatures or high strain rates [37]. As dislocation motion and mechanical twinning are plastic deformation mechanisms that compete with each other, then, the one that presents the lower tension will occur at the start of the plastic deformation [43,47].

Metals, especially the ones with HCP structure, show twinning as the main mechanism for plastic deformation, this occurs due to the little slip systems in the structure. Eventually, twinning occurs in metals with BCC crystalline structure and with lower frequency in FCC metals with high purity because these crystalline structures show bigger quantity of slip systems, considering that the slip systems of the FCC structure are more effective than the ones in the BCC structure. For mechanical twinning to happen in FCC metals, it is necessary a combination of factors to occur, such as high strain rate, low temperature and unfavourable crystallographic orientation for dislocation motion [43,47].

A twin generates the relative shearing between two portions of the crystal, in other words, it is the movement of a part of the crystal relative to the other one, where the crystalline structure, lattice parameter and crystalline continuity is maintained, the only change is the difference in orientation. It occurs through shearing of the crystalline lattice, creating a mirrored region, in a defined crystallographic plane, as seen in Figure 5 [14,43].

The boundary between the twinned region and the rest of the grain is called twin boundary. Usually, the contribution of the twinning in relation to the volume of the deformed material is small in relation to dislocation movement. But its significant contribution is in the resulting crystallographic reorientation, being able to put twinned regions in crystallographic orientations favourable to dislocation motion [14].

Figure 5 - Schematic example of a twin in a FCC metal.
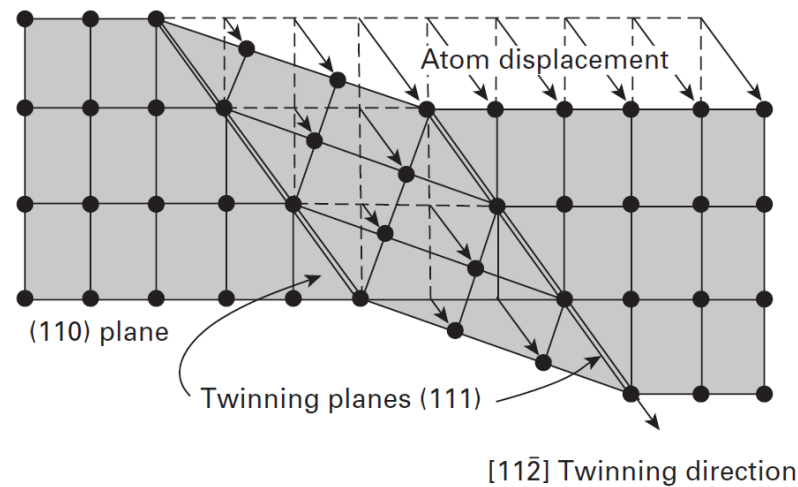
Source: Meyers and Chawla (2009) [14].

As seen earlier, the SFE influences dislocations mobility directly, so, it also has influence in mechanical twinning. Twinning is favoured when the metal presents low SFE, because then, there is lower dislocations mobility, disfavouring the deformation through dislocation motion. The energy of the twin boundary is also reduced with lower SFEs, that provokes smaller energetic cost for twin formation and, consequently, bigger ease for the deformation to occur through twinning [14,37,47].

The competition between plastic deformation mechanisms, through dislocations motion and mechanical twinning, show that, with an increase in strain rate or temperature reduction, the dislocations motion is greatly hindered, because the mobility is reduced due to SFE reduction [14]. High strain rates reduce the time for the dislocations to move; they then, may not have enough time to move, favouring mechanical twinning.

Diffusion is another plastic deformation mechanism. The diffusivity depends on various factors, such as the size of the atoms involved, crystalline structure, temperature and crystallographic orientation. In pure metals, above 0 K, the atoms vibrate around its equilibrium positions in the lattice and change position between themselves frequently, a mechanism that is called self-diffusion. There are lots of self-diffusion mechanisms: the ones that need a coordinated movement of atoms, like changing places with a neighbouring atom and the ring mechanism; a kind of interstitial diffusion, that is very improbable to happen; and the most common, which is the change of place between an atom and a vacancy [14,48].

In the case of solid solutions, either interstitial or substitutional, diffusion is also present. For the substitutional solid solution, the most common diffusion mechanism is the change of places with vacancies, just like in self-diffusion. In interstitial solid solution, it is more probable that the interstitial atoms diffuse through lattice interstices. It is also possible for diffusion to occur along crystalline defects, such as grain boundaries, linear defects and the external surface of the material [48].

Another mechanism for plastic deformation is the martensitic transformation, where the material's strain occurs due to the non-diffusional phase transformation. This mechanism was detailed in item 3.1.1.1. For austenitic stainless steels, the transformation happens from the austenitic phase (FCC) to the martensitic phase (BCC), in this transformation, there is an expansion of the unitary cell, which generates the deformation of the material [4, 7, 13-16].

The SFE of pure metal can be altered with the addition of solute atoms and with the initial grain size, which will impact the dislocation distribution. The solute atoms interact with the dislocations, reducing their mobility, which makes it difficult to annihilate dislocations through cross-slip and climb. The density of dislocations is bigger for samples with smaller grain size, for higher degrees of deformation ($\varepsilon > 1.4$) the density differences of dislocations are small when compared to samples with a low degree of strain ($\varepsilon < 0.7$) [37].

The deformation through grain boundary sliding is commonly found in creep mechanisms. During plastic deformation there is shearing of those grain boundaries and, in order to keep the cohesion of the grains, a cooperative movement between grain boundaries is necessary [43].

The temperature in which the material is deformed will impact the density and dislocation distribution, as well as in the stored energy. Being that the mobility of the dislocations decreases as the temperature reduces, the SFE also decrease. The effect of increasing the strain rate is equivalent to a reduction in deformation temperature, but the temperature, usually, is more impacting in the material's response than the strain rate [37].

The Zener-Hollomon (Z) parameter can be calculated and used to comprehend the conjunct influence of the temperature and strain rate, being that bigger Z values tend to mechanical twinning, increase in resistance, reduction in grain size and decrease in spaces between deformation twins. The increase in the Z

parameter can be caused by the rise in the strain rate and temperature reduction, as can be observed by the Zener-Hollomon equation:

$$Z = \dot{\varepsilon} \, \exp \frac{Q}{RT} \tag{1}$$

where:

Z: Zener-Hollomon parameter;

$\dot{\varepsilon}$: Strain rate;

Q: Activation energy;

R: Gases constant;

T: Temperature [49,50,51].

In the course of the material's deformation, when there is a rotation of the grain in the deformation mechanism, the crystalline lattice may rotate to a preferential orientation, called deformation texture. The deformation textures caused by uniaxial traction commonly found for FCC metals are <111> + <100> and for BCC <110> [52,53].

3.2.1 Dynamic Recovery x Dynamic Recrystallization

During material's deformation, it is possible that a recrystallization or recovery process happens; they are called dynamic recovery and dynamic recrystallization [37]. These phenomena happen simultaneously with strain and, usually, in high temperatures. Being that the temperature for these phenomena to happen depends on the material, and in many cases occur at room temperature [37,41].

The occurrence of dynamic recovery is related to the SFE of the material. Where the recovery kinetics in metals with high SFE is fast, reducing the number of defects present in the material. Alloys with low SFE show slow recovery kinetics, in this way the quantity of defects stays high during deformation [37].

When the material is deformed at high temperatures, due to thermal activation, there is a rearrangement of the dislocations formed during deformation for a subgrain structure, as seen in Figure 6 [37].

Figure 6 - Phases of plastically deformed metal recovery; (a) dislocations tangles; (b) formation of cells; (c) annihilation of dislocations in the walls of cells and (d) formation of subgrains.

(A)   (B)   (C)   (D)
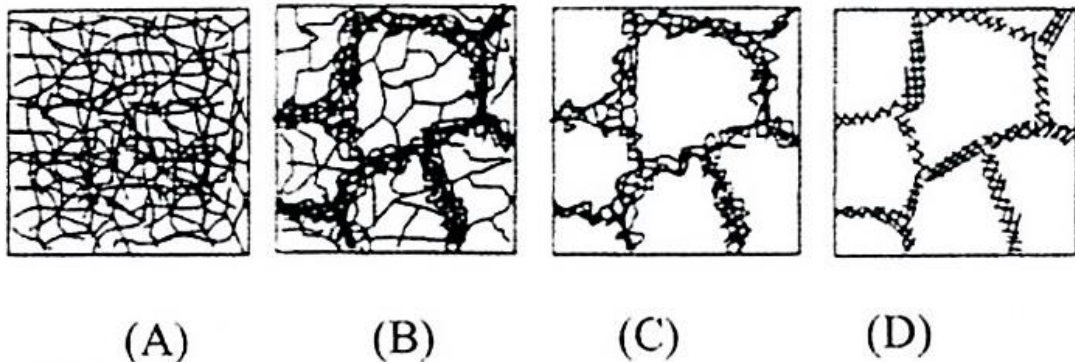
Source: Padilha and Siciliano Júnior (2005) [37].

These subgrains are formed by dislocation walls, called dislocation cells, where, for its formation, the annihilation of vacancies, interstitials and opposite signal dislocations is observed, as well as the rearrangement of them in the boundaries and the occurrence of cross-slip and climb [37].

During dynamic recovery, the grains stretch themselves in the function of deformation, and the subgrains keep their equiaxial structure, as seen in Figure 7.

Figure 7 - Microstructural changes during dynamic recovery. (a) Initial microstructure; (b) Microstructure after deformation ε_1; (c) microstructure after deformation ε_2, being $\varepsilon_2 > \varepsilon_1$
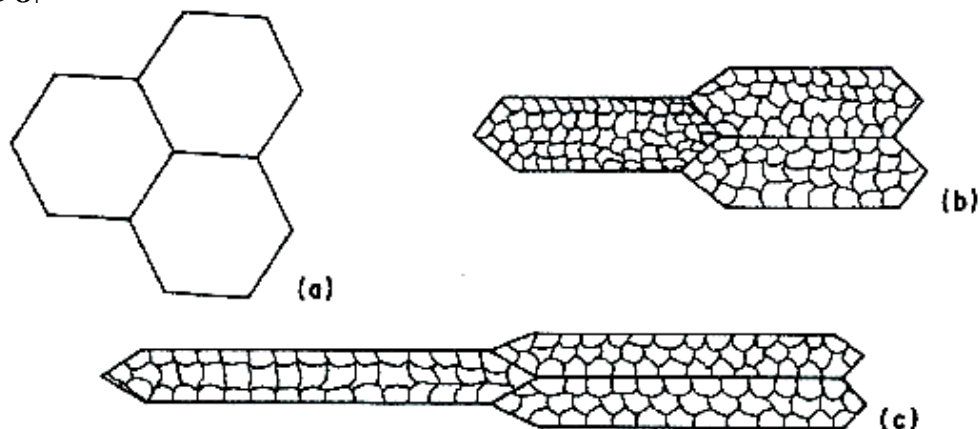
Source: Padilha and Siciliano Júnior (2005) [37].

The material's nature, the temperature and the strain rate will impact on the perfection of the sub-boundaries, on the crystallite dimensions and the differences in orientation [37]. The reduction in deformation temperature can reduce the occurrence of thermally activated phenomena, making that the rearrangement and annihilation

of dislocations more difficult, when this happens, it is said that there was partial suppression of the dynamic recovery [16].

The form of the stress x strain curve is affected by the effect of dynamic recovery, that is because it reduces the needed energy to move the dislocations through the slip planes to form the lower energy dislocation structures, called LEDS structure (Low Energy Dislocation Structure). Thus, the dynamic recovery makes the formation of additional dislocations easier, allowing for a bigger material deformation[16].

In Abbaschian (2009) it is cited that the fundamental difference between static and dynamic recovery is that in the first the movement of dislocations to form the subgrains happens due to an interaction between dislocations themselves, and in dynamic recovery, the applied tension is summed up to this interaction between dislocations [16]. In this book, Abbaschian describes that the correspondence between a metal showing dynamic recovery and its SFE suggests that the primary mechanism involved in dynamic recovery is the cross-slip thermally activated [16].

As mentioned before, during deformation a preferred alignment of specific orientations can occur, that is, texture. During the recrystallization, new grains grow at the cost of deformed grains, and the deformation texture can be replaced by recrystallization texture, which can be totally different from the texture presented previously. The presence or absence of these preferred orientations depends on various factors of the material and processing, such as chemical composition, starting grain size, second phase's precipitation and deformation temperature [53]. Typically during recrystallization, for FCC metals, there is a rotation of 30 to 40° around the preferential directions <111>, and for BCC metals the rotation occurs around 25 to 30° around the preferential directions <110> [54].

3.3 STUDY AT LOW TEMPERATURES

Temperature affects more the properties of the material than other process variables like pressure, magnetic field and electric field [48,55]. Some properties that can be altered with temperature are resistance, Young modulus, ductility and fracture toughness [56]. In this way, the effect of temperature is an area of interest to many researchers, and the results obtained are contributing to significant technological advances. However, the phenomena in high temperatures were more studied than

in low temperatures due to the difficulty to get low temperatures, yet in the last 50 years, the studies done in low temperatures have grown considerably due to the viability in using low temperatures [55,57].

The term "low temperature" is defined in terms of where the metallurgic processes change, in which, usually, are $T < 0.5\ T_m$ (melt temperature), although for structural materials that show little slip systems that are considered as $T < 0.3\ T_m$. For many applications, low temperature is associated with cryogenic temperatures, being the term "cryogenic" referred to temperatures below -150°C. Today there is a fair quantity of substances that can be used for experiments in low temperatures; some of them are shown in Table 5 [56].

Table 5 - Substances utilised for low-temperature testing.

Substance	Temperature °C
Ice	0
Isobutane	-10
Carbon tetrachloride	-23
Propane	-42
Trichlorethylene	-73
Carbon Dioxide	-78
Methanol	-98
n-Pentane	-142
Iso-pentane	-160
Methane	-161
Oxygen	-182.9
Nitrogen	-195.7
Neon	-245.8
Hydrogen	-252.6
Helium (He_4)	268.8
Helium (He_3)	269.8

Source: Adapted from Walsh (2004) [56].

Between these substances, some are easier to use than other ones, being hydrogen and oxygen two of them that, if possible, must be avoided (risk of explosion). The substance to be used needs to be chosen according to the test's

necessity, and it is possible to mix some of them to obtain intermediary temperatures[56].

3.3.1 Cryogenic Deformation

The cryogenic deformation can cause changes in material's properties, one of the reasons is the change in the most active deformation mechanism, such as the change in the dislocation motion mechanism for mechanical twinning, and/or occur some phase transformations not detected in higher temperatures. Also, one can observe an increase in mechanical resistance and ductility, simultaneous or not, when the metal is tested at low temperatures [58,59].

In a deformed metal at room temperature, the increase in the number of dislocations difficult their movement, increasing the material's resistance, that is because the dislocations lock themselves to each other or, when in solid solution, move close to the solute making the deformation more difficult [14,60]. The dislocations motion is impacted by the temperature effect, being that the bigger the temperature, bigger will be the ease to move the dislocations and, consequently, thermally activated phenomena, such as climb, are favoured. That way, temperature reduction requires more significant tension to move the dislocations, making secondary deformation mechanisms start to operate, such as mechanical twinning and stress-induced martensitic transformation [14,47,60].

Studies with cryogenic deformation encompass lamination processes, uniaxial traction, milling, compression, severe plastic deformation (SPD), stretching, among others; in metals such as copper, aluminium, silver, titanium, vanadium and stainless steels [17,56-59, 61-75]. Authors found, in general, an increase in mechanical resistance simultaneously with the increase in ductility after cryogenic deformation. Either BCC, FCC and HCP structures found a rise in the cited properties, of course, that one more effective than another one.

The SFE will also influence cryogenic deformation due to dynamic recovery phenomenon, as mentioned in item 3.2.1. In metals with high SFE, due to the way that the dislocations are distributed inside the grain, there is bigger ease for the recovery to occur [37].

Low SFEs result in the formation of twins and stacking faults during plastic deformation, leading to an increase in defect density and microstructural refining. The

phenomenon occurs because reducing the temperature will increase the volume fraction of twins and, with that, the distance between twins is lower, generating more significant grain refinement. Besides SFE, the starting grain size will also influence in the answer of the material to deformation, being that bigger grain sizes tend to generate twins in metals and alloys with low SFE [64].

In the deformation of a polycrystalline material, the grains that are favourably oriented to the deformation's orientation will deform initially. With a set strain rate, the grains that are randomly oriented in the metal will rotate, with the movement restrained by the neighbouring grains and align with the deformation direction. Thus, there will be strong grain orientation, called texture [14]. The presence of texture in the deformed material can be indicative that the main deformation mechanism is dislocation motion because mechanical twinning does not need grains to be rotated; they are done through lattice shearing [59,63].

In cryogenic deformation microstructural refinement can be intense, due to the partial suppression of dynamic recovery, mechanical twinning and fragmentation of grains by shearing bands generated in strain, reducing the crystallite size [59,63].

For austenitic stainless steels, the alloys show a considerable percentage of austenite -> martensite phase transformation after cold work at room temperature. Carbon and nitrogen tend to stabilise the austenite phase; in this way, a much more significant variation is found in 304 and 304L stainless steel that show little concentration of those elements [60,55]. The phase transformation has a strong influence of temperature, where an earlier phase transformation occurs as the temperature is reduced [17,19].

It can be concluded that crystalline structure, SFE, grain size, strain rate and temperature will influence the studied material's mechanical behaviour [58].

3.4 FRACTURE MECHANICS – MICROSTRUCTURAL CONSIDERATIONS

3.4.1 Ductile Fracture

The fracture modes of metallic materials can be divided into two big classes, ductile and brittle. However, as metals show high dislocation mobility, usually, the fracture is ductile. The subclasses for ductile fracture are presented in Figure 8. The ductile mode can happen through nucleation, growth or coalescence of microvoids

(through grains or grain boundaries), through reduction of the transversal section or shearing [14].

Figure 8 - Schematic classification of the ductile fracture mechanics for metallic materials.
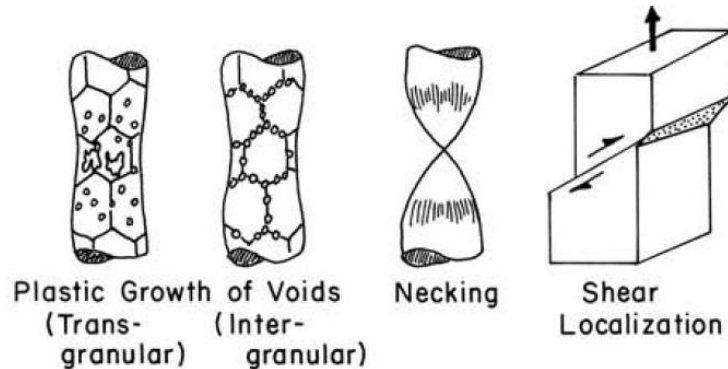
In a pure monocrystalline material, dislocations move without the presence of barriers, such as grain boundaries and precipitates. Due to this, there are no regions with tension accumulation, so there is no formation of cracks and the crystal will deform plastically in a homogeneous form until the start of the necking, place with high plastic instability. After the neck is formed, the deformation will be localised in this area and will deform until fracture, which can be a line or a point [14].

There will be stress concentrators in case there are barriers for the dislocations motion, auspicious places for microvoid nucleation, shown in Figure 8. However, these microvoids will not have cracks propagating between them; in these regions, there will be plastic instability, which can lead to fracture as the answer to the applied tension [14].

Microcracks can be nucleated in grain boundaries that show dislocation stacking and do not show tension relief through dislocation motion in the neighbouring grain, these are called Zener-Stroh cracks and are presented in Figure 9 (a). Another form of crack nucleation is through combining of lattice deformation with plane folding and twinning, as seen in Figure 9 (b) and (c) respectively.

The grain boundaries sliding, plastic deformation mechanism, generates tension concentration in triple points of grain boundaries, where microcracks can appear and are called type "w" cracks, as seen in Figure 9 (d). In high-temperature low tension conditions, the formation of microcavities around grain boundaries that

are approximately 90° from the tension axis can happen, seen in Figure 50 (e). These microcavities are called type "r" [14].

Figure 9 - Generation of microcracks and microcavities in the material. (a) From dislocation piled up at a barrier (Zener-Stroh); (b) and (c) through lattice rotation due to bend planes and deformation twins; (d) through grain-boundary triple point, type "w" and (e) in elevated temperatures and low tension are formed type "r" cavities in the grain boundaries.
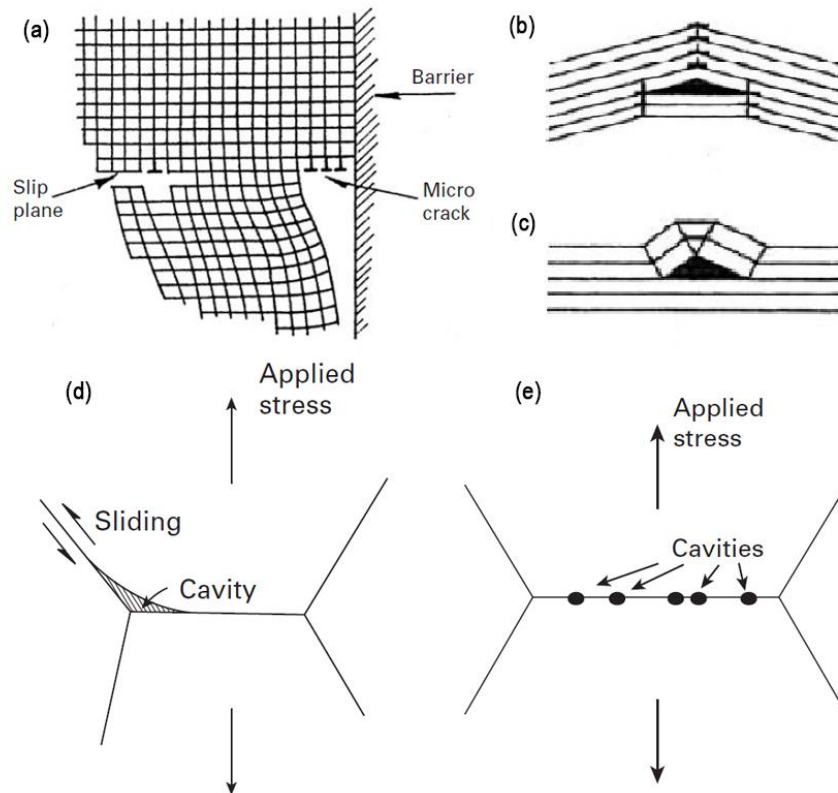
Source: Adapted from Meyers e Chawla (2009) [14].

In metals that show precipitates, microcavities will form around them [14,76]. Usually, the precipitate is more fragile and the matrix more ductile, so the precipitates cannot accommodate the matrix's deformation, in this way they may break or spread through the matrix. In both cases, there will be the formation of microcavities, and these, through the application of tension, can grow and coalesce leading the material do rupture. The microcavities and microcracks that emerge from the points described above are formed to accommodate the difference in the material's deformation [14].

At cryogenic temperatures, there are a more significant number of dimples in the fracture surface and with smaller size. It occurs due to the bigger potential to dimples nucleation, resulting in a lower available free path for expansion of the generated microcavities. It indicates that the material stored higher amounts of energy in internal defects during deformation [74,77].

It is common in ductile samples of cylindrical form to observe the cone-cup fracture, where it is possible to see microcavities (dimples) in the fracture region. The cone-cup form happens due to the shearing deformation, where the material deforms through dislocations motion, that the critical resolved shear tension reaches critical tension (at 45° in relation to the tensile load application). During ductile material's deformation, the dimples are formed, grow and agglutinate. And, according to growth, the dimples coalesce, but not all the microcavities contribute to the formation of the material's rupture. As tension is applied there is an increase in the tension concentration, making the microcavities expand to adjacent areas. With this mechanism, the sample's centre separates, and the failure propagates outwards, concluding the rupture of the material [14,78].

Dimples can also collaborate with another failure mechanism, where there is the main crack. Ahead of the crack, there will be a high-tension region, propitious to the formation of dimples. As tension is applied dimples grow and can unite themselves to the crack, increasing its size, and again, ahead of the main crack there will be a high-tension region and the mechanism will happen successively until the fracture of the material [14].

In FCC metals, where the slip systems are more effective, the application at cryogenic temperatures has shown a simultaneous increase of resistance and ductility. Some materials can show ductility increase at -150°C and have a loss of ductility in lower temperatures (-196°C), other ones can have discontinuous yield (serrated flow), as shown by Kula and De Sisto (1966) [58].

It is more probable that with the reduction of processing temperature or with an increase of the strain rate, metals with BCC or HCP crystalline structure show brittle fracture due to the rise in resistance to yield. This occurs due to the little and/or inefficient slip systems of these structures [58].

3.4.2 Brittle Fracture

In Figure 10 are presented, schematically, the forms of brittle fracture of metallic materials, which do not involve, or involve little, plastic deformation. Cleavage is the most common type of brittle fracture; in it, there is only one direct separation through atomic bond rupture inside the grains. The cleavage occurs in

specific directions and planes, so in crystalline materials, when the fracture finds a grain boundary, its direction changes preferentially to that grain [14,78,79].

Figure 10 - Schematic classification of the fragile fracture mechanics for metallic materials.

Cleavage   Inter-
            granular
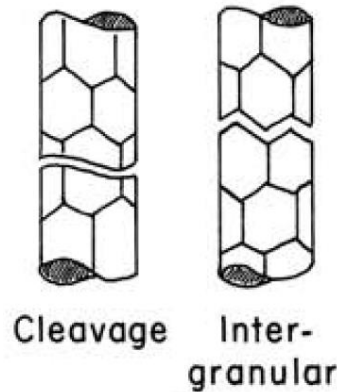
Source: Adapted from Meyers and Chawla (2009) [14].

Fracture surface shows straight facets with shinny appearance, and in some cases, one can note the presence of river marks. The river marks occur due to the presence of cracks in two parallel crystallographic planes (Figure 11 (a)), which can unite through secondary cleavage or shearing, forming steps, as seen in Figure 11 (c)[14,16].

Figure 11 - Stages of cleavage formation. (a) Parallel cracks (A, A) join through cleavage in B or shearing in C; (b) start of cleavage stage by passage through helix dislocation; (c) river mark formation.
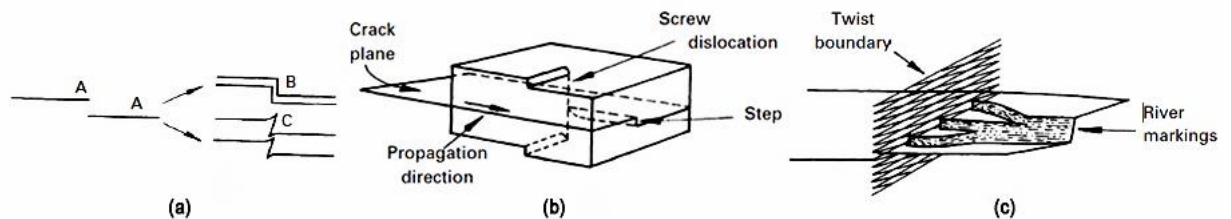
Source: Meyers and Chawla (2009) [14].

The start of cleavage happens when the crack passes through a screw dislocation, as seen in Figure 11 (b). Usually, the minimum energy to form a step is when cleavage occurs perpendicular to the crack's plane and parallel to the direction of propagation. For FCC metals, usually, cleavage does not happen in normal conditions, due to the significant amount of available slip systems that will act before the necessary tension for cleavage is reached. Although, for BCC and HCP structure metals cleavage is very common, due to the little and/or inefficient slip systems [14,16].

Besides crystalline structure, temperature, strain rate and applied load influence the fracture mode, being that increasing the load and strain rate and reducing temperature will favour the brittle fracture mode [16].

Intergranular brittle fracture is low energy fracture mode, where the cavities are nucleate and grow between grain boundaries, as seen in Figure 10. This crack path makes the fracture surface present a mat appearance macroscopically. Microscopically it is possible to see little cavities around grains [14,16,78].

The brittle fracture mechanism through cleavage will happen when the crystalline region is more fragile than grain boundaries. The sensitisation of grain boundaries occurs through inclusion or segregation of a second phase in the grain boundaries, turning them into more fragile regions than the crystalline lattice, and the brittle intergranular fracture will occur [14,16,78].

3.4.3 Ductile-Brittle Transition

The reduction in deformation temperature or an increase in strain rate can alter the mechanical properties of the material and, consequently, change the fracture mechanism of the material. So that metal with a ductile fracture at room temperature does not exhibit the same behaviour at low temperature or high strain rates. This behaviour changes from ductile to brittle fracture occurs in a determined temperature, which is called ductile-brittle transition temperature [4,13,14,77].

Ferritic stainless steels show the ductile-brittle transition (DBT) in answer to plastic deformation, where temperature reduction will implicate in an increase in mechanical resistance and loss of ductility. This occurs due to the loss of capacity of screw dislocations perform cross-slip in the BCC structure with temperature reduction. On this, cleavage fracture can be started through intergranular cracks or by second-phase particles induced deformation cracks [13,79]. Other aspects influence the ductile-brittle transition temperature, such as small grain size, low interstitial carbon and nitrogen quantity and absence of second phases, which can reduce the transition temperature [4,13].

The austenitic stainless steels do not show a ductile-brittle transition. However, the curve shape can be changed to sigmoidal due to martensitic transformation occurs more intense at low temperatures. The α'-martensite formed shows higher resistance and less ductility than the austenite initial, resulting in a

material more fragile than at room temperature. Therefore, fracture characteristics still ductile [11,13,17].

3.5 X-RAY DIFRACTION

In the materials area, there are plenty of X-ray usage characterisation techniques. In special, the X-ray diffraction is, increasingly, being utilised, because it is a non-destructive technique and offers enough quality of statistic data of the material's structural parameters [80].

X-rays are electromagnetic waves, oscillating, that propagate through space. When these waves hit the material's atoms, the charges, nucleus and electrons, vibrate due to the electric field's vibration. With high frequency, the X-rays are capable of exiting the electrons and, when atoms are regularly spaced in a crystalline reticulate and when incident radiation has a wavelength in the same order as the spacing, there will be constructive interference in specific directions and destructive interference in other directions. The result of the beam-sample interaction is a part of the beam absorbed by the material, and other part diffracted, forming a 2θ angle (scattering angle or diffraction angle) with the incident beam [80-83].

Bragg proposed a model to explain the nature of the diffraction, called Bragg's law. This model establishes the necessary condition (specific geometric relation), but not enough, for a beam of X-rays, incident over a set of planes (*h k l*), to be diffracted. Follows the model shown by Bragg:

$$n \ \lambda = 2 \ d_{hkl} \ sen(\theta) \tag{2}$$

where:

λ : Wavelength of the incident beam

d_{hkl}: Interplanar distance of the set of planes (h k l);

θ : Beam angle in relation to the plane;

n: Diffraction order, value of 1, 2, 3, ... [80-87].

There is another condition that must be obeyed for diffraction to occur in an X-ray beam: the structure factor to be different from zero. This factor depends on the atomic scattering factor and is associated to the number of electrons of the atom; it also depends on the Miller indexes of the plane that diffracts and the arrangement of each atom in the unitary cell [80-82].

The X-ray diffraction patterns are obtained through monochromatic beams (only one frequency) and are presented in function of the diffraction angle 2θ and the intensity, being that the intensity is the energy of a beam measured by the unit of area and the unit of time [80-82]. Nowadays, the intensity measurement is usually done by counting the number of photons in a detector [84]. The diffraction patterns obtain structural information of the sample, making it possible to identify the lattice parameter of the crystal and the phases present in the sample [80,81,85].

Indexing the diffraction peaks means finding which crystallographic plane is responsible for each peak. Materials previously characterised through this technique are listed in a diffractogram catalogue (called JCPD files); in this way, it is possible to identify the peaks of your material based on the ones catalogued [80,81].

Analysis can be done in X-ray diffraction results and offer a lot of information about the studied material, such as:

- Average Crystallite size;
- Crystalline lattice microstrains;
- Distribution of the average crystallite size;
- Average dislocations density;
- Dislocation characteristics;
- Planar defect density; and
- Phase transformation.

In Table 6 are described the possible types of analysis to be realised in diffractograms and which the parameters are used [88].

The average crystallite size and the microstrain present in the crystalline structure of the metal in analysis determine the form and width of a diffraction pattern. Being that the regions named as crystallites are small blocks that show the same crystallographic orientation, as shown in Figure 12, they are grouped forming a zone of coherent diffraction [82,88,89]. The microstrain is produced by a distribution of traction and compression short-range forces in the network. The microstrain generated in the crystallites may arise due to several sources, such as defects, dislocations, vacancies and shear planes [82].

Table 6 – The utilisation of the provided parameters from a diffractogram in the diffraction pattern analysis.

Method	Identification	Position	Intensity	Form	Displacement
Indexing	Cell parameters	X			
Phase analysis	Quantification and identification	X	X		
Peak displacement analysis	Residual tensions				X
Microstrain, average crystallite size, lattice defects	Pattern analysis	X		X	
Structure refinement	Atomic positions, Debye-Walter factor, other ones	X	X	X	

Source: Adapted from Ichikawa (2013) [88].

Figure 12 - Schematic drawing of the block structure.
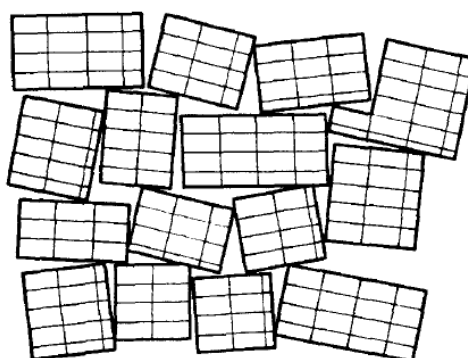
Source: Cullity (1978)[84].

Ichikawa (2013) in its work showed the effect of the crystallite size in the diffraction patterns, as can be seen in Figure 13, and one can observe that the smaller average crystallite size, the wider is the peak [88].

Figure 13 - Simulation of the diffracted intensity of a crystal in parallelepiped form altering the size of its edges and, consequently, the crystallite size (Ni).
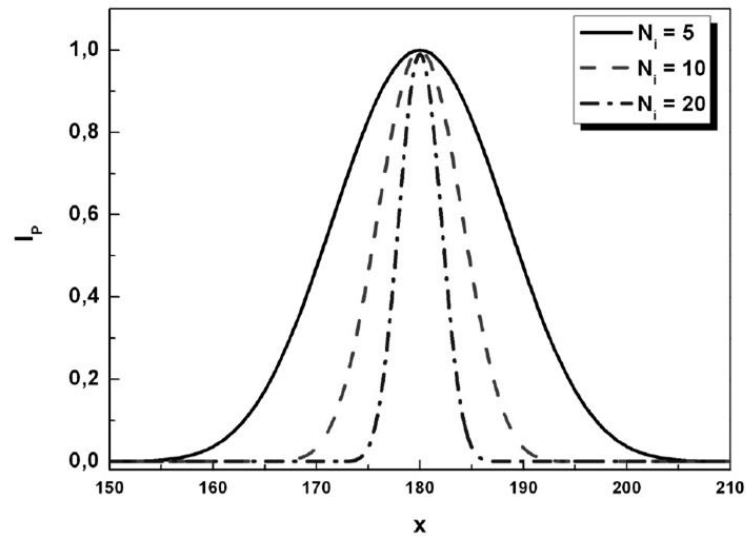
Source: Ichikawa (2013) [88].

As well as the average crystallite size, the material's cold work will impact in the diffraction patterns, where the deformation will lead to broadening and displacement of the diffraction maximums when compared to an annealed material, Figure 14 shows schematically the effect of cold work. These changes allow studies such as the determination of internal tensions and SFE through X-ray diffraction [81].

Figure 14 - Effect of deformation in position and width of the diffraction maximums.
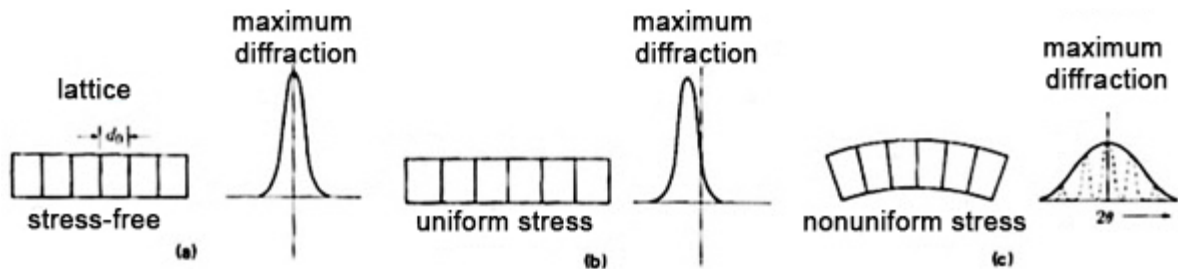
Source: Padilha and Ambrozio Filho (2004) [81].

Phase transformation can be observed through diffraction patterns, for austenitic stainless steels, which are susceptible to martensitic transformations at low temperatures. The study through X-ray diffraction techniques is of extreme importance for quantification and determination of present phases since the conventional microscopy techniques are not enough to identify stress-induced martensites [4,14,15].

3.5.1 Synchrotron Source

For X-ray generation, besides the X-ray tubes, that are small and cheap dispositives, there are also big types of equipment allocated in big laboratories, which present very high costs, these X-rays produced with more significant energy are called "synchrotron light" [80].

The X-rays tubes produce relatively low-intensity rays; in this way, a typical X-ray figure is obtained in 20 to 40 minutes. A reduction in time and analysis and an increase in the measured signal is possible using synchrotron light sources, or synchrotron radiation. These sources are composed by electron accelerators and a set of equipment that produce radiation [80,84].

In Brazil, there is an electron accelerator ring installed in the Brazilian Synchrotron Light Laboratory (LNLS) located in the city of Campinas-SP, as is shown in Figure 15. This source that produces very high-intensity radiation is composed of basically four parts: linear electron accelerator, transport line, electron storage ring and light lines. Being that, the linear accelerator injects electrons in the circular accelerator which stores them for a certain amount of time and in determined times (due to the beam intensity decay) there is reinjection of these electrons previously accelerated into the storage ring. The most diverse types of equipment are willing in these light's lines that utilise this machine as a radiation source [80,90].

Figure 15 - Synchrotron ring at the LNLS, Campinas-SP.

Source: UVX, CNPEM [90].

Sets of electromagnets disposed along the circular accelerator are responsible for keeping the electrons in an approximately circular trajectory [80,84]. The light's lines are willing tangentially to the ring because when the electrons are accelerated radially, they emit radiation tangentially to this curve. The wavelength of

the radiation will depend, mainly, of the electrons velocity and the curvature's radius of the ring [80].

The synchrotron radiation is better due to several factors, such as bigger X-ray intensity, smaller wavelength (which implies in a bigger number of reflections), more significant quality of results, besides allowing the tests to be done *in situ*.

3.6 INTEGRATIVE REVIEW

Metal processing at cryogenic temperature is studied in order to obtain improvements in mechanical properties, such as ductility and mechanical resistance, from materials already commercialised and well known, only altering deformation temperature. The study of cryogenic deformation is relatively new and is being studied by a significant number of researchers. However, until this moment, most studies focus on utilising pure materials to understand the microstructural evolution phenomena without the influence of carbides and second phase precipitation.

AISI 304 (austenitic) and 430 (ferritic) stainless steel are extensively commercialised and they are cheap steels when compared to other stainless steels. In this study, it is aimed to analyse the influence of temperature and strain rate in the processing of the studied steels, that can also be influenced by crystalline structure, starting grain size, SFE, phase transformation, second phase and carbide precipitation. By evaluating *in situ*, the microstructural evolution of these steels through X-ray diffraction it is possible to understand the changes in the deformation mechanisms and the microstructural rearrangements during deformation, without the influence of recuperation during sample preparation and without being necessary to extrapolate results, since most studies select a few points to do the tests.

This synchronism between deformation and result obtainment of the microstructural evolution is possible due to the XTMS station, which is equipped with a thermo-mechanical simulator and is coupled to the synchrotron light ring of the LNLS. The synchrotron light use allows more reliable data obtention than those obtained through common laboratory diffractometers because it presents bigger parallelism with the beam and bigger intensity of the diffraction peaks [91,92].

The analysis of the phenomena that occur during plastic deformation is even more attractive with the particularities of each studied steel. As the AISI 304 is austenitic stainless steel, there is also phase transformation when deformed, so this

study aims to even comprehend the influence of the parameters in this deformation mechanism. And the AISI 430, ferritic stainless steel, shows ductile-brittle transition due to the change in temperature and strain rate; this way, for this steel, there is another particularity to be studied. The comparison between the steels in the study shows great importance because they are both stainless steels, widely known and commercialised, however, show different crystalline structures, which can present different answers to the parameter variations, due to the differences of the acting phenomena, such as, for example, the deformation mechanisms.

4 MATERIALS AND METHODS

In this study, two stainless steels were used, one austenitic - AISI 304 - and the other ferritic - AISI 430 - the same ones were obtained from commercial sheets. Figure 16 below shows the experimental flowchart indicating the steps to get the samples and the methods of analysing performed.

Figure 16 - Flowchart of the steps to obtain the samples and the methods of analysis used.
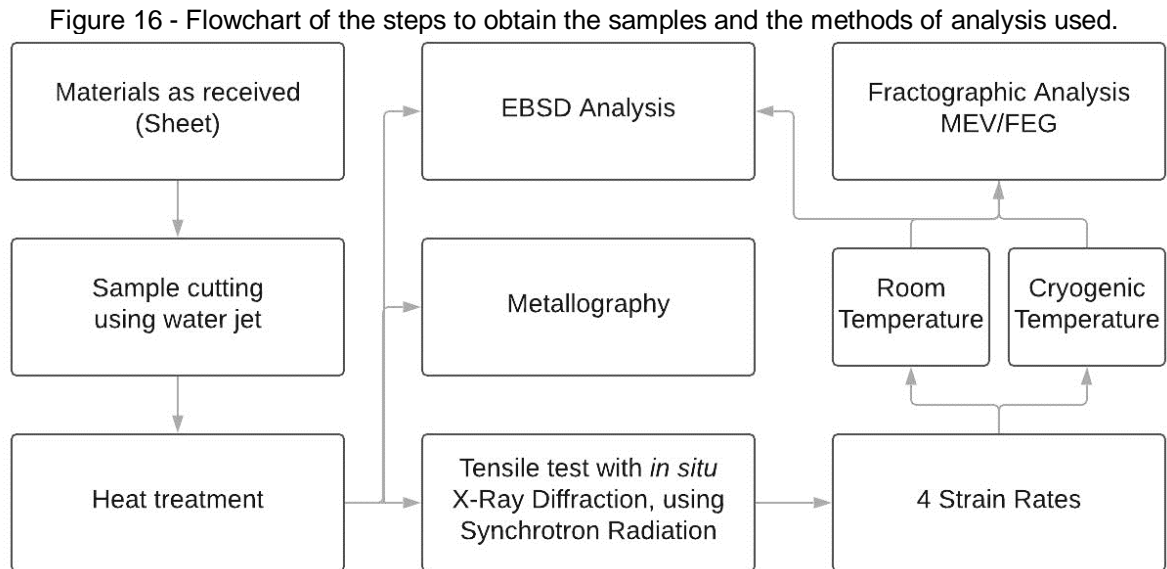
Source: The author.

4.1 MATERIALS

The chemical compositions of the stainless steels under study were analysed using the optical emission spectrometer, brand SHIMADZU, model PDA 7000, from the laboratory of the Federal University of Technology - Paraná, Ponta Grossa campus. Table 7 shows the chemical compositions of both steels.

Table 7 - Chemical composition (% in weight) of stainless steels AISI 304 and AISI 430.

	C	Mn	Si	P	S	Cr	Ni
AISI 304	0.06	1.27	0.47	0.014	0.00015	16.78	7.94
AISI 430	0.06	0.29	0.39	0.017	0	15.69	0,37

Source: The author.

4.2 EXPERIMENTAL METHODS

4.2.1 Sample Cutting

For test running in the Gleeble 3S50® thermo-mechanical simulator, a device was needed in order to hold the samples in the equipment's claws; it was necessary to use smaller samples to improve the system's adjustment, the schematic drawing is shown in Figure 17. Samples were cut from the original sheet using water jet. All the samples showed 40 mm in length and 14 mm in width, as shown in Figure 17. The thickness varied from one steel to another, for the AISI 304 the average thickness was 0.55 mm and 1 mm for the AISI 430.

Figure 17 - Sample dimensions, in millimeters.
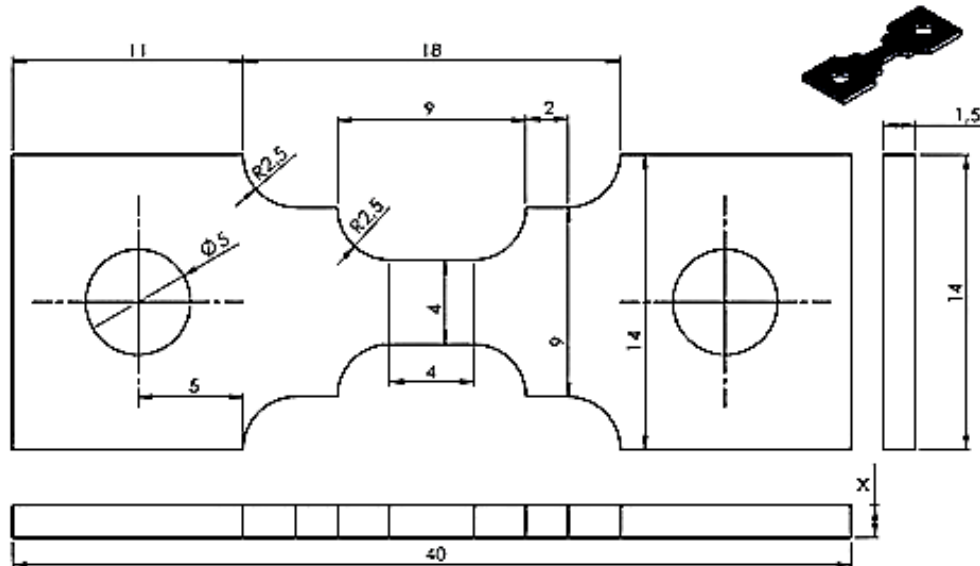
Source: The author.

The device used in the Geeble 3S50® is presented in Figure 18, it was responsible for allowing the cooling of samples until cryogenic temperatures. Cooling was made through liquid nitrogen that runs through the hoses that are coupled to the copper piece, being that this piece is responsible for conducting the temperature to the sample that is fixed with duplex stainless-steel bars.

Figure 18 - Sample, device and claws of the Gleeble 3S50® thermo-mechanical simulator.
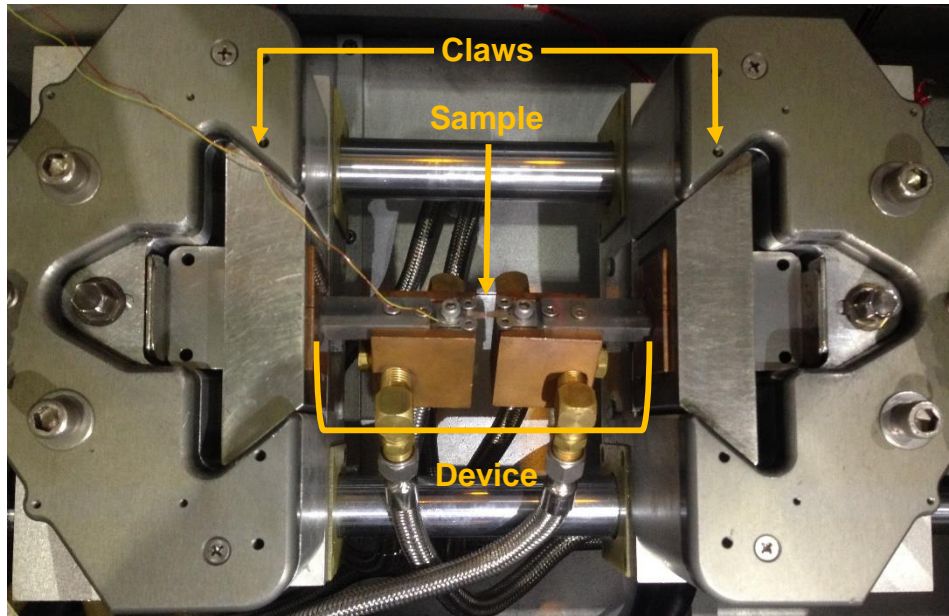
Source: The author.

4.2.2 Heat Treatment

In Table 8, we can see the indicated temperatures to obtain a tension-free structure, and with equiaxial grains. The heat treatments were needed due to the materials that had been received in sheet form and went through water jet cutting. Then, the samples went through annealing with the times and temperatures shown in Table 8. The temperatures were chosen based on the midpoint of the suggested temperature range and oven capacity.

Table 8 - Annealing temperatures and times used.

Steel	Indicated Temperature	Used Temperature	Time
AISI 304	1010º C – 1120º C	1050º C	15 minutes
AISI 430	705º C – 790º C	750º C	15 minutes

Source: Information taken from Washko and Aggen (1990)[6], and Douthett (1991)[93].

The recrystallization time was 15 minutes due to the thickness and small size of the samples, which allow a rapid homogenization of temperature.

4.2.3 Tensile Testing with X-Ray Diffraction, *in situ,* using Synchrotron Radiation

4.2.3.1 *Tensile test*

The mechanical tests were done simultaneously with X-ray diffraction tests; which was possible due to the XTMS (X-ray Scattering and Thermo-Mechanical Simulation Station) for test realisation. The station is located in the second bay of the XRD1 line of the synchrotron ring of the Brazilian Synchrotron Light Laboratory (LNLS - *Laboratório Nacional de Luz SÍncrotron*) installed in the Brazilian Centre for Research in Energy and Materials (CNPEM - *Centro Nacional de Pesquisa em Energia e Materiais*) as shown in Figure 19. The XTMS has a thermo-mechanical simulator Gleeble 3S50® and an acquisition and instrumentation system design exclusively for synchrotron ring operation [91,92].

Figure 19 - XRD1 synchrotron ring line image.
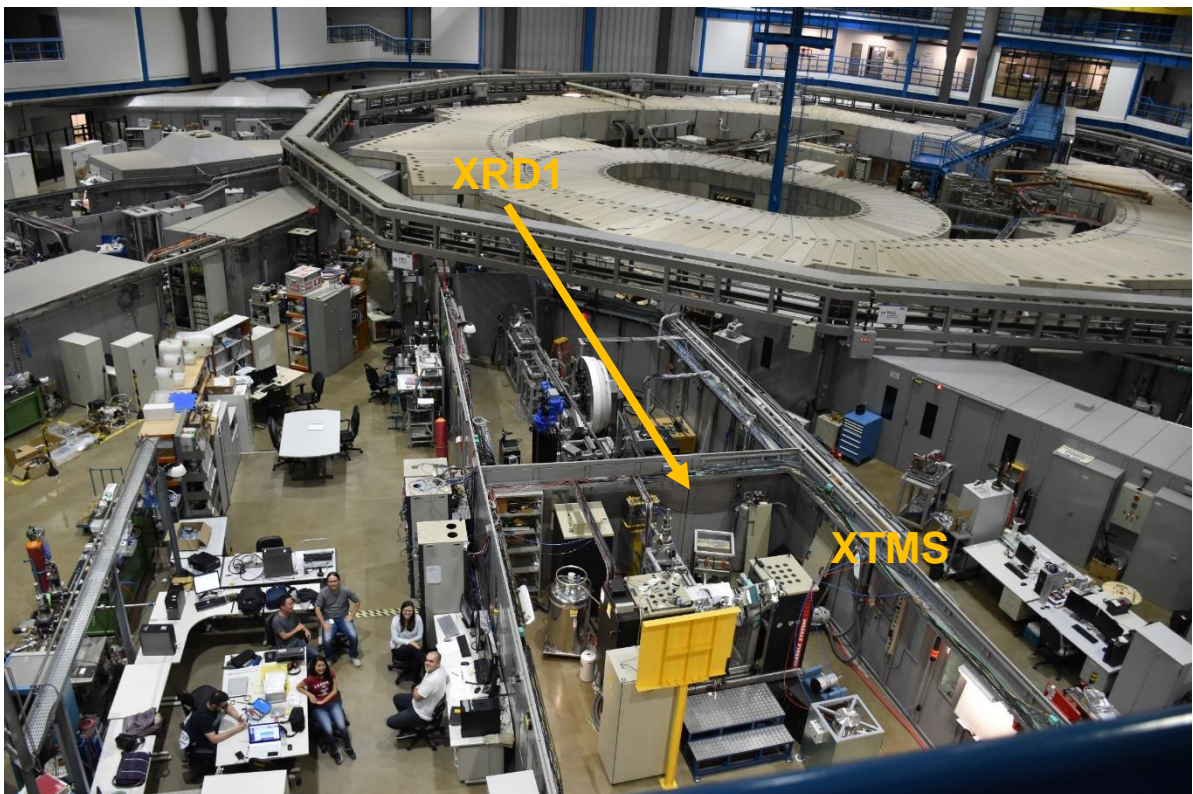
Source: The author.

Testing was performed in a vacuum atmosphere to avoid the ice formation due to cooling, which, if present, can interfere in the obtained data. The tension and deformation are applied and controlled through the claws symmetrical movement.

Strain is controlled through the claw's position (due to its displacement) or using a laser non-contact dilatometer, and the load is controlled using a 44 kN load cell with 0.1 kN resolution [92].

To reach below -170°C temperatures cooling system was used, as presented in Figure 18. The system consists of a duplex stainless-steel support, where the sample is fixed, that is coupled to the claws of the thermo-mechanical simulator. In the device, there is a copper piece that is responsible for conducting the temperature to the sample. The low temperature comes from the flux of liquid nitrogen that goes through the copper piece; the liquid nitrogen gets to the piece through the hoses coupled to the system.

Tensile tests under room temperature (24°C) and at cryogenic temperatures (between -170 and -180°C) were realised, and, in each temperature, four different strain rates were used, those are shown in Table 9.

Table 9 - Strain rates and temperatures used.

	SR 1	SR 2	SR 3	SR 4
Room Temperature	1.3×10^{-3} s^{-1}	5.0×10^{-4} s^{-1}	2.8×10^{-4} s^{-1}	1.2×10^{-4} s^{-1}
Cryogenic Temperature	1.3×10^{-3} s^{-1}	5.0×10^{-4} s^{-1}	2.8×10^{-4} s^{-1}	1.2×10^{-4} s^{-1}

Source: The author.

The AISI 430 stainless-steel was also deformed at cryogenic temperatures (CT) with a strain rate of 6.6×10^{-2} s^{-1} in order to obtain additional information. This test was realised in the mechanical testing laboratory of the Materials Engineering Department of UEPG (DEMa – UEPG), using the brand and model equipment: Shimadzu AG-I 10 kN. Due to the sample size and necessity of cooling them, the device shown in Figure 20 was used. As shown in Figure 20 (b), a Styrofoam cup was used to allow the submersion of the samples in liquid nitrogen during tensile testing.

Figure 20 - The device utilised in the UEPG mechanical laboratory.
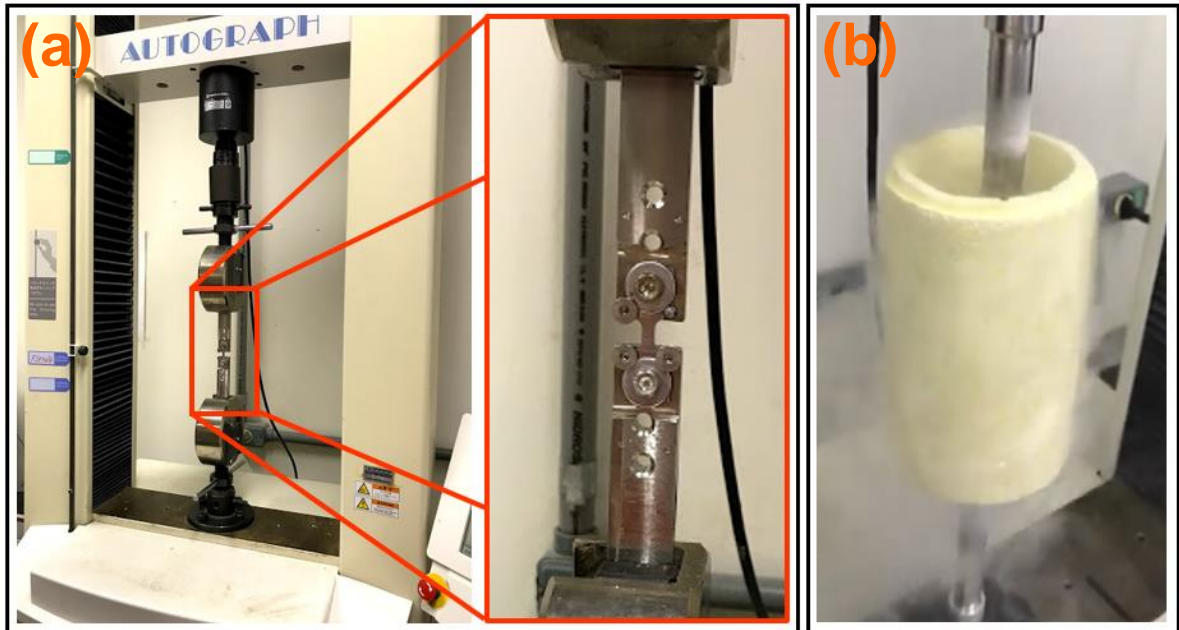
Source: The author.

For analysis of the mechanical behaviour stress versus engineering and true strain graphs were used. The engineering graphs used the following equations of stress and engineering strain:

Engineering Stress,

$$\sigma_e = \frac{F}{A_0}$$ (3)

where:

σ_e: Engineering Stress,

F: Applied load and

A_0: Area of the initial transversal section.

Engineering Strain,

$$\varepsilon_e = \frac{\Delta l}{l_0}$$ (4)

where:

ε_e: Engineering Strain,

Δl: Length variation and

l_0: Initial length.

For the stress versus true strain graphs the following equations were used:

True stress,

$$\sigma_r = \sigma_e(1 + \varepsilon_e) \tag{5}$$

where:

σ_r: True stress,

σ_e: Engineering stress and

ε_e: Engineering strain.

True strain,

$$\varepsilon_r = \ln(1 + \varepsilon_e) \tag{6}$$

where:

ε_r: True strain and

ε_e: Engineering strain[14].

In the stress versus engineering strain graphs, the mechanical resistance values were analysed, yield strength, ultimate tensile strength, total strain, ductility and homogeneous strain extension.

To analyse the cold work during the test's evolution, it was opted to examine the work-hardening rates x true strain. This rate was obtained through the true stress x true strain derivative graph [11,21,94].

4.2.3.2 *In situ X-ray diffraction at the XTMS line*

As mentioned before, the XTMS line allows us to do mechanical tests along with X-ray diffraction tests simultaneously. The Gleeble 3S50® thermo-mechanical simulator is responsible for the mechanical testing part, and for the X-ray diffraction measurements a system for acquisition and instrumentation was exclusively designed for the XTMS line. The developers are: *Dynamic Systems Inc.* (DSI), group of Metals Characterisation and Processing Laboratory (CPM) of the LNNano (Brazilian Nanotechnology Laboratory) and technical engineering team of the LNLS[92].

The synchrotron ring has a capacity of storage of 1.37 GeV and current injection of around 250 mA. There are two silicon monochromators installed in the XTMS line. The incident radiation has an energy of 12 keV and wavelength of λ=

1.0332 Å. When it goes through the sample, the incident beam on the sample has an average width of 1.2 mm (vertical direction) and 3.6 mm (horizontal direction). The incident beam control is done with an X-ray beam position meter and a gap system of high resolution. The additional size and position control of the beam can be done using optical elements in the XRD1 beamline [92].

The goniometer is mounted in a table with freedom of movement in the x, y and z directions, as shown in Figure 21, allowing a highly reliable alignment between the goniometer's rotation axis and the illuminated point of the sample. The detectors are mounted on a support, as shown in Figure 21 and 22, that moves along the goniometer's arm, altering the distance between the detector and the sample, and the positioning on the desired angular band. The chamber's lid is at 280 mm of the sample and has an X-ray transparent window. The window covers a 130° angle band, and the 2θ angle a vary between -5° and 125° [91,92].

The system has two linear Mythen 1K detectors, with a pixel size of 50 μm x 8mm mounted in bands of 1280 pixels. The station also has at disposal Rayonix SX165CCD area detectors. The distance from the detector to sample varies from 361 to 600 mm. Each Mythen 1K detector covers a band of approximately 9.15°, with a minimum gap between detectors of about 0.5° [92].

K type thermocouples, with a resolution of approximately 0.2°C were fixed on the samples to allow temperature control during testing. The temperatures reached around -170°C to -180°C during testing at cryogenic temperatures in this work.

The diffraction patterns were collected in 3 seconds, and the temperatures and rates used for each sample are described in Table 9. In order to remove the instrumental influence, the peaks widths were adjusted based on the yttria pattern measured with the same system. For the data synchronisation between X-ray diffraction with tensile testing, the data obtained in both results were applied to IgorPro® software, which synchronises the start of the test. In the same software, the peak adjustment for diffraction was adjusted with a Gaussian function.

Figure 21 - Illustrative figures of the possible table movements, from the goniometer and from the detectors.
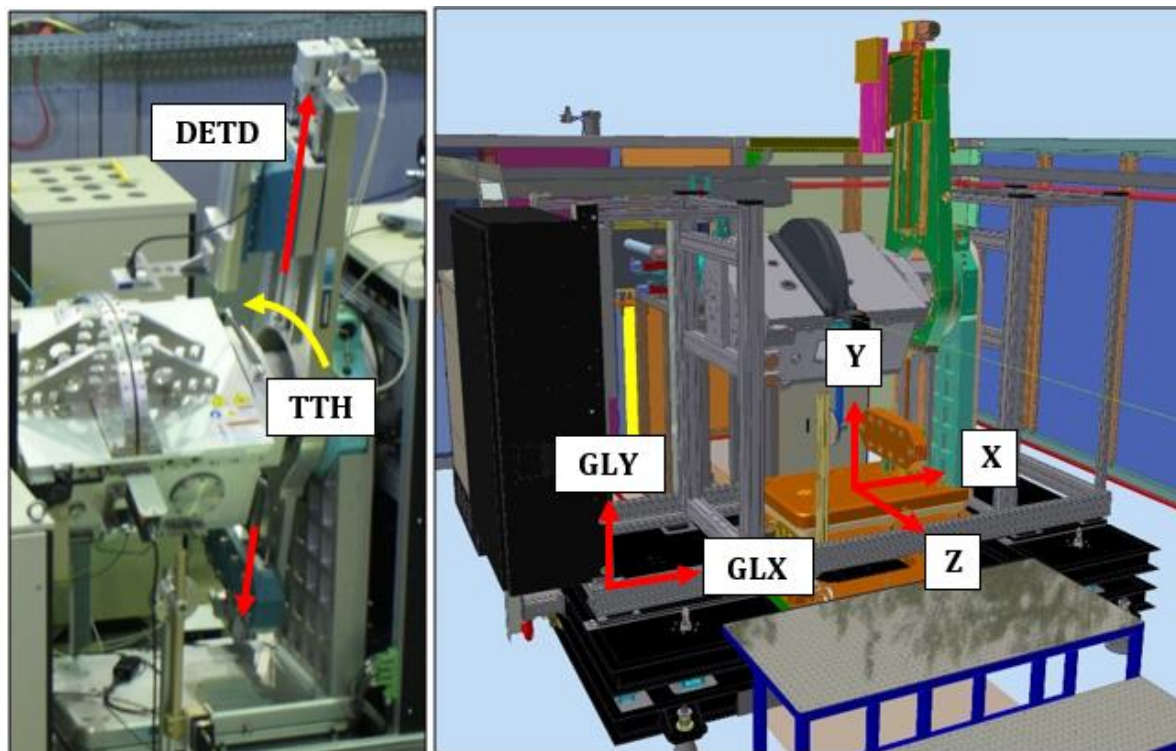
Source: XTMS Experimental Station User's Guide (2017) [91].

Figure 22 - Superior part of the chamber and detectors.
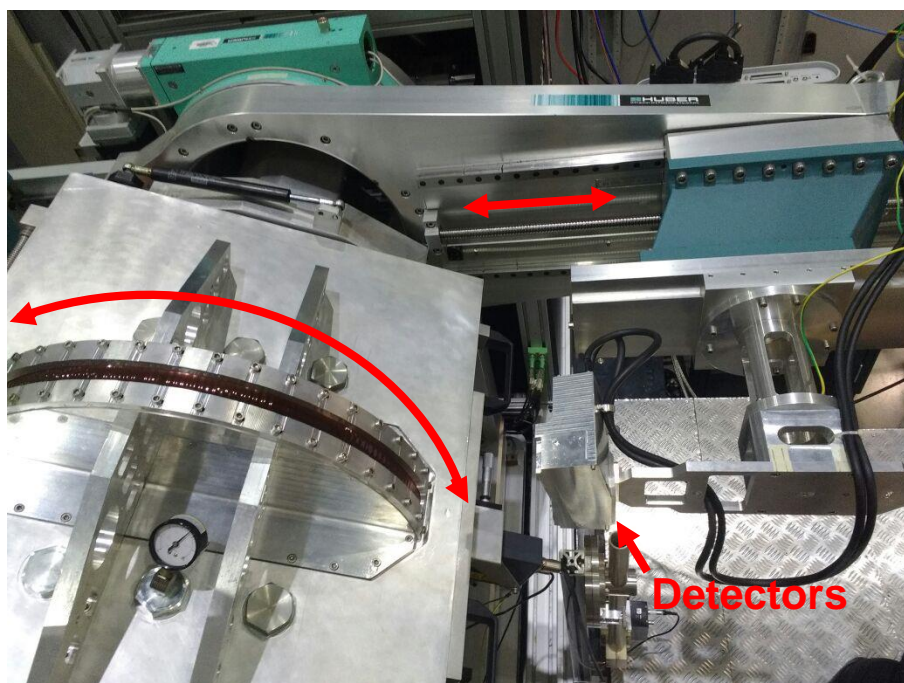
Source: The author.

The diffraction surface changes through the experiment, due to dimensional variation caused by temperature and applied strain; in this way, it is necessary to realise the position correction. The temperature change is not considered in this work, because it stays constant through the whole test. The correction equations are:

$$\Delta(2\theta) = \tan^{-1}(\varepsilon \frac{t}{g} \frac{\sin 2\theta_{obs}}{\sin \omega}) \tag{7}$$

where:

$\Delta(2\theta)$: Diffraction angle corrected position;

$2\theta_{obs}$: Observed angle;

t: Sample thickness;

ω: Incident beam angle;

ε: Sample strain;

g: Distance between the detector centre and irradiated region of the sample [84,95,96].

To understand the microstructural evolution, two parameters obtained by X-ray diffraction were analysed, them being: microstrain and average crystallite size. The microstrain ε was estimated by the stokes and Wilson formula, according to the equation:

$$\varepsilon = \frac{\beta \cos \theta}{4 \sin \theta} \tag{8}$$

where:

β: Width of diffraction peaks at half height;

θ: Diffraction angle [96-99].

The crystallite size D is obtained by the Sherrer equation:

$$D = \frac{0.94\lambda}{\beta \cos \theta} \tag{9}$$

where:

λ: Wavelength;

β: Width of the diffraction peaks at half height; and

θ: Diffraction angle [84,95].

For a quantitative estimation of the volume fraction of the martensite phase in the austenitic stainless steel during plastic deformation, the principle where the integrated total intensity of all diffraction peaks for each phase is proportional of this phase volume fraction [23,82,84,100,101]. With this it was possible to obtain the variation of each phase volume fraction, austenite and martensite, present in the AISI 304 steel. The equation proposed by Matsumura[101] (*et al.*), that describes the phase transformation curves, was used, as follows:

$$V_\alpha = 1 - \left(\frac{V_{\gamma_0}}{1 + (\frac{k}{q})V_{\gamma_0}\,\varepsilon^q} \right) \tag{10}$$

where:

V_α: Volume fraction of stress-induced martensite;

V_{γ_0}: Initial austenite volume fraction;

ε: Plastic strain;

k and q are constants determined through the curve adjusted from experimental data [23, 101].

Additional analysis were done using the conventional diffractometer from the UEPG's Multiuser Laboratory Complex (C-LabMu), Ultima IV – Rigaku, using Cu Kα1 and Cu Kα2 radiation operating at 40 kV and 30 mA at a scan speed of 1^0 min^{-1}. Further analysis were required because of the high results of martensite volume fraction at the beginning of tests using the XTMS.

4.2.4 Fractographic Analysis – SEM/FEG

For the stainless-steels fracture surface analysis a field emission scanning electron microscope was used (SEM/FEG), model MIRA3®, from TESCAN, installed in the UEPG's Multiuser Laboratory Complex (C-LabMu).

Using images obtained with the SEM/FEG and with aid from the Image J® software it was possible to obtain the fracture area values, the area reduction was calculated, given by the equation:

$$q = \frac{A_o - A_f}{A_o} \tag{11}$$

where:

A_o: Starting Area,

A_f: Final Area [39].

Being that, the **q** value can be multiplied by 100 so we can obtain the percentage of reduction in area value (%RA).

4.2.5 Metallographic Analysis

For the metallographic preparation, grinders of 150 to 1500 mesh were used to remove the sample's deeper marks. And the polishing was carried out in an electrolytic polishing system model Eletromet 4, from Buehler®. The composition of the electrolytic solution used for the two steels was:

- 940 mL ethyl alcohol (P.A),
- 6 mL distilled water and
- 54 mL perchloric acid ($HClO_4$) [102].

The modified Beraha II metallographic reagent was used, which composition is described below:

- 80 mL distilled water;
- 40 mL hydrochloric acid (HCl);
- 4.8 grams ammonium bifluoride (NH_4)HF_2;
- 1 gram potassium metabisulfite ($K_2S_2O_5$) [103].

The microstructural development was performed by immersion, immediately after electrolytic polishing, lasting from 30 to 120 seconds.

In order to improve the delineate grain boundaries and twins, the electrolytic etching with nitric acid (HNO_3) was chosen. The solution used was:

- 60 ml nitric acid (HNO_3);
- 40 mL distilled water [102].

The combination of these two etching solutions was also used.

Microstructural analysis was performed using the Olympus model BX - 51M optical microscope.

5 RESULTS AND DISCUSSION

5.1 MICROGRAPHS

Microstructural analysis was performed initially with the modified Beraha II reagent. Figure 23 shows the sample micrographs of AISI 304 steel, after recrystallization, in three different magnifications.

Figure 23 - AISI 304 steel micrograph, after recrystallization. Electrolytically polished. Modified Beraha II. Using Nomarski filter.
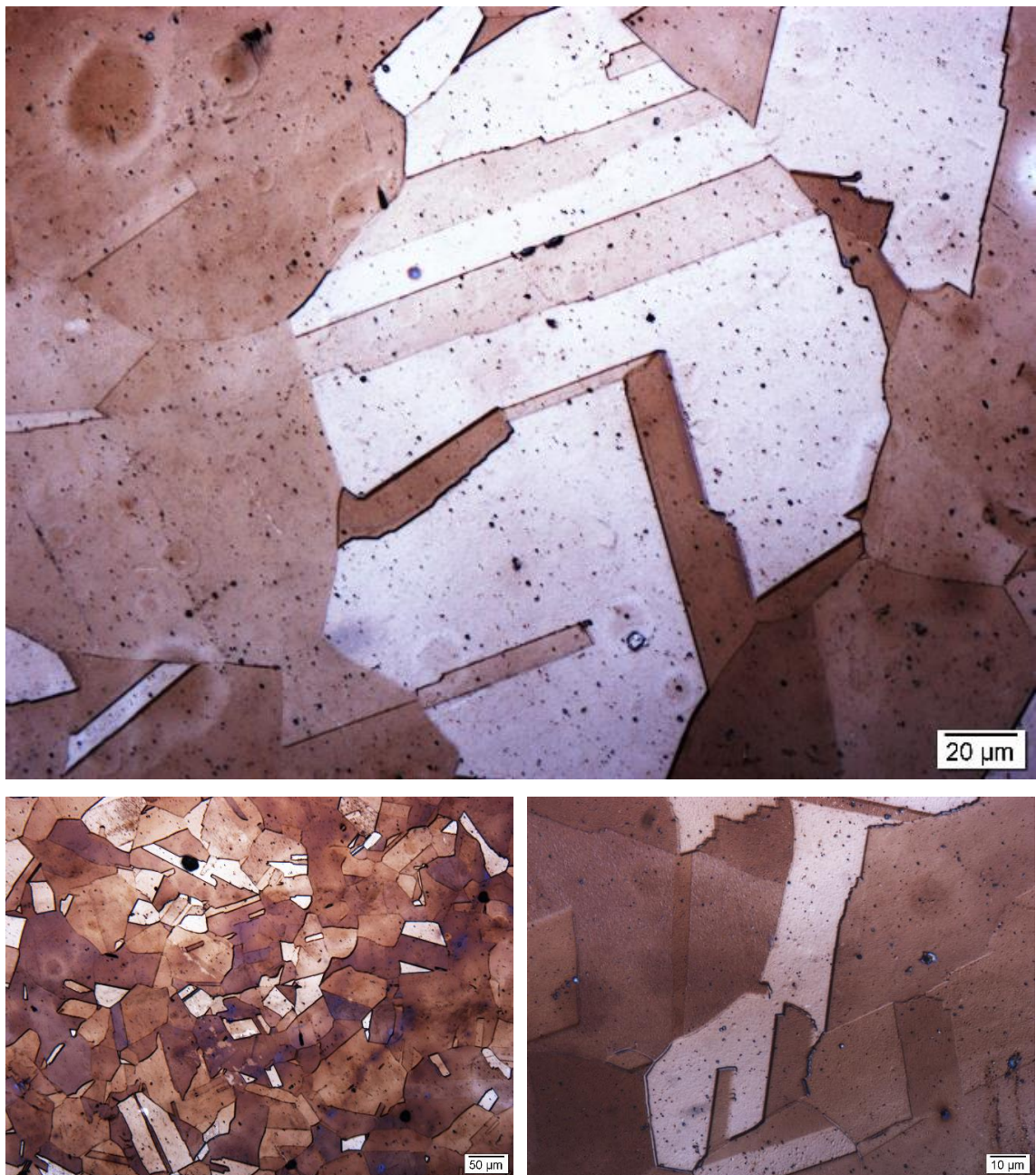
Source: The author.

To reveal the grain boundaries of AISI 304 steel, long times were taken, close to 120 seconds, which caused, at some points, elevated corrosion.

In order to obtain well-delineated grain boundaries to be able to perform grain size analysis, electrolytic etching with nitric acid was used. Figure 24 shows AISI 304 result by electrolytic etching with HNO_3, presenting well delineated grains boundaries and twins. With this etching, there are sample regions where the corrosion was stronger, as such in Figure 25. In order to improve Beraha etching, previous electrolytic etching with HNO_3 was used, such as in Figure 26.

Figure 26 shows the grain boundaries of the austenitic steel and the presence of annealing twins. Precipitation of the $M_{23}C_6$ carbide may occur on heating the annealed material. At high temperatures, such as that used in the treatment of recrystallization of this material, the $M_{23}C_6$ carbide forms in grain contour as small spherical particles; thus this carbide can be present. The δ ferrite phase may be present; however, with the etching used, it could not be identified.

Figure 24 - AISI 304 steel micrograph, after recrystallization. Electrolytic Etching with HNO_3. Parameters: 25 s and 1.1 A

Source: The author.

Figure 25 - AISI 304 steel micrograph in regions with strong corrosion effect. Electrolytic Etching with HNO_3. Parameters: 25 s and 1.1 A. Using Nomarski filter.

Source: The author.

Figure 26 - AISI 304 steel micrograph, after recrystallization. Electrolytic Etching with HNO_3, followed by etching using modified Beraha II. Parameters: 15 s and 1.1 A. Using Nomarski filter.

Source: The author.

Figure 27 - AISI 430 steel micrograph, after recrystallization. Electrolytically polished. Modified Beraha II. The rolling direction is indicated in the figure.
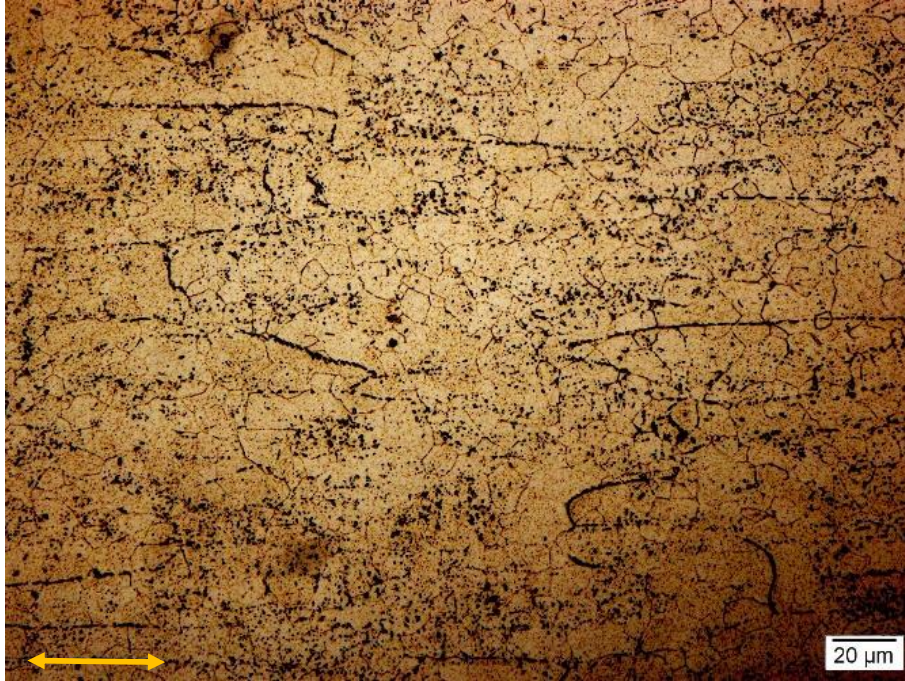
Source: The author.

In the same way, as for AISI 304, the nitric acid was used in AISI 430 to grain boundaries print. Figure 28 shows the well-delineated grain boundaries for AISI 430, in three different magnifications. The larger image has the same magnification as Figures 24 and 25; thus, it can see that the heat treatment used for AISI 430 resulted in smaller grain size when compared to AISI 304.

One point to be noted is the successful electrolytic etching using nitric acid in both materials. The mix between this technique and conventional print showed up promising.

Figure 28 - AISI 430 steel micrograph, after recrystallization. Electrolytic Etching with HNO₃. Parameters: 20 s and 1.2 A.
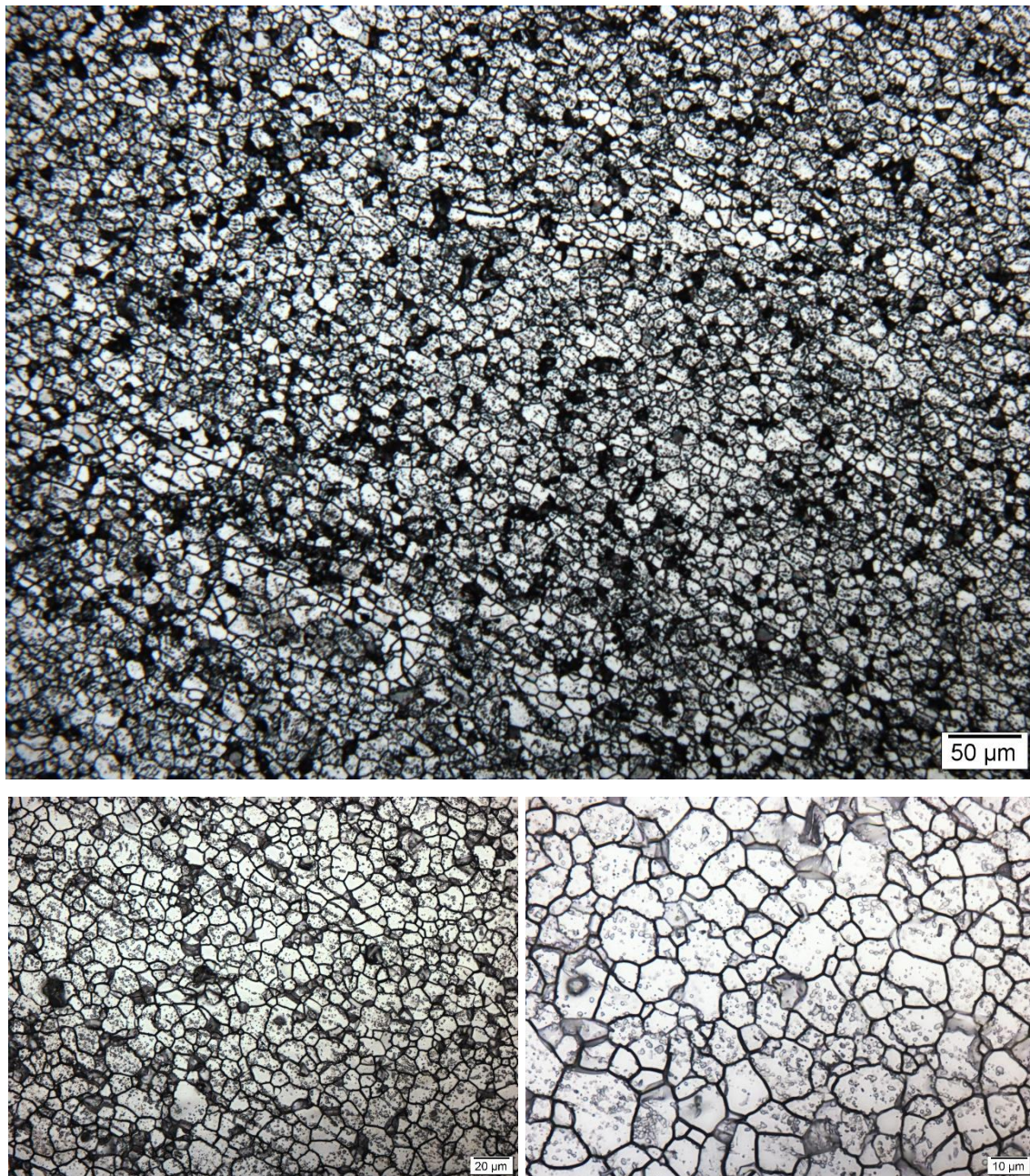
Source: The author.

5.2 INITIAL CONDITIONS CHARACTERISTICS

To complement the starting material characterisation, the average hardness value was measured by microindentation following standard test method ASTM E 384. The test executed on the LEICA microindentation hardness measuring equipment, model VHMT MOT. The distance between a marking and another respected three times the marking diameter, as requested by the standard. The AISI 430 steel result, after recrystallization, was 161 HV, 1.4 HV standard deviation. For AISI 304 steel, it was obtained 171 HV, 3,7 HV standard deviation [104,105,106].

The initial samples average grain size, after recrystallization, were measured using the 3-circumference method of standard ASTM 112-13 [104,107]. In both steels samples, an electrolytic attack was made in nitric acid solution to reveal the grain bordering. AISI 430 steel presents, on average, grain diameter of 8.14 µm (0.35 µm standard deviation), with an ASTM 11-grain size number. For AISI 304 steel the average value of the grain diameter is 46.69 µm (3.81 µm standard deviation), ASTM 6.

Using the empirical formula of Schramm and Reed [108], which follows bellow, the SFE was calculated to AISI 304 steel, and its result was 13 mJ.m^{-2}.

$$\gamma = -53 + 6.2\%Ni + 0.7\%Cr + 3.2\%Mn + 9.3\%Mo \qquad (12)$$

Images by diffraction electron backscattered diffraction (EBSD) were obtained in SEM/FEG electronic microscope (the same used for fracture analysis), to characterise the initial materials, Figures 29 and 30, 1.87 Hz acquisition speed of approximately, and 0.7 µm step scan.

Figure 29 shows that in the austenitic stainless steel initial condition, the presence of the phase of face-centred cubic and body-centred cubic, FCC and BCC, respectively. The microscope software used provides phase quantification of images, the results presented in Table 10. This analysis shows that the AISI 304 steel, in its initial condition, gives approximately 76% austenite (FCC phase) and 19% of BCC phase, which may be α'-martensite and δ ferrite. This result represents only an image analysis and not the whole material.

Figure 29 - AISI 304 stainless steel initial condition EBSD images.
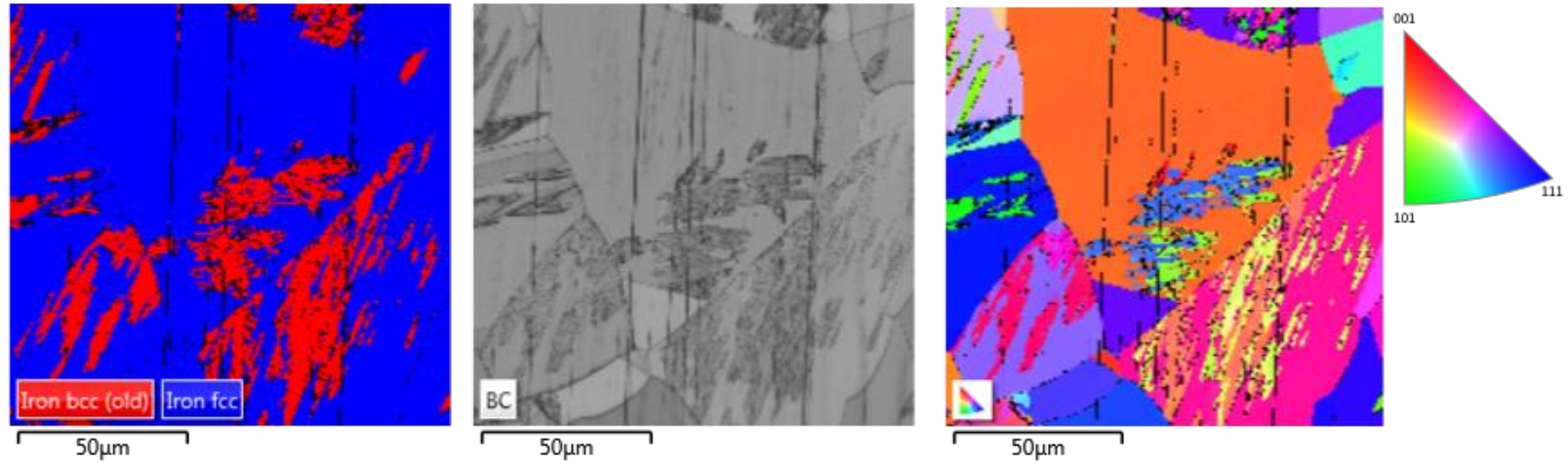
Source: The author.

Figure 30 - AISI 430 stainless steel initial condition EBSD images.
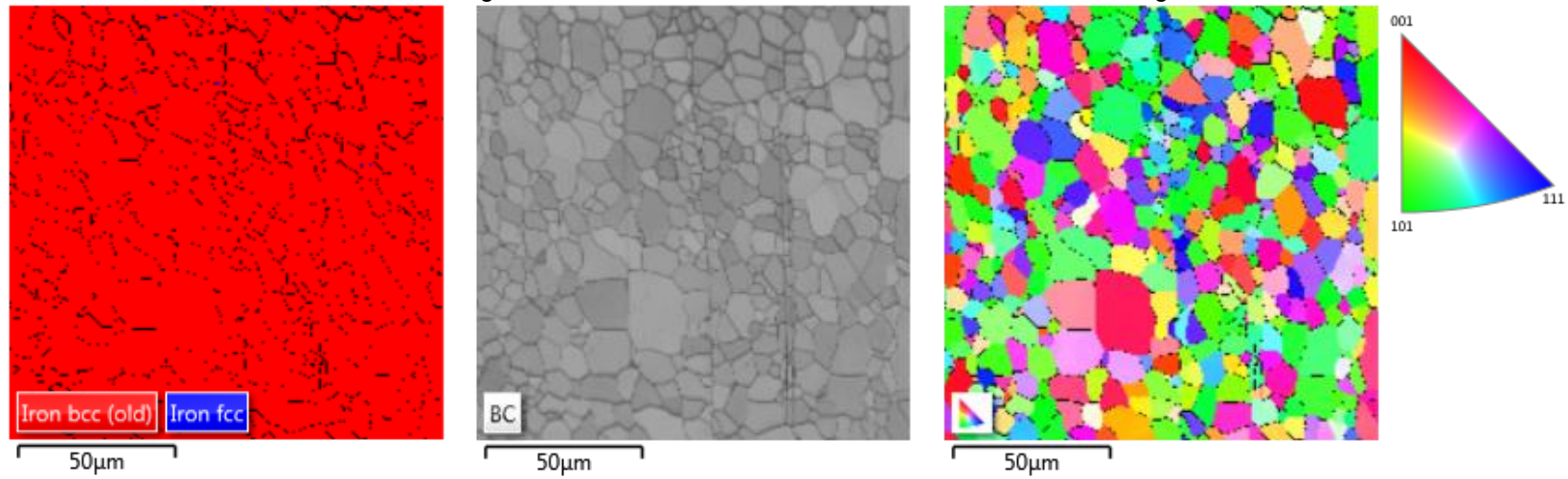
Source: The author.

Table 10 – Phases percentages obtained in the EBSD images of the initial conditions of the AISI 304 and AISI 430.

	FCC	BCC	Zero resolution
Phase fraction AISI 304	76.0	18.9	5.1
Phase fraction AISI 430	-	95.1	4.9

Source: The author.

An EBSD image of the AISI 430 stainless steel, in its initial condition, is shown in Figure 30, and the fractions of the phases are presented in Table 10. Thus, we have that the ferritic stainless steel is entirely composed of the BCC phase, as expected. EBSD did not identify chromium carbides, or they were too small to be detected.

5.3 MECHANICAL RESULTS

5.3.1 AISI 304

XTMS experimental station performed the mechanical tests of uniaxial traction with X-ray diffraction measurements at the same time. The strain values considered the position of the claws since the values obtained with the non-contact laser dilatometer did not present satisfactory quality.

Figure 31 shows the AISI 304 steel tensile curves obtained at room temperature (RT) at the different strain rates used, and Figure 32 shows the curves at cryogenic temperature. Based on the stress-strain graphs, it was possible to obtain the ultimate tensile strength values, total elongation, rupture stress and uniform elongation for all strain rates in both temperatures. Table 11 shows the results and the mechanical data of all the tests performed in AISI 304. The yield strength was not evaluated because of the strain calculated on the claw displacement values; in this case, there was interference of the system's accommodation in the data obtained at the tests beginning.

Observing the mechanical response when the strain rate changes at room temperature, it can be said that there is not an evident influence of the strain rate on the behaviour. The 2.8×10^{-4} s^{-1} strain rate is the rate with the highest total elongation and the top uniform elongation, with 0.14 and 0.12 mm/mm ranges, respectively. The

test with 5.0×10^{-4} s^{-1} strain rate resulted in the highest ultimate tensile strength value and rupture stress, with 103 and 57 MPa ranges, respectively.

Figure 31 - Engineering stress-strain curves of AISI 430 steel in four different strain rates utilised at room temperature.
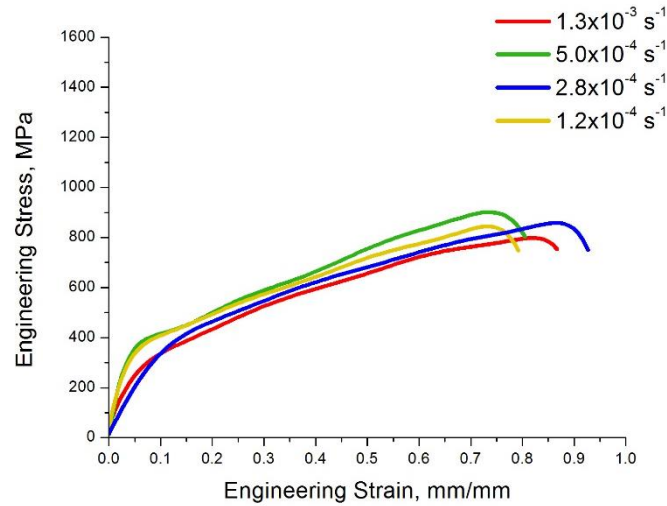
Source: The author.

Table 11 - Mechanical tests results of AISI 304 steel samples, at room and cryogenic temperatures.

		Rupt. Stress σ_r (MPa)	Average σ_r	Total Elong. (mm/ mm)	Average TE	UTS (MPa)	Average UTS	Unif. Elong. (mm/ mm)	Average UE
Room Temperature	1.3x10^{-3}	755		0.87		799		0.82	
	5.0x10^{-4}	804	764	0.80	0.85	902	851	0.74	0.79
	2.8x10^{-4}	751		0.93		859		0.86	
	1.2x10^{-4}	747		0.79		844		0.74	
Cryogenic Temperature	1.3x10^{-3}	1276		0.51		1500		0.46	
	5.0x10^{-4}	1348	1273	0.37	0.42	1577	1516	0.33	0.38
	2.8x10^{-4}	1223		0.43		1471		0.40	
	1.2x10^{-4}	1246		0.37		1515		0.33	

Source: The author.

Some researches, such as of Talonen[94,109], *et al.* (with $3x10^{-4}$ s^{-1}; 10^{-1} s^{-1} and 200 s^{-1} strain rates), Tsuchida[21], *et al.* (with ten strain rates ranging from 10^3 s^{-1} to $3.3x10^{-5}$ s^{-1}), Yoo[110], *et al.* (with $1.6x10^{-4}$, 10^{-3} s^{-1} and 10^{-2} s^{-1} strain rates), Das and Tarafder[111] (with five strain rates ranging from 10^{-4} s^{-1} to 1 s^{-1}), and Park[112], *et al.* (with $1.6x10^{-4}$ s^{-1}, $1.0x10^{-3}$ s^{-1} and $1.0x10^{-2}$ s^{-1} strain rates), found that the increase of strain rate in room temperature tests caused a more significant effect on ductility than on mechanical resistance. In general, the increase in strain rate caused losses of total and uniform elongation.

These authors explain that this result is the reply to higher adiabatic heating that higher rates can provide. However, the strain rate effect is stronger in strain rates above 10^{-3} s^{-1}, being that, in some studies, the strain rate impacts are not so evident. In Yoo[110], *et al.* and Park[112], *et al.* works, the strain rate also varied at cryogenic temperature, and with the temperature reduction, the strain rate influence was more explicit.

Figure 32 - Engineering stress-strain curves of AISI 430 steel in four different strain rates utilised at cryogenic temperature.
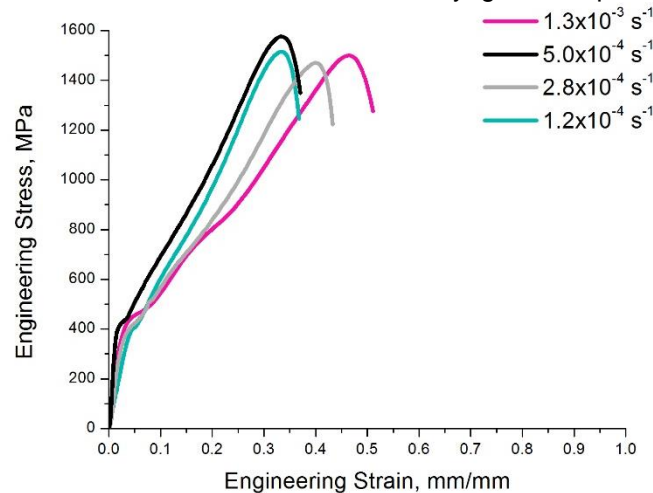
Source: The author.

At the cryogenic temperature (CT), when the strain rate was changed (Figure 32), disregarding the $5.0x10^{-4}$ s^{-1} rate, the results show a comportment influence, with the slower strain rate resulting in lower total elongation and lower uniform elongation, with 0.14 and 0.13 mm/mm ranges, respectively. Concerning the ultimate tensile strength, the $5.0x10^{-4}$ s^{-1} strain rate presented the highest value, and $2.8x10^{-4}$ s^{-1} presented the lowest value, the amplitude of the result was 106 MPa. The strain rate

influence in both temperatures was not also so clear due to the proximity in the strain rates values.

In Park[112] and Yoo[110] researches, at cryogenic temperature, the most distressed property was the ultimate tensile strength, with higher strain rates presenting lower values. Thereby, considering only the extremes strain rates, 1.3×10^{-3} s^{-1} and 1.2×10^{-4} s^{-1}, ultimate tensile strength (UTS) decreased by 45 MPa with increasing strain rate.

When analysing the temperature influence, the influence in mechanical properties is apparent, as it is better compared in Figure 33, in which at low temperatures there is a ductility loss and strength increase.

By comparing the average rupture stress result in both temperatures, a considerable increase of 67% was obtained when the material was deformed at cryogenic temperature. By analysing the average elongation obtained at each temperature, it can be observed a loss of more than 50% in the total elongation. When evaluated the temperature influence on the UTS, an increase of more than 78% occurs for those deformed at cryogenic temperature. However, there is a great loss of uniform elongation at this temperature, of around 50%.

Figure 33 - Engineering stress-strain curves of AISI 304 steel at room and cryogenic temperatures in 5×10^{-4} s^{-1} strain rate.
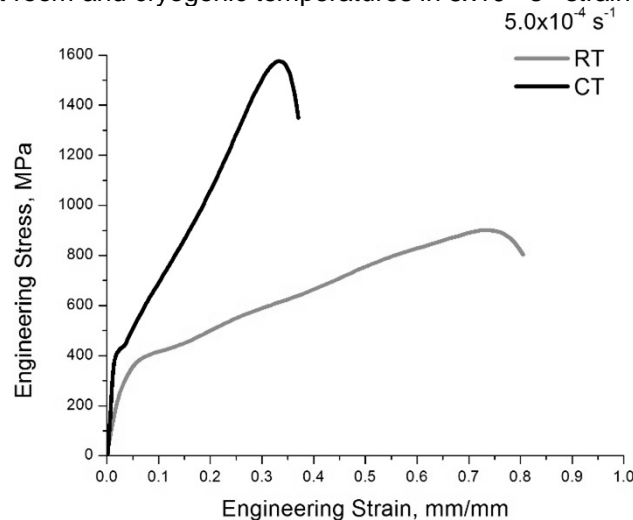
Source: The author.

At cryogenic temperature, it was possible to verify the slope change in the stress-strain curve. CT has a sigmoidal behaviour during plastic strain, due to the secondary hardening from the martensitic transformation. At room temperature, this behaviour was not visible, because with temperature increase there was a

suppression of strain-induced martensite induced formation, being that the rising temperature leads to austenite stability increase, related a higher SFE [11, 17, 21,110,111,112,113].

Other austenitic stainless steels researches show similar results, as Park[112] *et al.*, Das e Tarafder[111], Yoo[110] *et al.*, Tsuchida[21] *et al.*, Lee[113] *et al.*, Talonen [11] and Hecker[17], *et al.*

For a better understanding of temperature effects on mechanical behaviour, the work-hardening rate (WHR) variation during deformation was analysed, for the same strain rate at room and cryogenic temperatures (Figure 34). It can be observed that the work-hardening rate is profoundly affected by temperature, and with increasing temperature, the second hardening effect reduced, due to an SFE increase and a chemical driving force $\Delta G^{\gamma \to \alpha'}$ reduction. At room temperature, the WHR peak occurs at higher values of true strain and presents lower value.

Figure 34 - True stress and work-hardening rate as function of true strain in the AISI 304 steel at strain rate 5.0×10^{-4} s^{-1} at cryogenic and room temperature.
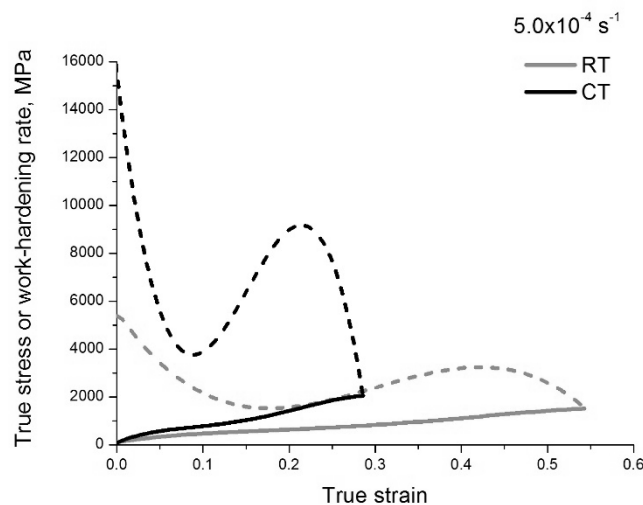
Source: The author.

Some authors describe the hardening rate effect on austenitic stainless steels in stages, part of them describe in three and others in four stages [11,114]. Talonen, in his work, verified that during the first stage, the hardening rate decreases rapidly, the motive of dynamic softening would be that strain was facilitated by the chemical driving force for the martensitic transformation. The end of stage I is in the minimum work-hardening rate and, at this point, stage II begins. In this new stage, there is an increase on the work-hardening rate, due to the effects of α'-martensite.

Being that there is generation of the geometrically necessary dislocations only up to the percolation threshold of the martensite. In stage III, the plastic deformation can no longer be fully accommodated by the plasticity only of the austenite, but also the α'-martensite must deform. With the martensite mechanical behaviour different from the austenite, a higher load is needed to deform the material. Thereby, the WHR keeps on increasing with increasing martensite volume fraction. Finally, stage IV onset is associated with the maximum WHR, and during stage IV, WHR decreased. In higher levels of strain, the α'-martensite phase is more important, because more volume fraction of this phase are present, becoming increasingly important. And then the aggregate behaviour is predominantly commanded by the α'-martensite phase. Thus, the plasticity and dynamic recovery of the martensite phase causes WHR to start to decrease.

In Figures 35 and 36, the variation in the hardening rate can be compared with the change in the strain rate. By observing only extreme rates, it can be seen that both at RT and CT, a strain rate increase causes an increase in true strain value where it was obtained the highest value of hardening rate. However, the differences between strain rates, do not present a clear tendency.

Figure 35 - True stress and work-hardening rate as function of true strain in the AISI 304 steel at various strain rates at room temperature.
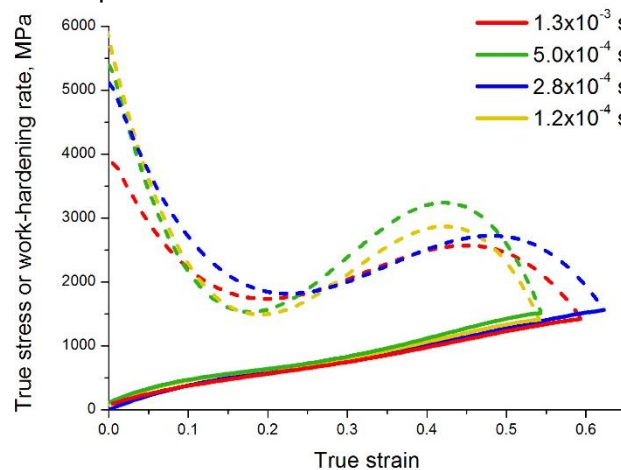
Source: The author.

Figure 36 - True stress and work-hardening rate as function of true strain in the AISI 304 steel at cryogenic temperature at various strain rates.
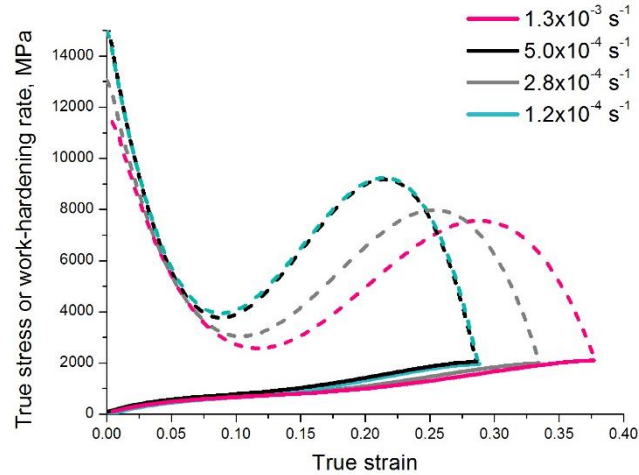
Source: The author.

5.3.1.1 *Electron backscatter diffraction (EBSD)*

Besides of figures of AISI 304 steel's initial condition, there were also obtained figures of the samples after deformation, by electron backscatter diffraction, using a scanning electron microscope (SEM). Figures 37 and 38 show AISI 304 deformed at room and cryogenic temperatures, respectively. The step scan was 0.08 µm, in all images.

At room temperature, it can be seen a significant presence of the BCC phase (α'-martensite) and a little FCC phase (austenite), in addition to a large part not indexed that is the result of high dislocations quantities due to deformation. At cryogenic temperature, it can also be seen that a large part is not indexed, and there is significant presence of the BCC phase, but, in this case, there is an even smaller amount of the FCC phase. Phases fraction obtained by Oxford software confirm these proportions, as shown in Table 12.

Table 12 – Phases percentages obtained in EBSD images of the AISI 304 after deformation at room and cryogenic temperatures.

	FCC	BCC	Zero resolution
RT	1.5	34.2	64.3
CT	0.1	28.2	71.7

Source: The author.

Figure 37 - AISI 304 stainless steel EBSD images after deformation at room temperature with 5x10^{-4} s^{-1} strain rate.
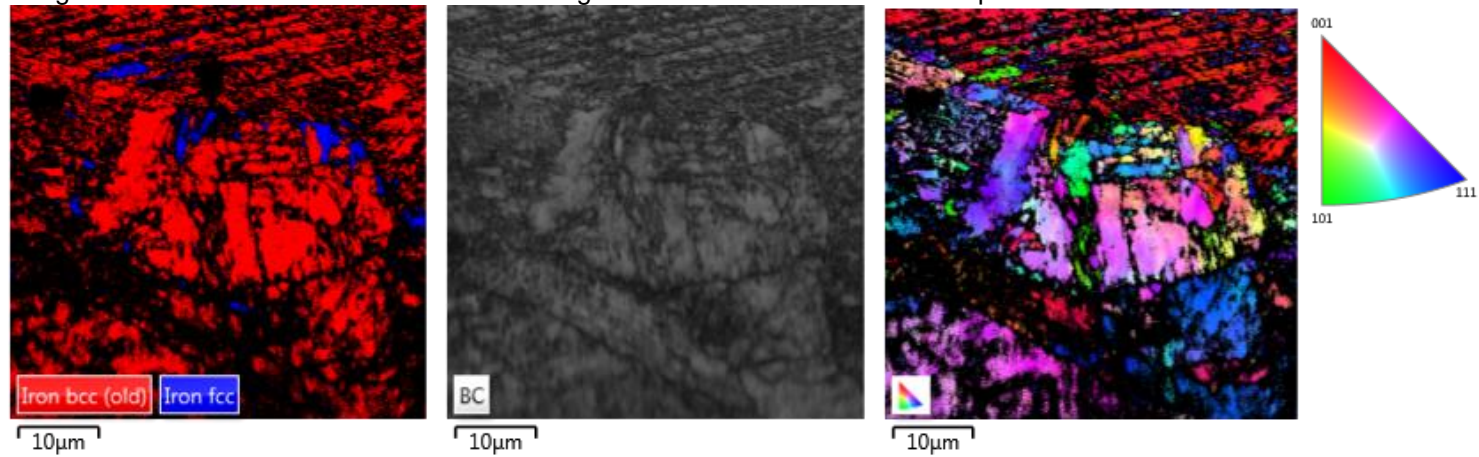
Source: The author.

Figure 38 - AISI 304 stainless steel EBSD images after deformation at cryogenic temperature with 5x10^{-4} s^{-1} strain rate.
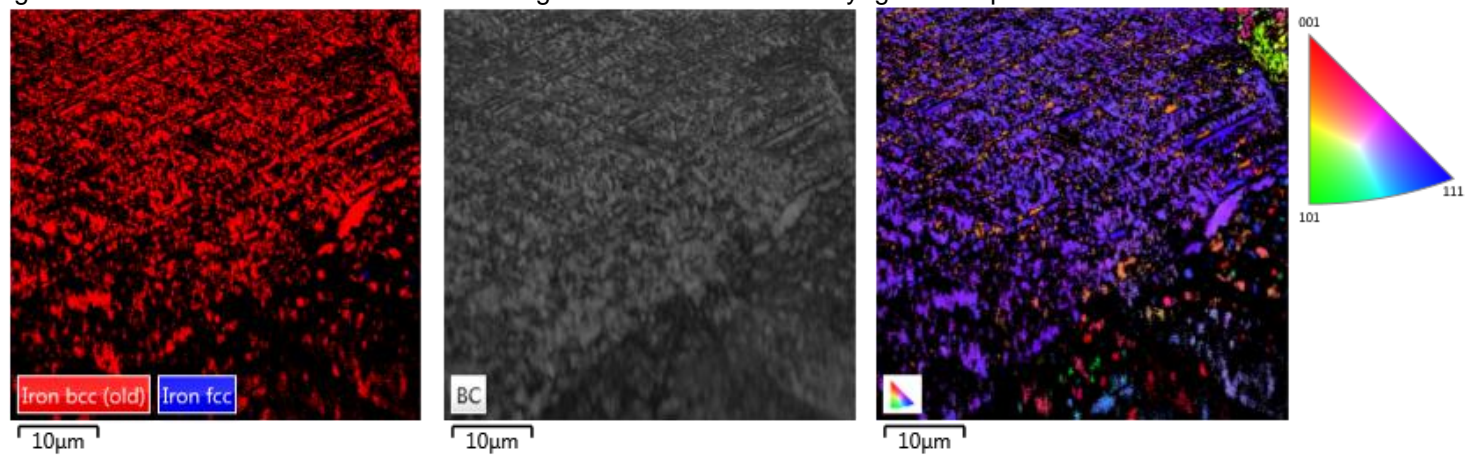
Source: The author.

These results show that at cryogenic temperature, there was a more significant amount of transformed martensite amount and higher energy storage through dislocations (superior zero resolution).

5.3.2 AISI 430

For the ferritic stainless steel, it is not expected a significant strain rate sensibility at room temperature, but the influence of strain rate increases with decreasing temperature and vice versa. At low strain rates and high temperatures, there is an increase in the athermal component of stress that tends to reduce the visible effect of strain rate and temperature, and when the thermal part is stronger, in higher strain rates and low temperatures, thermal variations become more influential. A reduction in temperature causes an increase in yield stress (YS) and ultimate tensile strength (UTS). The effects of an increase in strain rate have a similar impact of decreases in temperature. The behaviour changes because it increases resistance to dislocation motion and can vary the active slip system as well as its handling, depending on temperature and strain rate. At low temperatures or high strain rates, there is difficulty in moving screw dislocations due to energy barriers, interstitial impurities, or thermally activated conversions of screw dislocations [115-122].

Figure 39 - Engineering stress-strain curves of AISI 430 steel in four different strain rates utilised at room temperature.
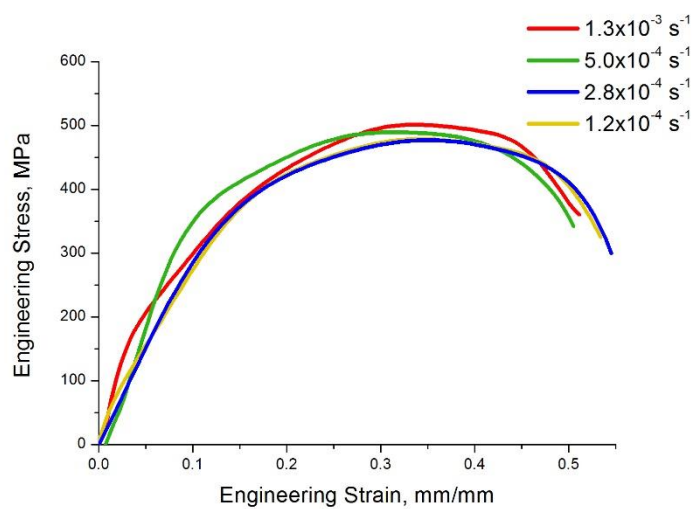
Source: The author.

Table 13 - Mechanical tests results of AISI 430 samples, at room and cryogenic temperatures.

		Rupt. Stress σ_r (MPa)	Average σ_r	Total Elong. (mm/mm)	Average TE	UTS (MPa)	Average UTS	Unif. Elong. (mm/mm)	Average UE
Room Temperature	$1.3x10^{-3}$	36		0.51		502		0.34	
	$5.0x10^{-4}$	343	332	0.51	0.52	490	487	0.31	0.33
	$2.8x10^{-4}$	300		0.55		477		0.35	
	$1.2x10^{-4}$	325		0.53		479		0.34	
Cryogenic Temperature	$6.6x10^{-2}$	879	-	0.23	-	947	-	0.17	-
	$1.3x10^{-3}$	627		0.41		803		0.27	
	$5.0x10^{-4}$	583	583	0.45	0.43	759	765	0.29	0.28
	$2.8x10^{-4}$	564		0.40		756		0.27	
	$1.2x10^{-4}$	557		0.46		744		0.31	

Source: The author.

Figure 39 shows engineering stress-strain curves of AISI 430 in all strain rates utilised at room temperature, and Table 13 shows the mechanical properties values from this chart (and also the results at cryogenic temperature). It can be noted a little influence of strain rates, with the increase in the strain rate there is a tiny increase in the UTS. The difference between the strain rates is more prominent when the values of strain rates are more distinct. About the yield stress, if we do not consider the strain rate of $1.3x10^{-3}$ s^{-1}, the strain rate influences shows the behaviour following the trend seen by other researchers. However, as mentioned before, the beginning of the tests was compromised from tension system accommodation. Thus, the YS analysis will not be considerate.

Figure 40 displays engineering stress-strain curves of AISI 430 in all strain rates utilised at cryogenic temperature. Considering only the strain rates defined at work initially $1.3x10^{-3}$ s^{-1}, $5.0x10^{-4}$ s^{-1}, $2.8x10^{-4}$ s^{-1} and $1.2x10^{-4}$ s^{-1}, in the engineering stress-strain curves is possible to observe the little strain rate effect in mechanical

behaviour, and this behaviour is similar to the one found at room temperature. Quicker strain rates promote higher UTS.

Figure 40 - Engineering stress-strain curves of AISI 430 steel at cryogenic temperature in four different strain rates pre-established and one new stain rate.
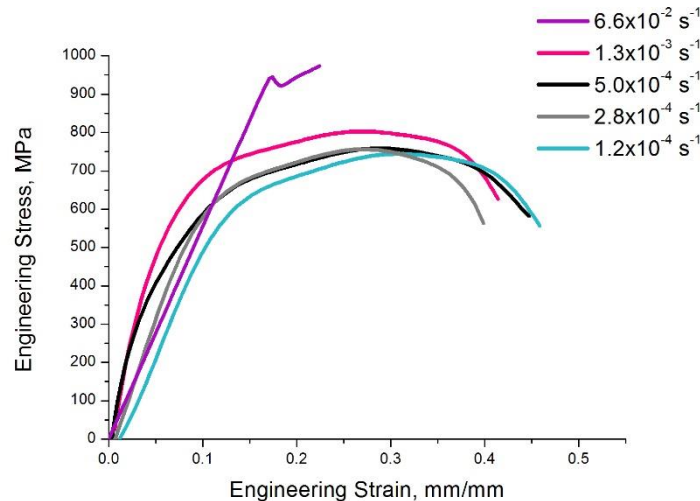
Source: The author.

When comparing the same strain rates in both temperatures, shown in Figure 41, it is possible to see a considerable increase in mechanical strength without significant loss of ductility, mainly in uniform elongation. It can be noted a significant increase of more than 75% in the UTS obtained when the material is deformed at cryogenic temperature and only approximately 15% of loss in total and uniform elongation. These results are ideal when we need a product with high resistance made by a stamping process, which requires high ductility.

Nevertheless, the expected was that at cryogenic temperature, AISI 430 would be fragile. The AISI 430 has a ductile-brittle transition (DBT), which can occur at temperatures as high as or higher than ambient. However, the DBT temperature depends on grain size, SFE, the presence or not of intermetallic phases or interstitially dissolved carbon/nitrogen [115,116,118,119,121,123,125]. The material AISI 430 utilised in this work has 8.14 µm grains size, and this probably is a reason that the ductile-brittle transition did not appear at cryogenic temperatures in the first four strain rates utilised.

Figure 41 - Engineering stress-strain curves of AISI 430 steel at room and cryogenic temperatures in 5×10^{-4} s^{-1} strain rate.
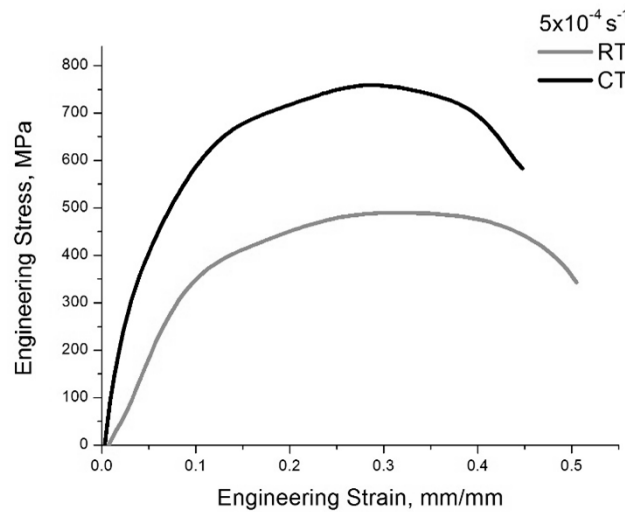
Source: The author.

Thus, one more strain rate was chosen to be tested at cryogenic temperature in the UEPG mechanical laboratory to confirm if only a faster strain rate would be enough to change the mechanical behaviour to fragile. The strain rate chosen was 6.6×10^{-2} s^{-1}, and it was able to overcome the point of ductile-brittle transition, as shown in Figure 40. Of course, it should be remembered that the cooling system in UEPG lab is different than used in XTMS, having a difference of minus twenty-Celsius degrees approximately, and this has an influence too. With this, it can be affirmed that strain rates utilised at cryogenic temperature were close to the ductile-brittle transition limit.

Following the same way as for the AISI 304 steel, work-hardening rate curves were made to AISI 430. Figures 42 and 43 show curves of true stress and work-hardening rate, as function of true strain in the AISI 430 steel, at various strain rates at room and cryogenic temperatures, respectively. In these graphs, the same behaviour was noted for all conditions. It can be seen that both at room and cryogenic temperatures there is no secondary hardening as in AISI 304. 2nd hardening does not occur because, in ferritic stainless steels, there is no phase transformation during the plastic deformation.

Figure 42 - True stress and work-hardening rate, as function of true strain, in the AISI 430 steel at various strain rates at room temperature.
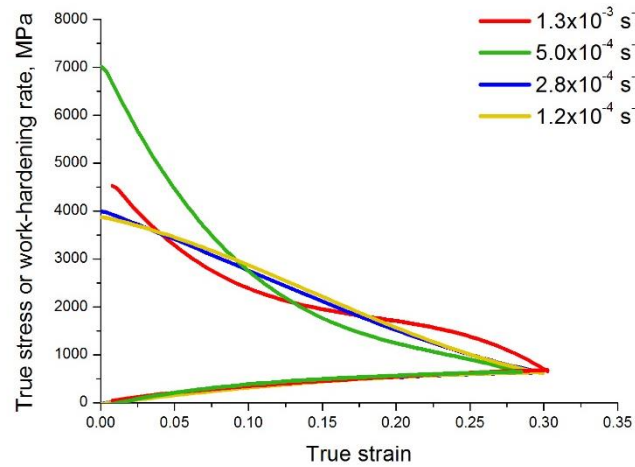
Source: The author.

Figure 43 - True stress and work-hardening rate, as function of true strain, in the AISI 430 steel at various strain rates at cryogenic temperature.
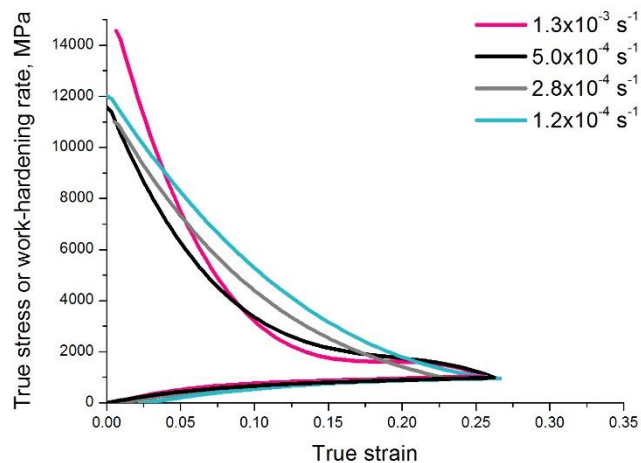
Source: The author.

Figure 44 shows the work-hardening rate at cryogenic temperature compared with the answer at room temperature, both at strain rate 5.0×10^{-4} s^{-1}. With this result, the effect is that at cryogenic temperature, there is more energy accumulated, presenting higher values of work-hardening rate, especially in the deformation beginning.

Figure 44 - True stress and work-hardening rate, as function of true strain in the AISI 430 steel, at strain rate 5.0×10^{-4} s^{-1} at cryogenic and room temperature.
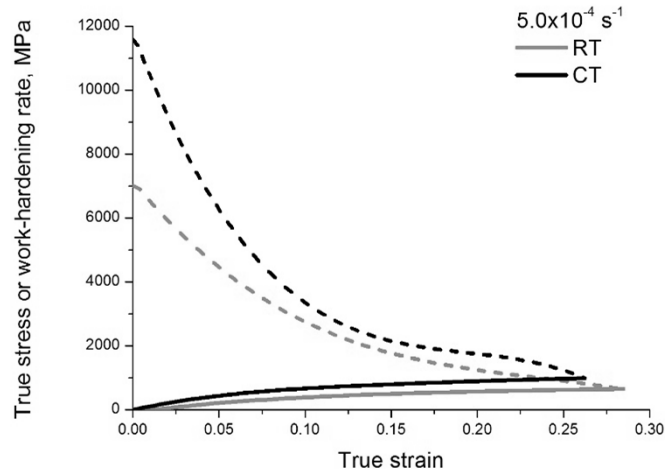
Source: The author.

5.3.2.1 *Electron backscatter diffraction (EBSD)*

In the same way as made for AISI 304, for AISI 430 there were made figures of the samples after deformation, for both temperatures, by electron backscatter diffraction. Figures 45 and 46 show the results of AISI 430 steel deformed at room and cryogenic temperatures, respectively. The step scan in all images was 0.08 µm. In addition, Table 14 shows the phase proportion for these samples. With the results at this strain rate, both the visual aspect and the phase proportion show the same effect; it can be seen that there are no significant differences between the sample deforming at cryogenic temperature and room temperature.

Table 14 – Phase percentage obtained in AISI 430 EBSD images after deformation at room and cryogenic temperatures. 5×10^{-4} s^{-1} strain rate.

	BCC	Zero resolution
RT	70.1	29.9
CT	69.4	30.6

Source: The author.

Figure 45 - AISI 430 stainless steel EBSD images after deformation at room temperature with 5x10^{-4} s^{-1} strain rate.
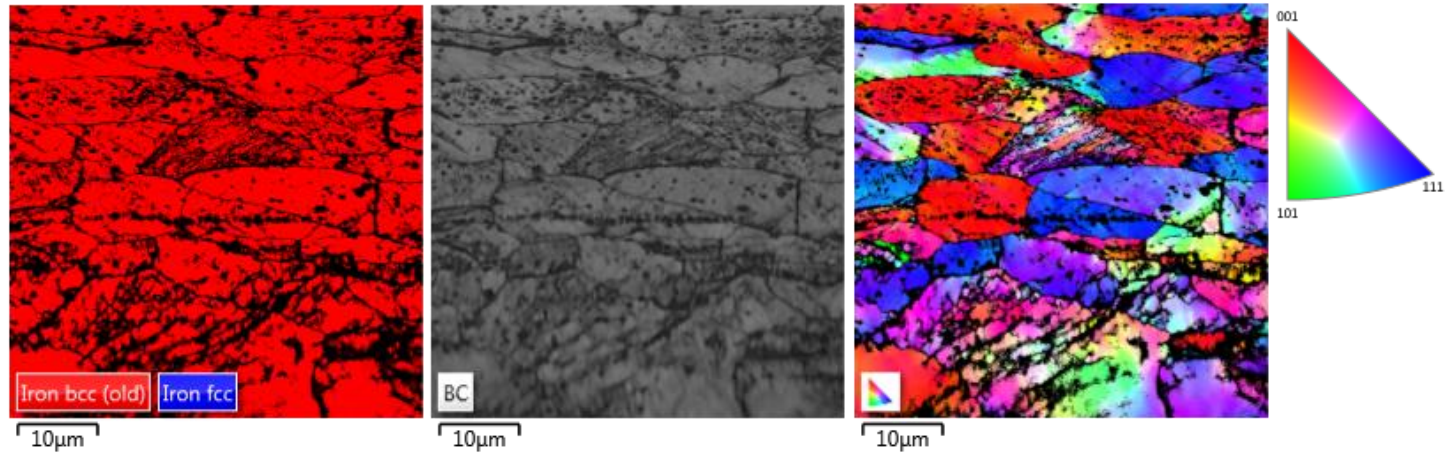
Source: The author.

Figure 46 - AISI 430 stainless steel EBSD images after deformation at cryogenic temperature with 5x10^{-4} s^{-1} strain rate.
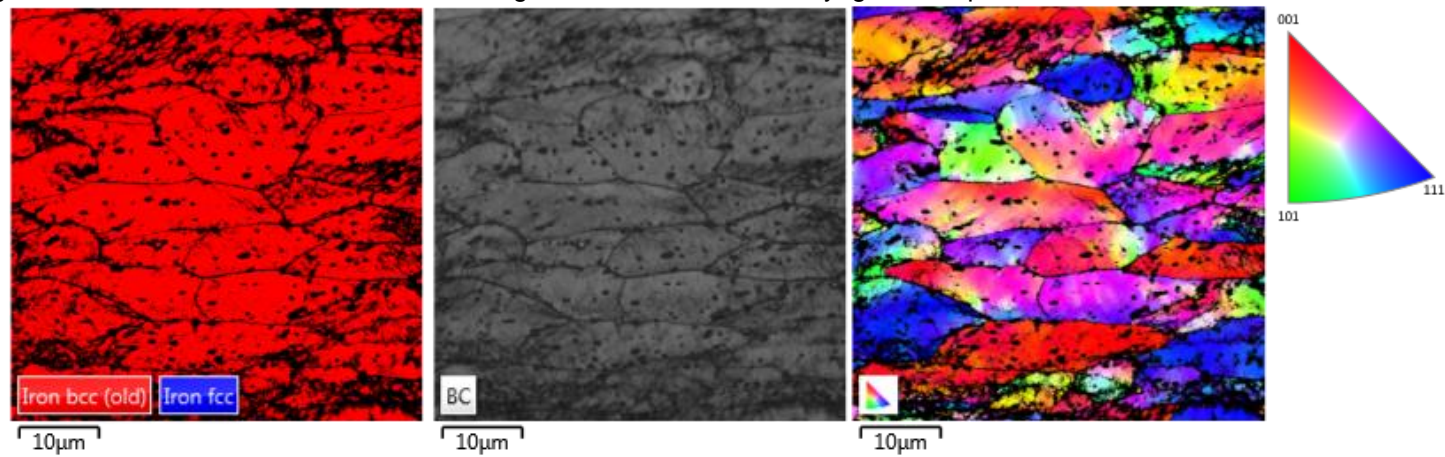
Source: The author.

5.4 FRACTOGRAPHY ANALYSIS

5.4.1 AISI 304

Based on images obtained by secondary electron signals in a high-resolution microscope, SEM-FEG, as shown in Figures 47 and 48. In the figures, it can be seen, in both conditions, faceted fracture surface. It can be also visually perceived that the fracture surface area is smaller at room temperature (RT) when compared to the answer cryogenic temperature (CT), showing a reduction in area bigger.

Figure 47 - Fracture surface micrograph of AISI 304 steel, tested at room temperature in 2.8×10^{-4} s^{-1}.
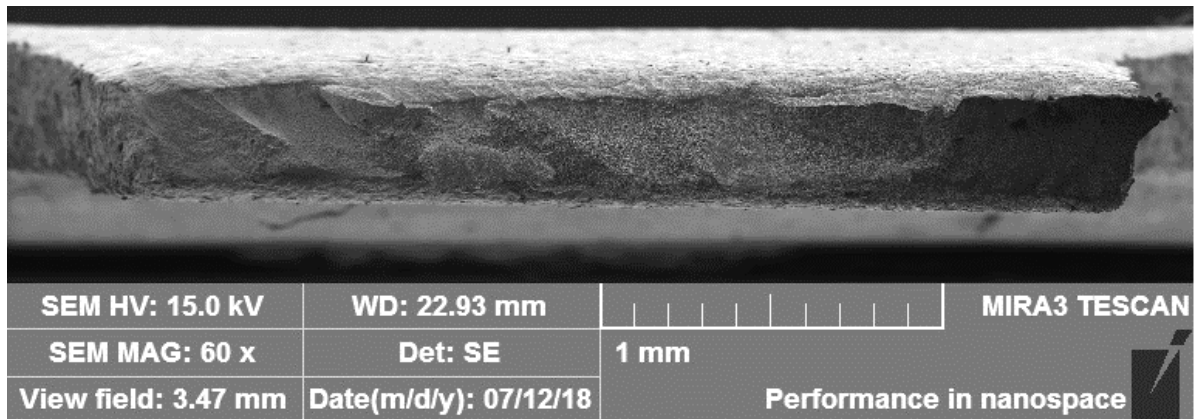
Source: The author.

Figure 48 - Fracture surface micrograph of AISI 304 steel sample, tested at cryogenic temperature in 2.8×10^{-4} s^{-1}.
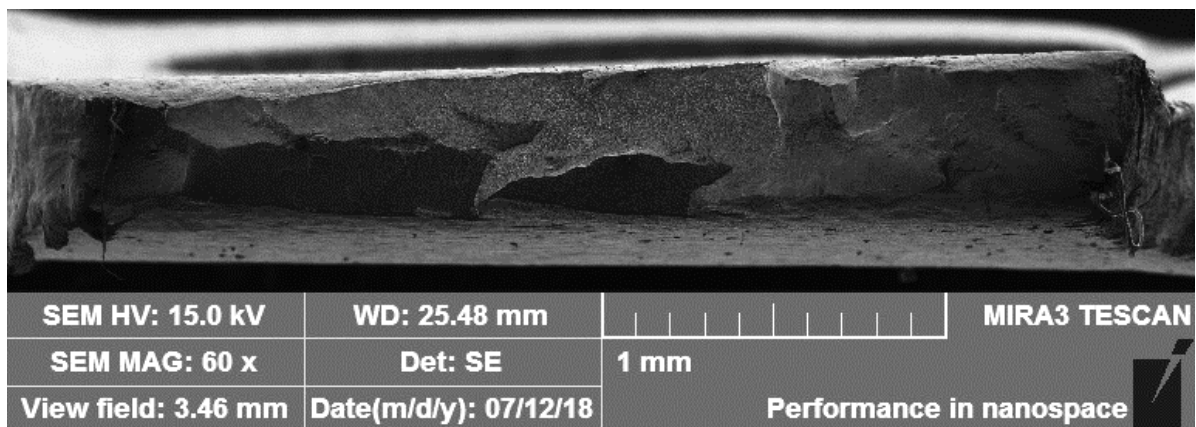
Source: The author.

In both temperatures, the fracture surface was fully composed with the presence of dimples, ductile fracture characteristic. The mechanism of ductile fracture involves nucleation of voids, growth and their coalescence. During plastic

deformation occurs void formation either by cracking of the second-phase particles or by decohesion of second-phase particles from the matrix [16,111,126-130]. In the samples submitted to the CT tests, dimples are subtly smaller and less deep, which indicates a lower ductility at this temperature. Those differences can be seen on the fracture surface, Figure 49.

Figure 49 - AISI 430 steel fractography at (a) room and (b) cryogenic temperature (Both 2.8×10^{-4} s^{-1}).
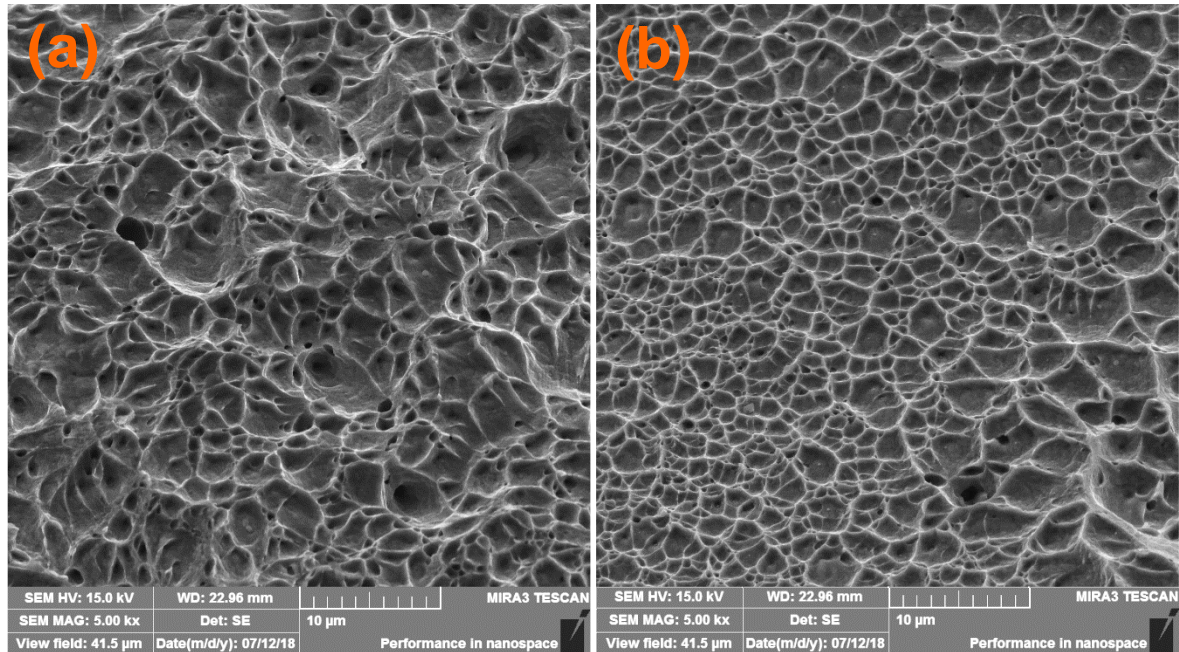
Source: The author.

In both temperatures, there are differences in voids size. For ductile materials, there are many published literature correlating fracture mode with deformation properties. Dimples with a smaller size at cryogenic temperatures occur due to the bigger potential to dimples nucleation, resulting in a lower available free path for expansion of the generated microcavities [74, 77]. However, when it comes to austenitic stainless steel, we should remember that there is phase transformation. In this case, the interfaces between austenite and martensite formed during tensile tests become principal nucleation sites for secondary void formation. Das and Tarafder found that microvoid formation resulted from the separation of adjacent islands and localised deformation of martensite, and decohesion at the austenite-martensite interface [111].

With this, it can be assumed that any fractograph morphology variation of the samples tested is due to the amount of stress-induced martensite. Thus, at CT

occurred a greater number of nucleation void than at RT, pointing a bigger amount of austenite-martensite interfaces available.

The fracture area values were obtained by Image J® software, and by Equation 11 values of reduction in area were calculated, results are shown in Table 15 and Figure 50.

Table 15 - Values of reduction in area % for AISI 304.

	1.3×10^{-3} s^{-1}	5.0×10^{-4} s^{-1}	2.8×10^{-4} s^{-1}	6.6×10^{-4} s^{-1}
RT	70.9%	61.8%	65.9%	63.48%
CT	56.9%	49.1%	50.5%	49.7%

Source: The author.

Comparing to both temperatures response, it could be observed, in RT tests, that there was a more significant reduction in area than at CT. As a result, the average reduction in area for RT was 65.5%, and for CT was 51.5%. Resulting in a 27% increase in reduction in area when comparing RT to CT. This result shows that deformed material at RT has higher ductility than deformed material at CT.

Figure 50 - Values of reduction in area for AISI 304.
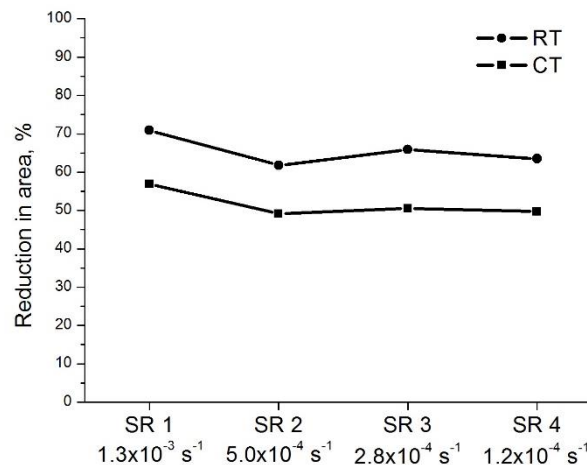
Source: The author.

Reduction in area results, when analysed only a temperature (ambient or cryogenic), it can be noted that there is a more significant reduction in area for the faster strain rate (1.3×10^{-3} s^{-1}), and a smaller decrease in area in other strain rates, the results being very close, however non-linear. Strain rates values are very close, then, the difference between strain rates, especially for three lower strain rates, can be associated with the error value.

In summary, tests at RT exhibit more ductility in the reduction in area result, and in appearance fracture surface, which has fewer dimples density and presents larger dimples size, than tests at CT. About strain rates, by the values it cannot be observed a definite relation.

5.4.2 AISI 430

The images obtained by secondary electrons signals in the high-resolution microscope, SEM-FEG, at 2.8×10^{-4} s^{-1} strain rate, are presented in Figures 51 and 52. Notably, the fracture surface area of the sample at RT is smaller than at CT, which indicates a more ductile fracture in RT. In addition to the fracture area, the higher ductility in RT can be seen in the fracture aspect, and CT has a flatter surface than RT, characteristic of brittle fracture.

Figure 51 - Fracture surface micrograph of AISI 430 steel sample, tested at room temperature in 2.8×10^{-4} s^{-1}.
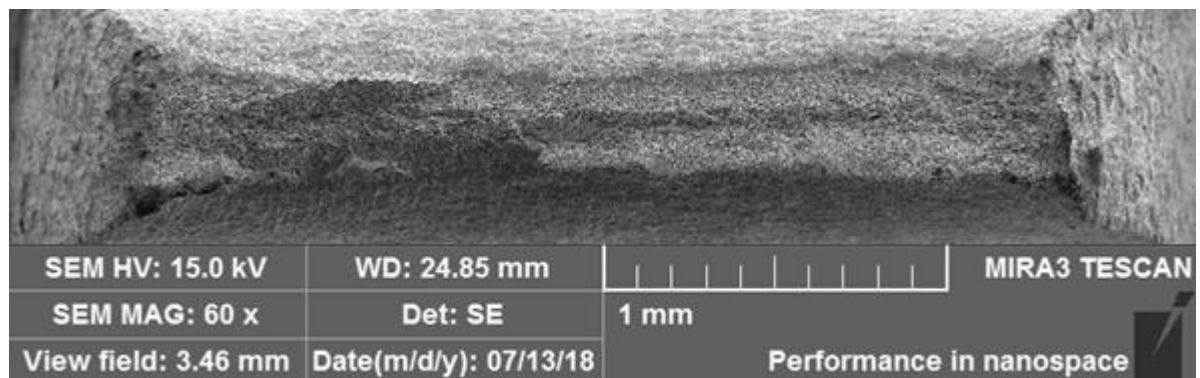
Source: The author.

Figure 52 - Fracture surface micrograph of AISI 430 steel sample, tested at cryogenic temperature in 2.8×10^{-4} s^{-1}.
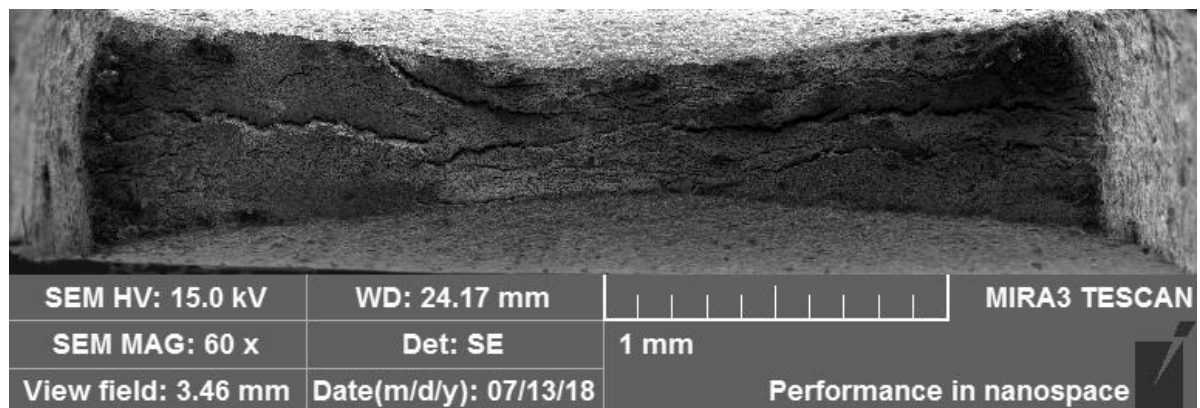
Source: The author.

An additional test was made to improve the ductile-brittle transition understanding, with 6.6×10^{-3} s^{-1}, its fractography is showed in Figure 53. With this strain rate faster than the others, a surface more fragile was obtained at cryogenic temperature, presenting a greater fracture surface area, with small necking.

Figure 53 - Fracture surface micrograph of AISI 430 steel sample, tested at cryogenic temperature in 6.6×10^{-2} s^{-1}.
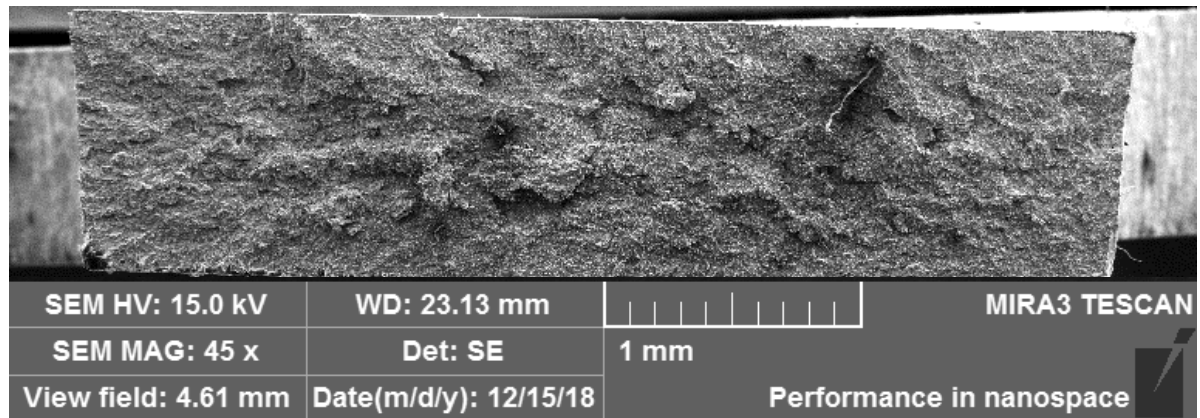
Source: The author.

Figure 54 shows the three fractures with a greater magnification. At (a) it can be seen a pure ductile fracture. In the fractography (a) and (b), it can be seen that some bands were formed by void coalescence along the fracture surface, being more evident in (b), when a large group or micro-cracks were formed. Aspects of brittle fracture are present, like cracks, river patterns, and transgranular brittle cleavage in the CT sample fracture surface, as seen in (c).

Figure 54 - AISI 430 steel fractography (a) at room, (b) at cryogenic temperature (Both in 2.8×10^{-4} s^{-1}) and (c) 6.6×10^{-3} s^{-1} at cryogenic temperature.
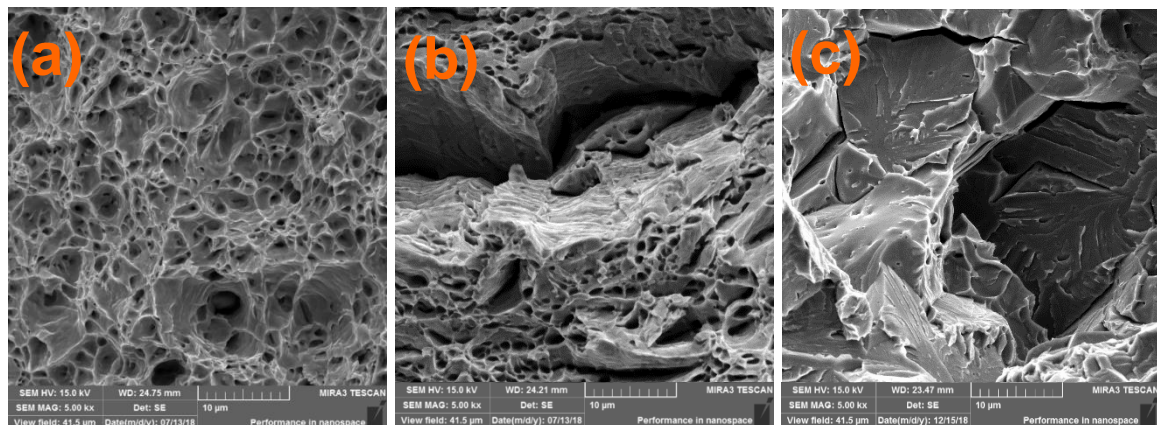
Source: The author.

AISI 430 results for reduction in area, in all conditions, are shown in Figure 55. At RT there is a slight variation of reduction in area between the strain rates, having a slight increase in percentage when strain rate decreases, but the values of the two slowest rates are very close. At CT results, comparing only the four strain rates used initially, it seems that the more quickly strain rate, 1.3×10^{-3} s^{-1}, showed more difference when compared with other strain rates, having it a smaller reduction in area result. The other three strain rates have a subtle %RA increase when decreasing strain rate. The %RA average was 80.8% at RT and 64.8% at CT with the same strain rates, thus, there was an increase of RT reduction in area of 20% approximately.

Figure 55 - Values of reduction in area for AISI 430.
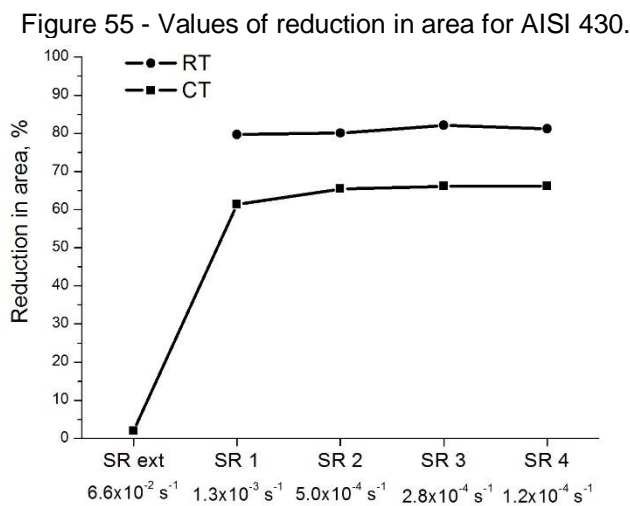
Source: The author.

Utilising the new strain rate result, tested in UEPG laboratory, it could be noted a difference between the strain rates used before. With the new strain rate, the reduction in area was 2%, and the average reduction in area of other strain rates at CT was 65%. Table 16 exhibits all reduction in area values.

Table 16 - Values of reduction in area % for AISI 430.

	6.6×10^{-2} s^{-1}	1.3×10^{-3} s^{-1}	5.0×10^{-4} s^{-1}	2.8×10^{-4} s^{-1}	6.6×10^{-4} s^{-1}
RT	-	79.7%	80.1%	82.1%	81.2%
CT	2.0%	61.4%	65.4%	66.1%	66.2%

Source: The author.

At room temperature, the fracture occurred with the ductile mechanism of nucleation, growth, and coalescence of voids, but temperature decrease induces the

ductile-brittle transition (DBT). The ductile mechanism and cleavage compete with each other in the ductile-brittle transition, and the phenomenon could be observed in fracture surface analyse, as seen in Figure 56. Both samples were deformed at cryogenic temperature, strain rates (a) 1.3×10^{-3} s^{-1} and (b) 6.6×10^{-2} s^{-1}. In the letter (a) there are dimples, ductile fracture characteristics, simultaneously with river patterns, that is brittle fracture characteristic.

Figure 56 - AISI 430 fractography, with strain rate (a) 1.3×10^{-3} s^{-1} and (b) 6.6×10^{-2} s^{-1} at cryogenic temperature.
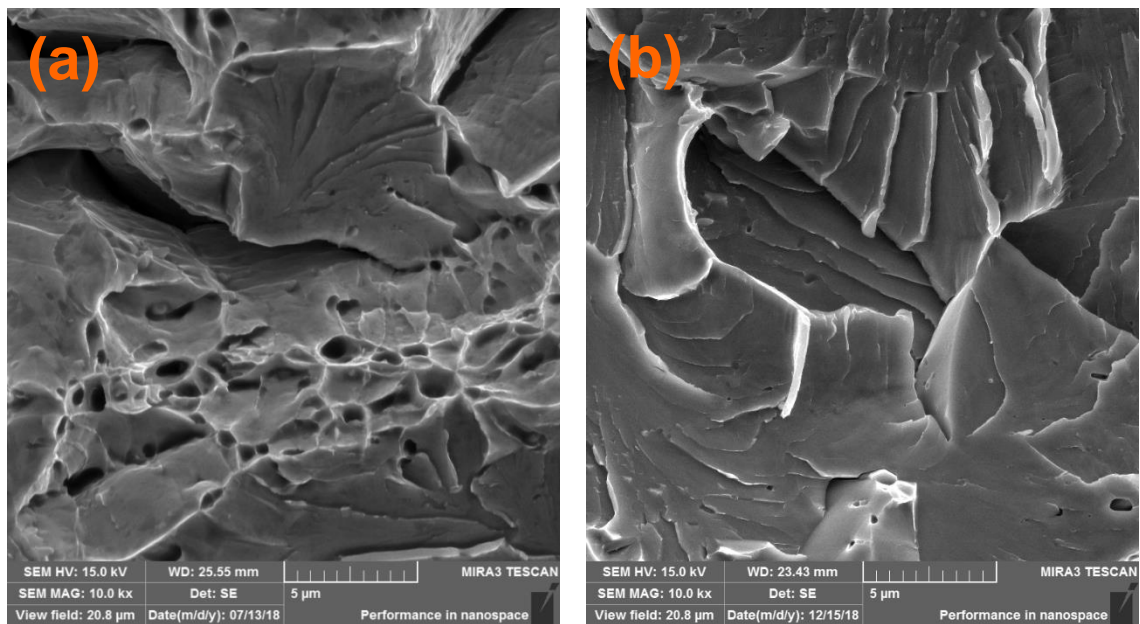
Source: The author.

Using fractography it was possible to observe fracture mode change according to the strain rate at CT; the faster strain rates show a more significant presence of brittle fracture characteristics, as shown in Figure 57. At the slower strain rate, 1.2×10^{-4} s^{-1} Figure 57 (a), river patterns can be found but they were rare. Increasing strain rate to 2.8×10^{-4} s^{-1}, Figure 57 (b), there is a higher amount of river patterns. However, there are still few. Comparing these two strain rates, there is not much difference in how they look, only in the higher quantities of river patterns in 2.8×10^{-4} s^{-1}. Now, when the strain rate increases to 5.0×10^{-4} s^{-1}, Figure 57 (c), the presence of river patterns is relevant, but regions with only a brittle characteristics were not seen. In 1.3×10^{-3} s^{-1} it can be seen areas with this aspect, Figure 57 (d), this condition exhibits regions without dimples. Besides, with the additional strain rate (6.6×10^{-2} s^{-1}), Figure 57 (e), only brittle fracture characteristic is present.

Figure 57 - AISI 430 steel fractography, at cryogenic temperature, with (a) de 1.2×10^{-4} s^{-1}, (b) 2.8×10^{-4} s^{-1}, (c) 5.0×10^{-4} s^{-1}, (d) 1.3×10^{-3} s^{-1} e (e) 6.6×10^{-2} s^{-1} strain rate.
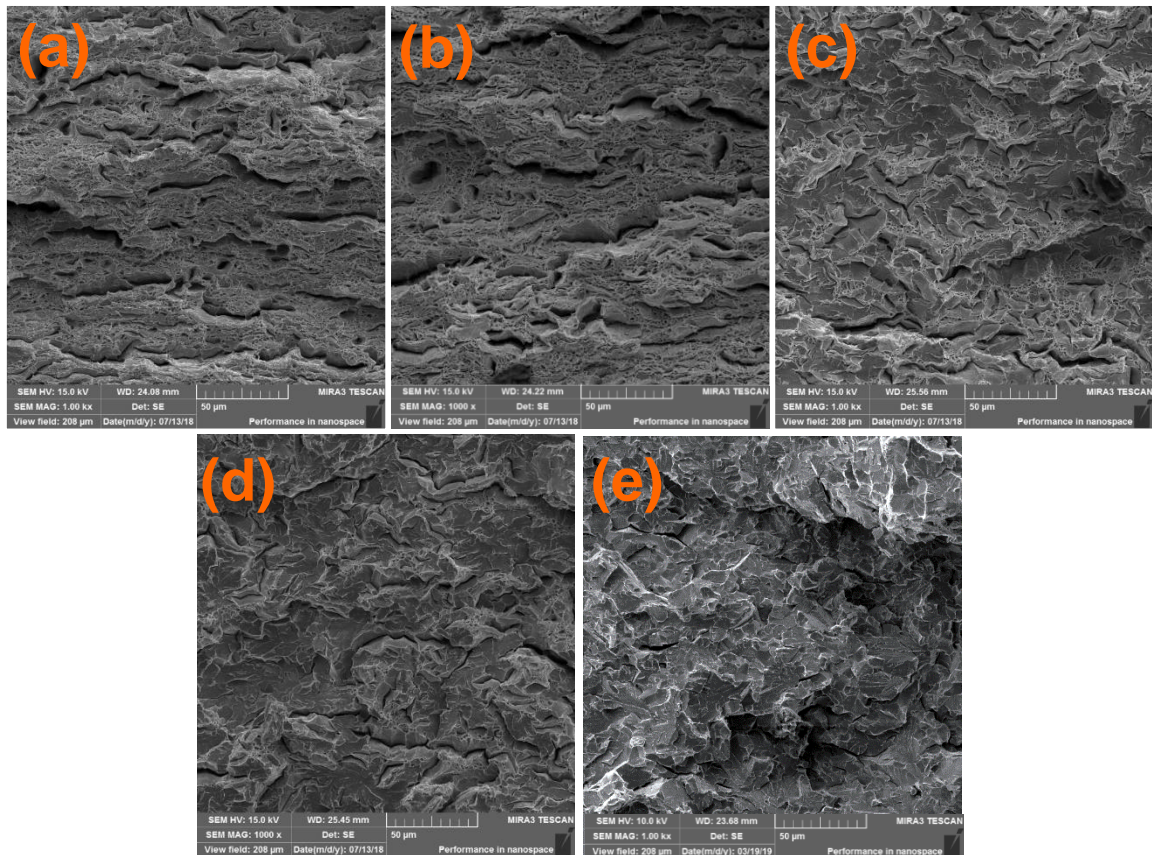
Source: The author.

The faster strain rate was able to reach to brittle fracture. These events indicate that all strain rates used in CT were close to the ductile-fragile transition point. Both ductile and brittle mechanisms will be competing during deformation, and both mechanisms can be active at the same time, the intensity of each will differentiate the dominant mechanism. Both will conduct to an active softening zone. An internal necking of the ligaments between unstick particles will occur in the ductile mechanism, and for cleavage, this is the region where the cohesive zone is in the softening regime of the traction-separation law [122].

Both in RT and CT, the three slower rates were very close, and they did not present significant differences in reduction in area. However, with the fracture surface analysis, it can be noted the difference between these strain rates, being that the faster rates have a more brittle characteristic. Therefore, it can be concluded that strain rates were revealed to have little effect on the YS and UTS, and likely influence in the failure mode. This result also was evident in the research of Xu[118] *et al.*

Another interesting fact is that the fracture tips are regions in which there is the most expressive brittle characteristic and, as it approaches the middle of the sample, the dimples presence is increased, until in the central area where only dimples are observed. This shape is best seen in the sample with the strain rate $1.3x10^{-3}$ s^{-1}, as shown in Figure 58.

Figure 58 - Fracture aspect transition along the length. Cryogenic temperature sample in $1.3x10^{-3}$ s^{-1}.
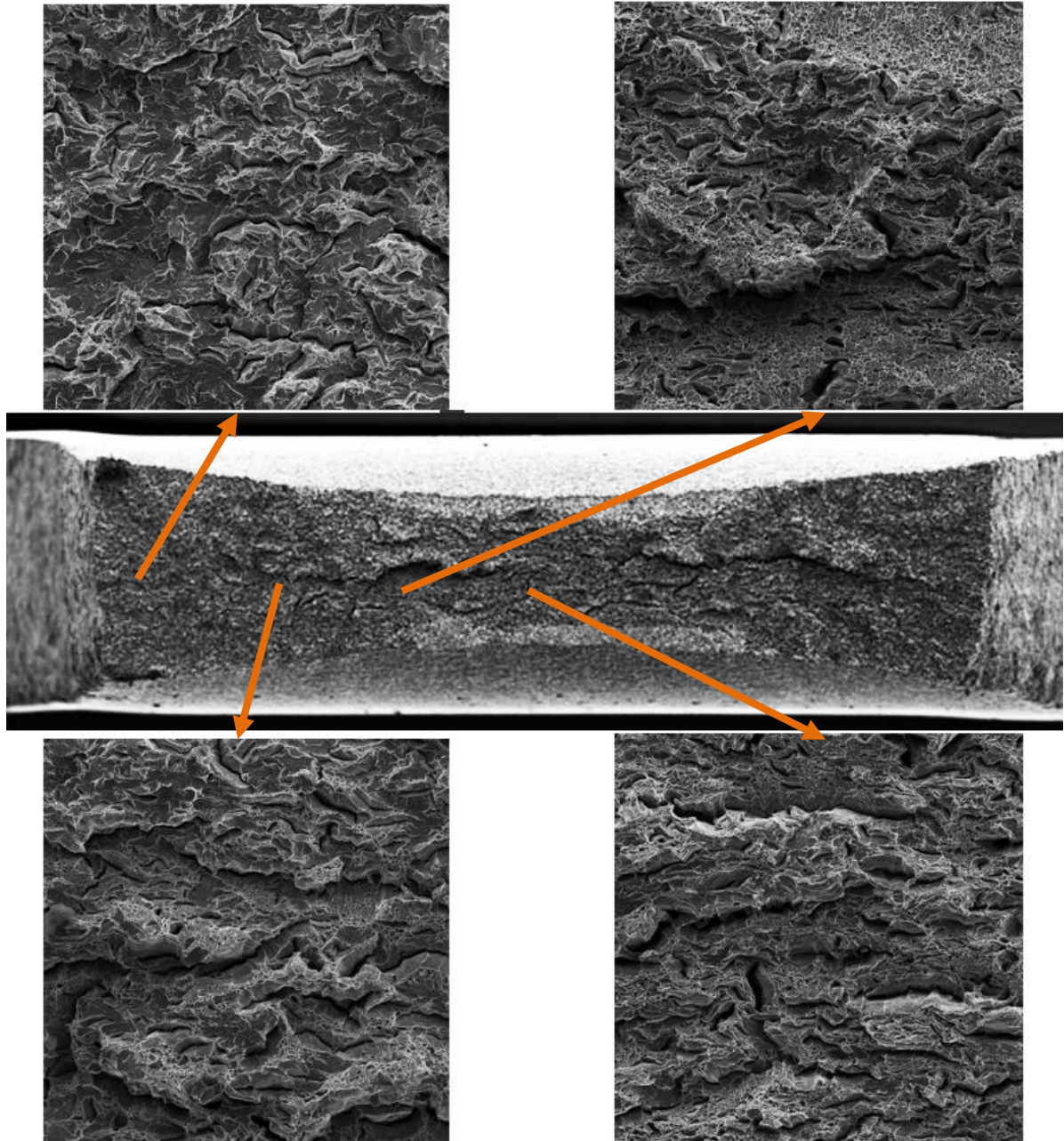
Source: The author.

From the border distance to the totality of dimples is more considerable for the deformation rate of 1.3×10^{-3} s^{-1}, and decreasing strain rate there is a distance reduction. This feature is another striking difference between fractography at rates 1.3×10^{-3} s^{-1} and 5.0×10^{-4} s^{-1}. It remembers that 6.6×10^{-2} s^{-1} at CT presents only brittle fracture characteristic.

Everything that interferes transition, as grain size, carbide particle, the cohesive strength of the matrix, and SFE are necessary for understanding the ductile-brittle transition. There are some manners to crack initiation and propagation, and it depends on the cohesive strength matrix, the carbide strength, and the carbide-ferrite interaction. Hütter[131] and Giang[122] showed the initial crack propagation for weak particles, with cohesive strength of particle-ferrite interface $\sigma_{cPM}/\sigma_0 = 1$, in three different values of the matrix strength ratio, which corresponds to different temperatures. Purely ductile crack propagation is, characterised by void nucleation from debonded carbide particles and subsequent void growth. At low strength ratio (ferritic matrix x yield stress), generally at low temperatures when the yield stress increases, the carbide particles break first before cleavage occurs in the matrix. Plastic deformations are not observed, but the matrix remains completely elastic. In the intermediate DBT region, ductile and brittle failure co-occurs. In the beginning crack, voids have grown, a stretch zone has been formed at the crack tip, and then, the matrix finally fails by cleavage. Figure 59, the first carbide particles debond from the matrix, whereas those in a certain distance to the initial crack tip broken [122,131].

Figure 59 - Crack initiation and propagation with weak particles in ductile-brittle transition region.
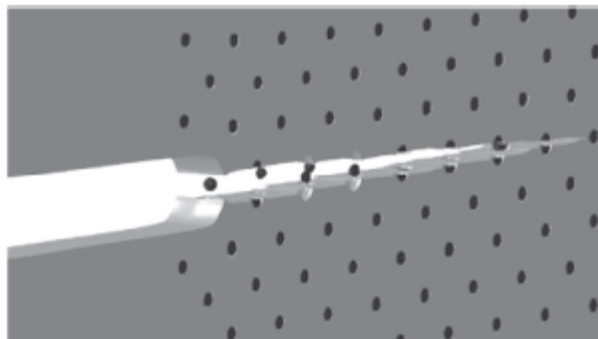
Source: Giang *et al.*, (2017)[122].

With these statements, it can be concluded that the condition shown in Figure 58 was in DBT0 region and that, in the sample's middle started the crack. In this

region is where there is a higher concentration of tensions because this region is localised in the maximum strain axis, where there is the stress triaxiality more pronounced [122,126,127,129]. After the crack beginning, a stretch zone has been formed at the crack tip, and the cleavage begins to occur. Because of this phenomenon, the sample border has cleavage characteristics.

The fracture shape also shows the DBT effect. Because in the sample centre, where there are more ductile characteristics, the fracture shape looks like a ductile fracture. However, in the sample border, where there are more brittle characteristics, the fracture shape resembles with brittle fracture. Thus, the sample centre has more strain, showing minor thickness, and the sample border has less strain, showing limits with right angles shape.

5.5 X-RAY DIFFRACTION

5.5.1 AISI 304

Together with the tensile test, X-ray diffraction (XRD) measurements were performed using synchrotron radiation. The acquisition time was 3 seconds, which allows an *in situ* evaluation of the phenomena occurrence.

AISI 304 steel samples stress-strain curve tested at a strain rate $5.0 \times 10^{-4} s^{-1}$, at room and cryogenic temperatures, was chosen to exemplify the changes in the profiles during deformation, such as broadening and displacement of the peaks. The strategic points for the diffractograms collected were the same for both temperatures; however, due to different strain response, they are not the same strain values. The points were: test beginning, plastic strain approximately at the beginning and at the middle, ultimate tensile strength and after necking beginning. These profiles are shown in Figure 60, without corrections and adjusts.

Due to peaks number and the intensity variation between them, a better analysis can be done by overlapping the diffraction profiles for each peak. The AISI 304 steel peaks (111), (200) and (220) referring γ-austenite planes, (110) and (200) α'-martensite planes and (101) ε-martensite plane are shown individually in Figure 61.

Figure 60 - AISI 304 steel samples diffractograms tested on the XTMS line, obtained simultaneously to the mechanical test under 5.0×10^{-4} s^{-1} strain rate. (a) Room temperature; (b) Cryogenic temperature.
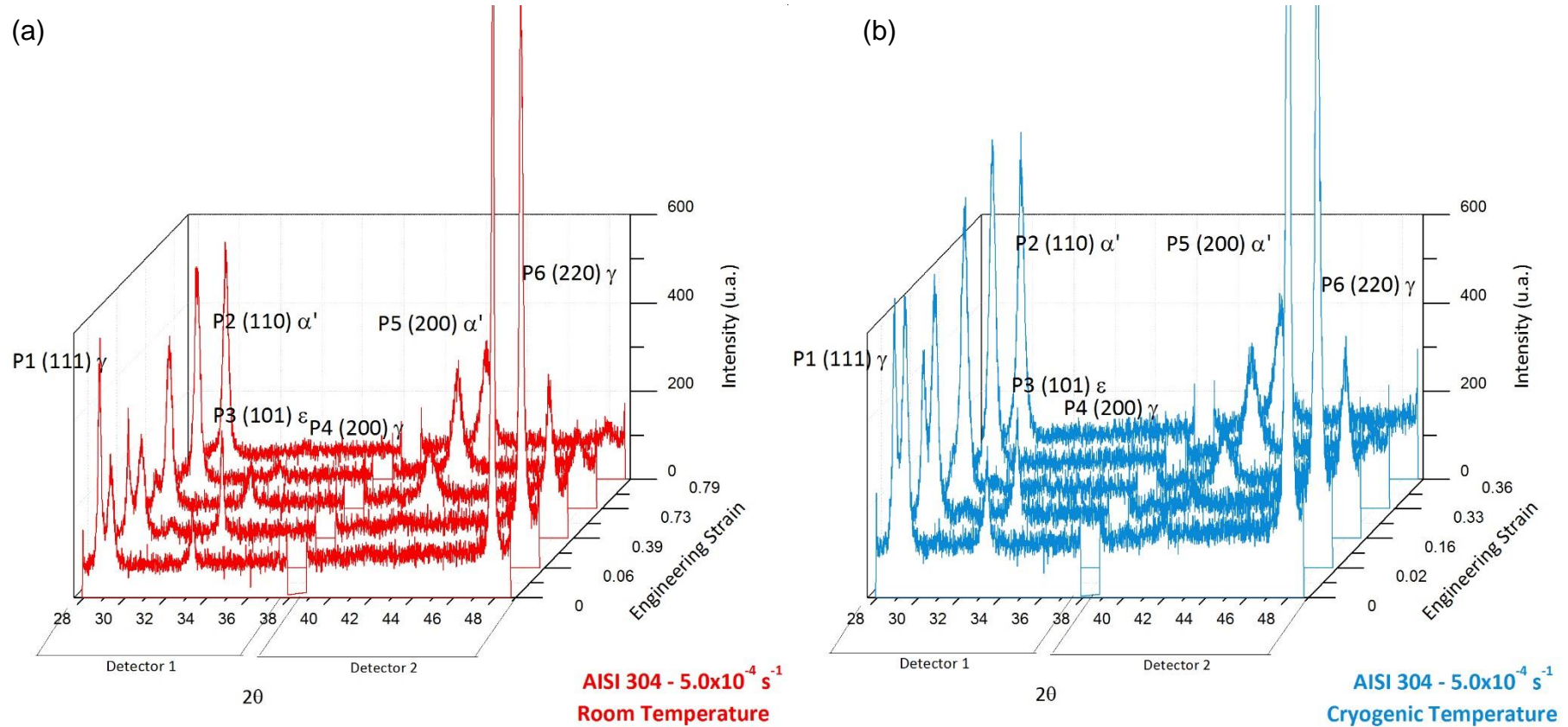
Source: The author.

Figure 61 - Peaks (111), (200) and (220) of austenite planes, (110) and (200) α'-martensite planes and (101) ε-martensite plane of the AISI 304 steel, under strain rate of 5.0×10^{-4} s^{-1}, at room and cryogenic temperatures.
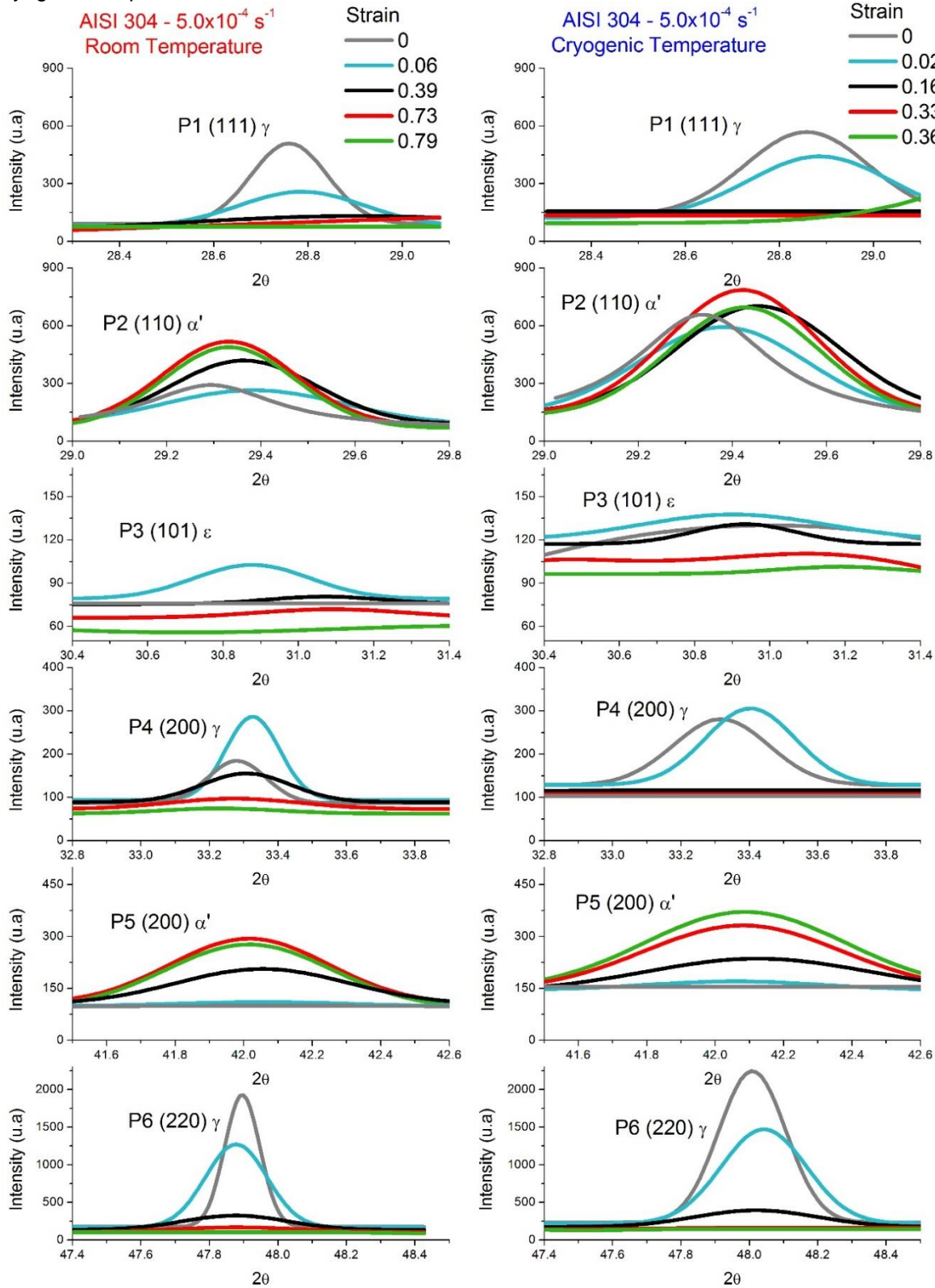
Source: The author.

The peaks were adjusted using a Gaussian function, just as all X-ray diffraction profiles were adjusted for the other analysis. As the same scales of graphs were used for each peak at room and cryogenic temperatures, one can see and compare the position and width variation of the peaks. For peak (111) of austenite plane, P1, it is perceived that the initial peak width, without strain, is higher at CT than at RT. As deformation progresses, there is an intensity reduction and width broadening of peaks in both cases. At the two temperatures, in about half plastic strain, there is no longer the presence of this peak.

At cryogenic temperature, the peak (110) of α'-martensite plane (P2) presents higher intensity and greater width than this peak at room temperature. The area under curves increases, in both cases, up to the ultimate tensile strength, and after necking beginning there is area reduction.

Both at room and cryogenic temperatures, during deformation the (101) ε-martensite peak (P3) appeared, such as shown in Figure 61. Analysing peak presence in all strain rates, in both temperatures, only the fastest rate at room temperature did not reveal the peak presence. However, this may be related to a small number of acquisitions due to test time (quickly strain rate), which was not slow enough to capture peak arising. For all other strain rates, the peak appears at the beginning of plastic strain, and near the middle of plastic strain it becomes to be not so evident. Several researchers found where α'-martensite formation initially occurs, and the searches pointed to shear bands, staking faults, twins and ε-martensite [17,19,98,132]. In this study, how there is the ε-martensite presence, probably α'-martensite can have their embryos formed in these places. However, it can make it possible to observe α'-martensite formation together with ε-martensite occurrence, showing that α'-martensite embryos formation can occur also in another sites. Volume fraction of ε-martensite was not calculated because there is only a peak for analysis, and the peak presents low intensity.

Areas under peaks (200) for austenite plane for initial diffractograms and approximately at the plastic strain beginning are more significant for the sample tested at CT. In both temperatures, there is an area increase from the initial point to plastic strain beginning, in ultimate tensile strength point, the peak still exists only at RT, at CT it is no longer present.

The peak (200) of α'-martensite plane is not initially present, in both temperatures, and as the strain occurs, there is an increase in its area, progressively.

In a manner contrary to that (200) α'-martensite plane, the peak (220) of austenite plane presents beginning with high intensity, and as the strain occurs, there is a decrease in its area, progressively. Close to ultimate tensile strength, the peak present loses intensity significantly.

With this analysis, it can be observed that plane peaks related to the austenite phase reduce as strain increases in both temperatures, and plane peaks related to the α'-martensite phase increase as strain increases. Thus, it is proving that the martensite transformation occurs during deformation of AISI 304 austenitic stainless steel. It was also possible to observe the ε-martensite phase presence, which becomes evident after strain beginning and disappears during plastic strain.

5.5.1.1 *Martensitic transformation*

X-ray diffraction results turned it possible to obtain volume fraction variation of phases, austenite and α'-martensite, present in AISI 304 steel. The Matsumura equation was used to describe the phase transformation curves [101]. Thus, Table 17 shows the k and q constant values calculated for each sample, using the true and engineering strain values [21,101].

Table 17 - Constants k and q at various strain rates, at room and cryogenic temperatures, in the AISI 304 steel.

		True Strain		Engineering Strain	
		q	k	q	k
Room Temperature	1.3×10^{-3} s^{-1}	3.67	213.7	3.13	57.2
	5.0×10^{-4} s^{-1}	2.15	30.9	1.93	15.6
	2.8×10^{-4} s^{-1}	2.66	47.3	2.27	17.1
	6.6×10^{-4} s^{-1}	1.65	16.5	1.52	10.1
Cryogenic Temperature	1.3×10^{-3} s^{-1}	1.72	69.1	1.59	43.4
	5.0×10^{-4} s^{-1}	1.34	34.6	1.44	47.8
	2.8×10^{-4} s^{-1}	1.34	26.1	1.26	19.0
	6.6×10^{-4} s^{-1}	2.18	335.6	2.06	217.4

Source: The author.

Figure 62 - Volume fraction of austenite and martensite in AISI 304 steel tested at room and cryogenic temperatures, in four strain rates.
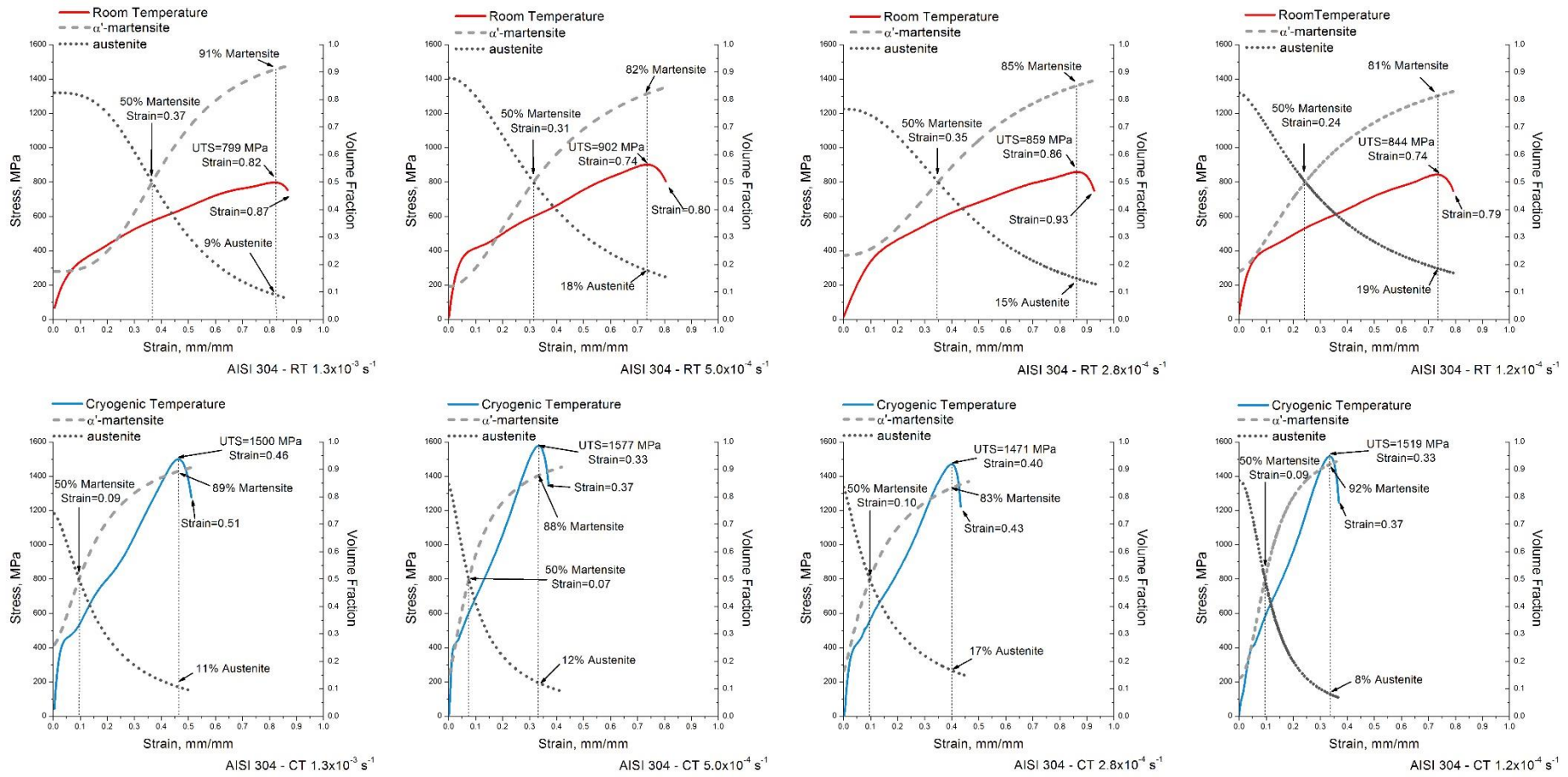
Martensitic transformation dynamic graphs of austenitic stainless steel are presented in Figure 62, at room and cryogenic temperatures and in four strain rates used. By analysing phase transformation kinetics, initially focusing on temperature variation, a formation advance 50% α'-martensite is observed when the material was tested at cryogenic temperature. Figure 63 was plotted for better comparison in 50% α'-martensite transformation strain values. Strain values at room temperature are around 0.3 mm/mm, and for cryogenic temperature, the martensitic transformation occurs approximately at strain of 0.1 mm/mm, showed considerable anticipation at CT. At higher temperature, there is suppression of strain-induced martensite formation, being that rising temperature leads to austenite stability increase. As previously observed, the hardening rate was affected by temperature, rising temperature decreases the second hardening effect, due to an SFE increase (resulting in more stability austenite) and a chemical driving force $\Delta G\gamma \rightarrow \alpha$' reduction [11,17,21,110-113].

Figure 63 - Strain values for 50% martensitic transformation, in all strain rates, at room and cryogenic temperatures.
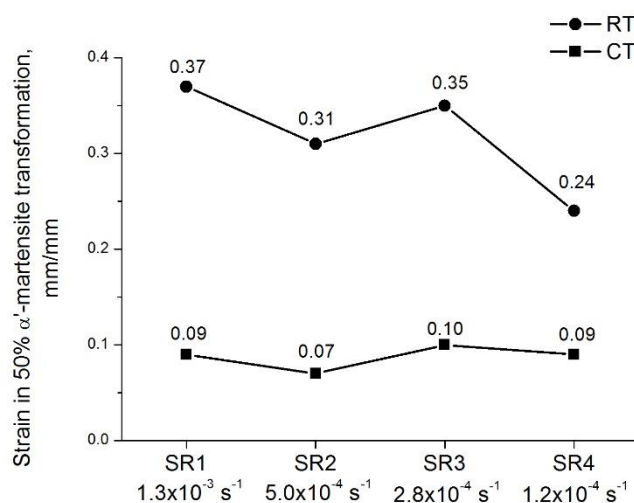
Source: The author.

When comparing martensitic transformation by observing the influence of strain rate at room temperature, a delay in the formation of 50% martensite is seen when the strain rate is increased. Wherein the strain rate 5.0×10^{-4} s^{-1}(SR2) runs away comportment; however, values are near. Of course, the behaviour becomes evident when comparing two extreme strain rates. At room temperature, martensitic

transformation delay occurs due to higher adiabatic heating generated at high strain rates [17,94,110].

Now, when comparing martensitic transformation, at cryogenic temperature, by observing strain rate influence, significant changes were not found. For all strain rates, strain values on 50% martensitic transformation point are around 0.09 mm/mm. At cryogenic temperatures, how α'-martensite transformation occurs in the very beginning of deformation, the strain rate influence cannot be observed.

In order to improve the understanding of martensitic transformation, transformation rates analysis were made at room and cryogenic temperatures, as shown in Figure 64.

Figure 64 - Volume fraction of stress-induced martensite (a) and rate of stress-induced martensitic transformation (b) as function of true strain at room and cryogenic temperatures in AISI 304 steel. Both 5.0×10^{-4} s^{-1} strain rate.
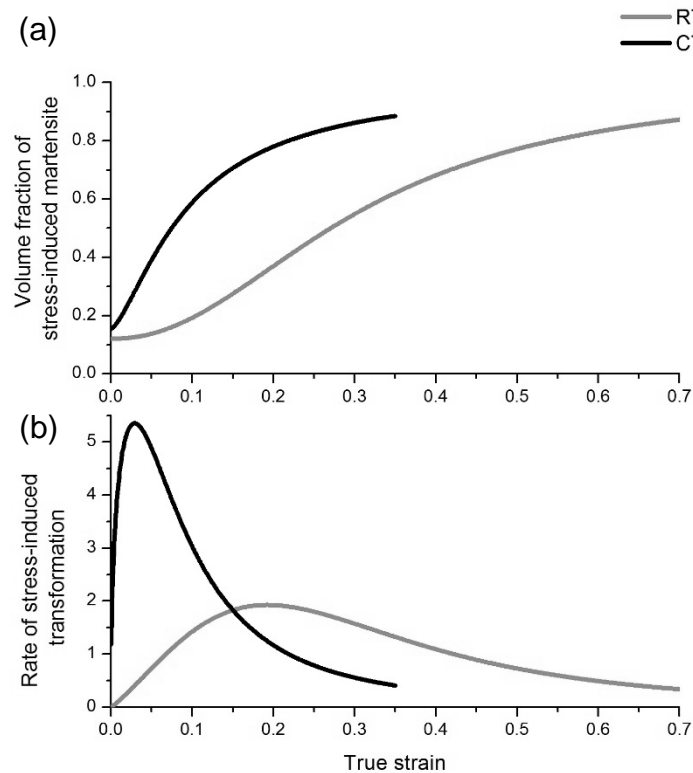
Source: The author.

Martensitic transformation rate (MTR), in both cases, after the start strain, increased to the maximum and decreased after the maximum value. Therefore, MTR at CT increased quickly right at the beginning strain, and there is an advancing to reach maximum MTR value observed when compared with RT. While at RT, the maximum point occurs at larger strain, and there is a lower maximum MTR value.

Looking for α'-martensite volume fraction graph, it can be noted that the final phase values are close, but at CT, the maximum volume fraction occurs before, indicating what the transformation rate already exhibited.

Figure 65 shows the martensite volume fraction (MVF) at the points: the beginning of tests and ultimate tensile strength. The UTS values were chosen due to diffractograms after necking not to show well-delineated peaks. In general, comparing both temperatures, all MVF are close, at both initial and UTS values. The difference between these conditions can be seen, but it is small. However, the initial values of MVF are more prominent than expected, thereby a new analyse using a conventional diffractometer was made to understand the high values of martensite initial (Figure 66).

Figure 65 - Martensite volume fraction (MVF) in the beginning of tests and ultimate tensile strength. At room and cryogenic temperatures and all strain rates.
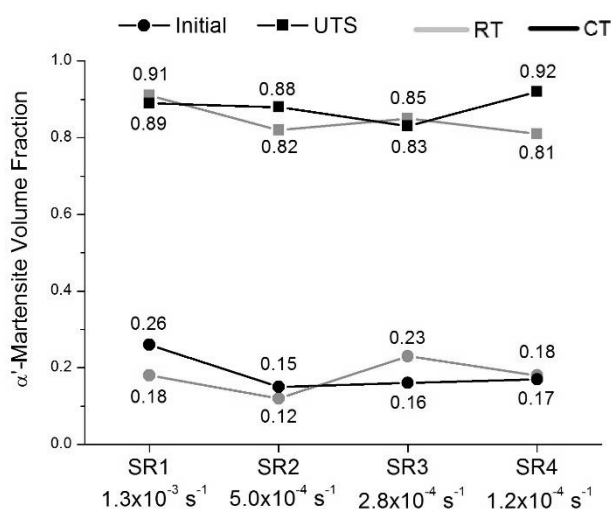
Source: The author.

With these new diffractograms, XRD's results from samples prepared as used in the XTMS and electrolytically polished samples, it can be observed that electropolishing was enough to remove the martensite initial. The 20% MVF initial, approximately, can be due to mechanical stress caused by grinding for metallographic preparation; or heat treatment wasn't enough to remove all martensite caused by skin-pass in the processing. In the second possibility, the electropolishing can have been enough for removing the layer deformed by skin-pass. The high MVF observed in EBSD analysis cannot be taken into account because a little area was used to analyse and did not represent all material.

Figure 66 - X-ray diffraction data using a conventional diffractometer, in samples as used in XTMS (black line), and grinded and polished (red line).
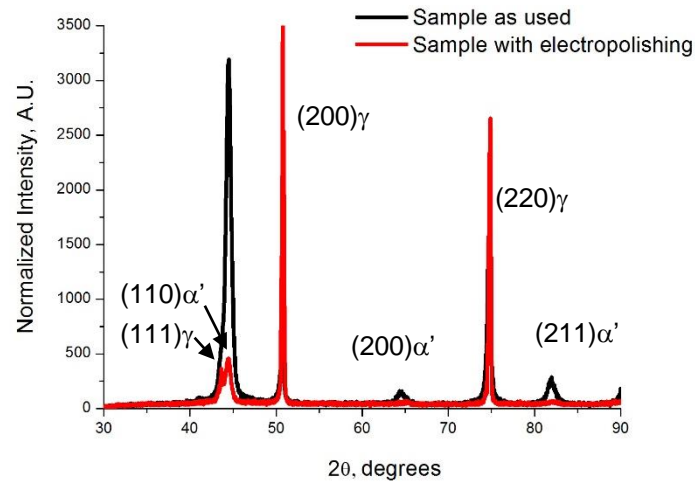
Source: The author.

Figure 67 - Volume fraction of stress-induced martensite (a) and rate of stress-induced martensitic transformation (b) as function of true strain, in all strain rates, at room temperature, in AISI 304 steel.
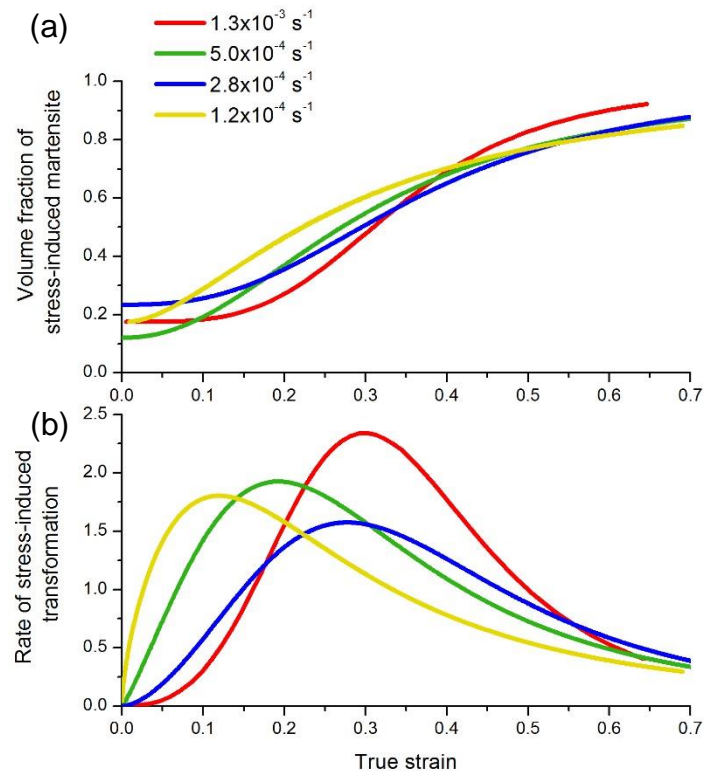
Source: The author.

Now, analysing only room temperature, the martensitic transformation rate (Figure 67) shows that increasing strain rate delays maximum MTR, then it occurs

with greater strain. Another point to analyse is MTR value, which is more significant with increasing strain rate. Only the 2.8×10^{-4} s^{-1} (SR3) strain rate did not show these phenomena, but they occurred because of the initial martensitic volume fraction; these are more different and higher than on other strain rates. Thus, the derivative of the MVF curve for SR3 presents lower area under the curve. The martensitic transformation delay at faster strain rates occurred due to the more significant effect of adiabatic heating with the strain rate increase, leading to larger austenite stability, as already mentioned [94].

Figure 68 - Volume fraction of stress-induced martensite (a) and rate of stress-induced martensitic transformation (b) as function of true strain, in all strain rates, at cryogenic temperature, in AISI 304 steel.
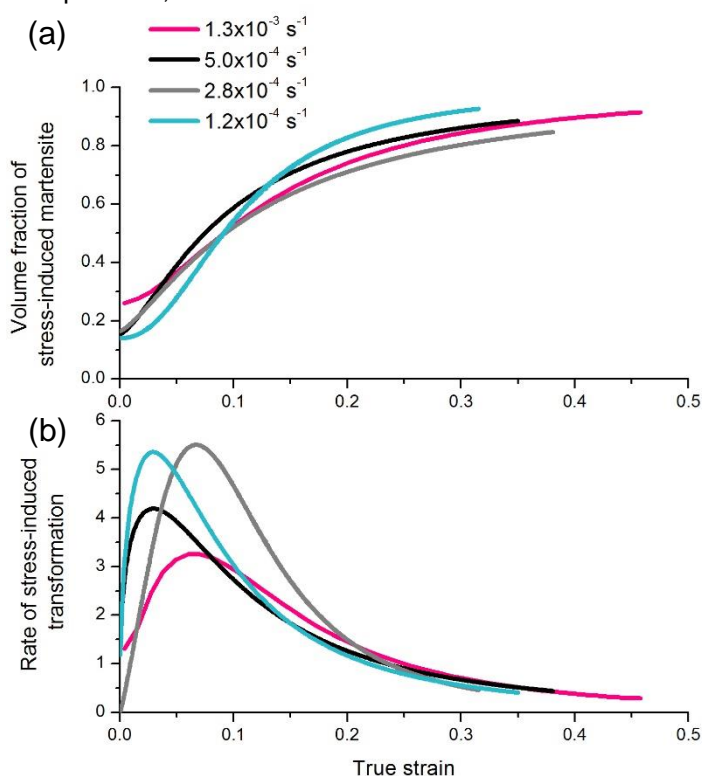
Source: The author.

About cryogenic temperature, the martensitic transformation rate (Figure 68) shows that all strain rates reach maximum MTR early in strain. At CT, the differences between strain values are closer than at RT, so the strain rate impact is small at CT, as mentioned before. The maximum MTR values at CT were lower with increasing strain rate. The thermal effect causes an increase in the stability of austenitic stainless steel and reduces the saturation fraction of martensite [110]. The 1.3×10^{-3} s^{-1} (SR1) strain rate curve showed distance from other strain rates behaviour, but it also

occurred because of the initial martensite volume fraction that is more different and higher than on other strain rates (Figure 65). Thus, by changing the derivative behaviour.

5.5.1.2 *Additional analysis*

At the moment when it was decided to carry out new analysis of X-ray diffraction in conventional diffractometers, to understand the origin of the high value of initial martensite, took advantage of the opportunity and diffraction measurements were carried out also to analyse if there was a preferential orientation on AISI 304 steel. X-ray measurements were taken at 0º direction used in the XTMS and at 90º from that direction. Figure 69 shows the result and appoints that there is no preferential orientation in the austenitic steel studied.

Figure 69 - X-ray diffraction data using a conventional diffractometer, in samples with the same direction at XTMS (black line), and 90º (red line).
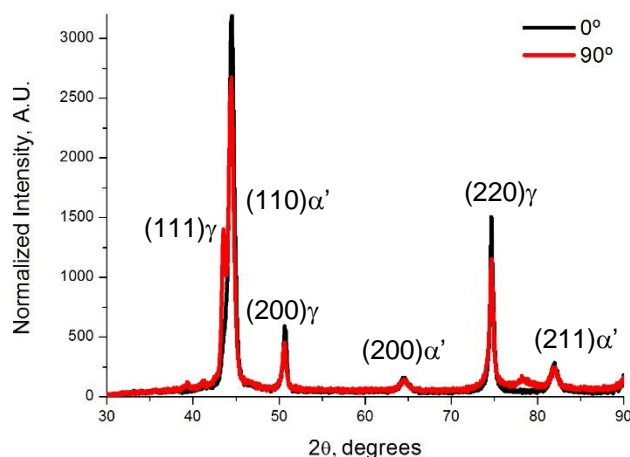
Source: The author.

5.5.1.3 *Microstrain*

Microstrain analysis were performed for each plane present in diffractograms separately. Thus, AISI 304 steel peaks in which the microstrain was analysed refer to (111), (200) and (220) austenite planes and (110) and (200) martensite planes, Figure 70 shows the results. For the ε-phase, the results were not shown here due to the low intensity of (200) peak, which produces a high deviation in results.

Figure 70 - AISI 304 steel microstrain and stress, by engineering strain. At room temperature with strain rate (a) 1.3×10^{-3} s^{-1}; (b) 5.0×10^{-4} s^{-1}; (c) 2.8×10^{-4} s^{-1} and (d) 1.2×10^{-4} s^{-1} And at cryogenic temperature with strain rate (e) 1.3×10^{-3} s^{-1}; (f) 5.0×10^{-4} s^{-1}; (g) 2.8×10^{-4} s^{-1} and (h) 1.2×10^{-4} s^{-1}.
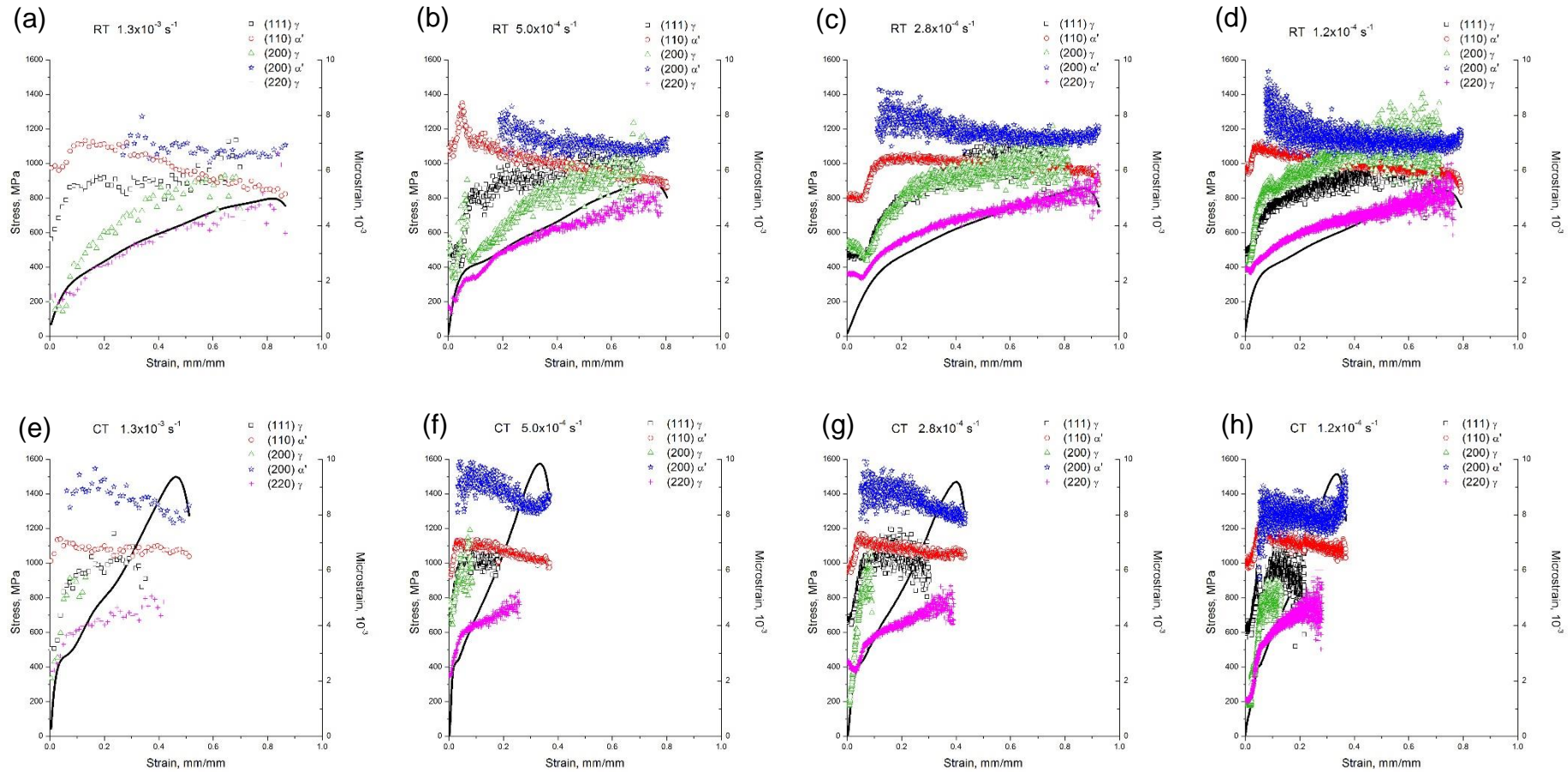
Source: The author.

The microstrain in three planes of austenite phase increased with plastic deformation course in all cases, being that increase in microstrain started after the end of elastic deformation. The austenite planes (111), (200) and (220) tend to disappear before the end of the experiment, because, due to martensitic transformation, the austenite phase is transformed into martensite. At room temperature, the austenite peaks remain until the end, or close to the end, of the experiment. At cryogenic temperature, the austenite peaks disappear sooner than at room temperature; this is because the martensitic transformation happens in advance when decreasing temperature. In general, the austenite peak (200) is the first to disappear, followed by plane (111), and the plane (220) is what remains until the end of the experiments.

The austenite microstrain increases because there is an accumulation of defects in this phase, i. e. concentrate plastic deformation in this phase, initially being responsible for increasing work hardening. With deformation, the microstrain rate of austenite remains constant; however, intensifies driving force for the stress-induced transformation, which increases work hardening. Karimi[133] *et al.* and Hedayati[134] *et al.* established that increase of α'-martensite occurred due to defects density in austenite (more available nucleation sites, as shear band intersections).

The martensite planes (110) and (200) microstrain remains constant, and in some cases, there is a small reduction. The initial values of microstrain of the plane (200) of the martensite phase were disregarded since they presented a high dispersion, then it was not possible to affirm that there was a microstrain increase at the initial deformation. However, for the (110) α'-martensite plane, microstrain increased during the initial yielding and then decreased. It can be assumed that dynamic recovery occurred for α'-martensite phase. It is more probable for dynamic recovery to happen in BCC martensite than in FCC austenite, because higher SFE promote high dislocations mobility, lessening the defects density, resulting in a soonest recovery kinetic [37,59,73].

The α'-martensite constant microstrain was found by Shintani and Murata[135] that showed that the dislocation's density produced by cold rolling at room temperature is mostly stored in austenite phase of AISI 304 steel, because dislocation's density of α'-martensite remained unchanged after cold rolling up to 80% reduction. It is essential to mention that the microstrain values for α'-martensite

planes are more prominent than for austenite planes. Martensite phase α' inherits the austenitic microstrain, and α'-martensite has a higher capacity to store defects than the matrix, then showing high microstrain. This observation was also reported by Hedström[136] *et al*. and Gaus[98] *et al*., in which α'-martensite stores more than twice the stress comparing with autenite in a tensile test of AISI 301 steel.

For better visualisation of the difference between final and initial microstrain obtained for each plane of both phases, a graph with the values was assembled, which is presented in Figure 71. It is seen that there is not a clear tendency in microstrain variation for the planes when the strain rate is varied. Another point observed is that the respective planes to the austenite phase presented more considerable microstrain variation than the planes corresponding to the α'-martensite phase, as previously noted. It can be observed that at CT, the austenite planes reduced the microstrain variation, but the difference is too small, and it can be associated with error due to high final dispersion. With the strain rates used, no behavioural trend can be noted for the microstrain analysis.

Figure 71 - Microstrain variation in (111), (200) and (220) austenite planes, and (110) and (200) α'-martensita planes of AISI 430 steel, at room and cryogenic temperatures, according to strain rate.
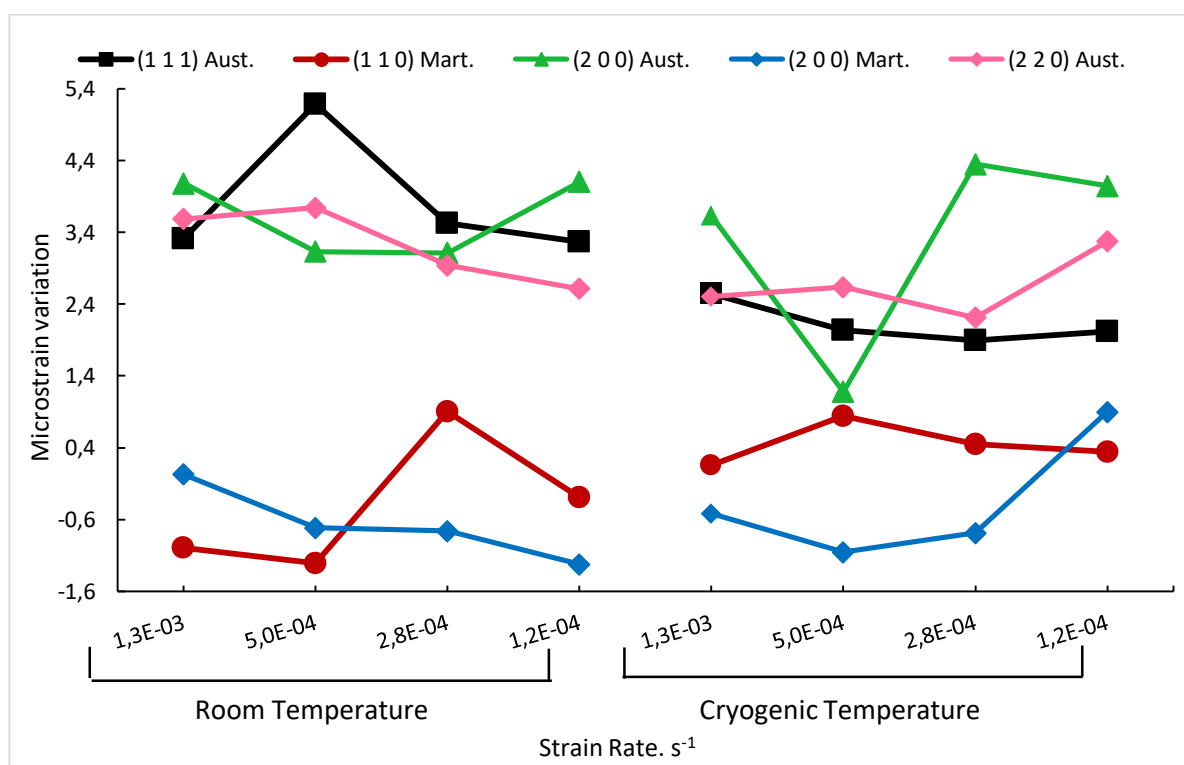
Source: The author.

5.5.1.4 *Crystallite size*

The crystallite size is another parameter measured by X-ray diffraction analysis. The results obtained for AISI 304 at room and cryogenic temperatures at the four different strain rates used are shown in Figure 72. As austenitic steel presents a phase transformation from austenite to martensite, the crystallite size was analysed individually for each phase.

Figure 72 - AISI 304 steel crystallite size and stress, by engineering strain. At room and cryogenic temperatures, with strain rate: (a) 1.3×10^{-3} s^{-1}; (b) 5.0×10^{-4} s^{-1}; (c) 2.8×10^{-4} s^{-1}; (d) 1.2×10^{-4} s^{-1}.
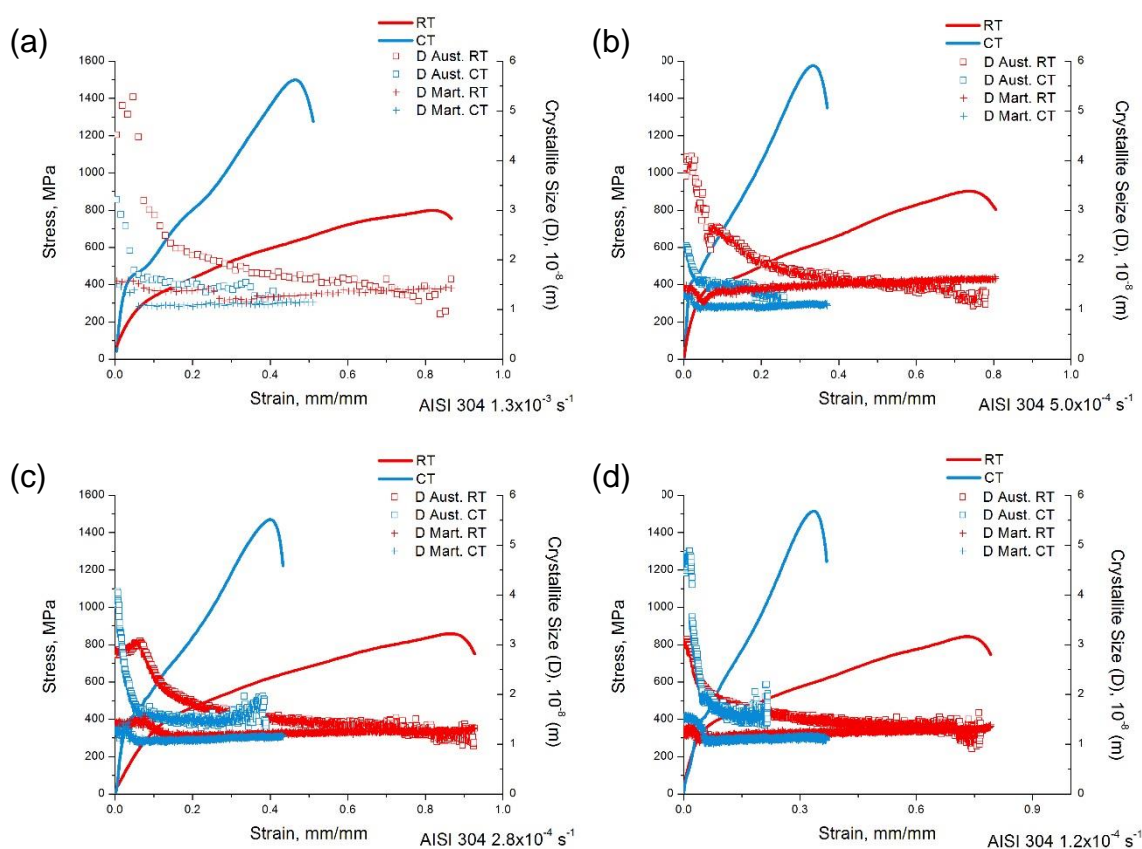
Source: The author.

For austenitic phase, the initial crystallite size is high, and with the deformation, there is a quick reduction in crystallite size. After approximately 0.15 mm/mm strain, the crystallite size reduction rate for the austenite is reduced. For the martensitic phase, in all cases, the crystallite size starts smaller than for the austenitic phase, it has its most significant reduction until approximately 0.15 deformation and then becomes almost constant.

It can be noted that, in both temperatures, the final crystallite size of austenite and martensite are very similar, as showed in Figure 73. The variation between all values is 0.5×10^{-8} m approximately, but it represents almost 50%. Another point noted is the final crystallite size of α'-martensite phase to be a bit bigger than the austenite phase final crystallite size at RT. At CT, the behaviour is reverse, where the value for austenite showed a bit bigger than the martensite value.

Figure 73 - Final values of autenite and α'-martensite crystallite size for AISI 304 steel according to strain rate, at room and cryogenic temperatures.
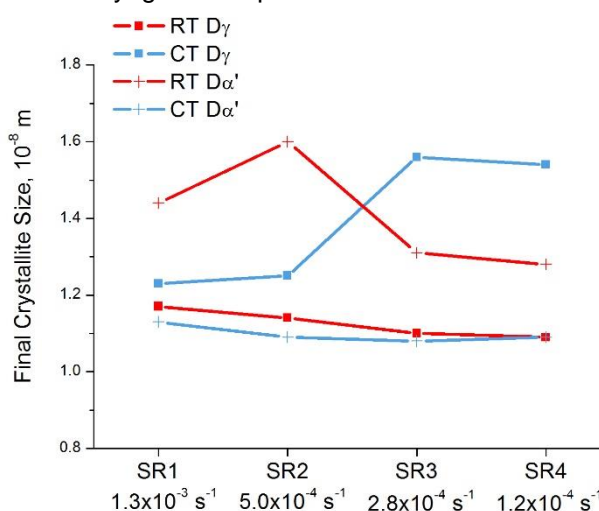
Source: The author.

Looking at the final crystallite size of α'-martensitic phase, it seems that at room temperature the deformation resulted in a larger final crystallite size than at cryogenic temperature. Recalling that BCC has fast recovery kinetics at RT, it is known that at room temperature this phase probably underwent dynamic recovery, and at CT there was a dynamic recovery partial suppression, with a smaller final crystallite size [37,59,63,73].

For the austenitic phase, CT results should present higher microstructural refining due to the more significant twin volume fraction, resulting in smaller twin distance. However, an opposite response is observed; in RT, the final crystallite size is smaller. Thus, it can be assumed that at room temperature there is a more intense grain refinement. However, the final data shows a high interference in diffraction peak, and considering that values are closer, its phenomenon may be associated with the error.

5.5.2 AISI 430

In order to obtain a better visualisation of the change in the XRD profiles during the deformation, such as broadening and displacement of the peaks, strategic points in AISI 430 steel samples tested at a strain rate of $5.0x10^{-4}$ s^{-1}, at room temperature and cryogenic, were chosen by engineering stress-strain curves. The strategic points were: start of the test (0 strain), approximately the beginning of the plastic deformation (0.1) and the medium plastic strain (0.2), at the point of the ultimate tensile strength (0.3) and after the beginning of the necking (0.4). Figure 74 shows these overlapping diffractograms, in which can be seen, in both cases and for both peaks, that there is broadening.

When comparing the material response at room temperature with the cryogenic temperature, it can be noted that there is more considerable variation in the peak of the (110) plane than (200) plane.

The peaks of Figure 75 were fitted with a Gaussian function, just as all diffraction profiles were adjusted for the analysis. With these graphs, the changes during deformation were more evident, as the peaks broadening; remembering that the line broadening can be influenced by three factors, microstrain, crystallite size and instrumental element [88].

Figure 74 - AISI 430 steel samples diffractograms tested on the XTMS line, obtained simultaneously to the mechanical test under strain rate of 5.0×10^{-4} s^{-1}. (a) Room temperature; (b) Cryogenic temperature.
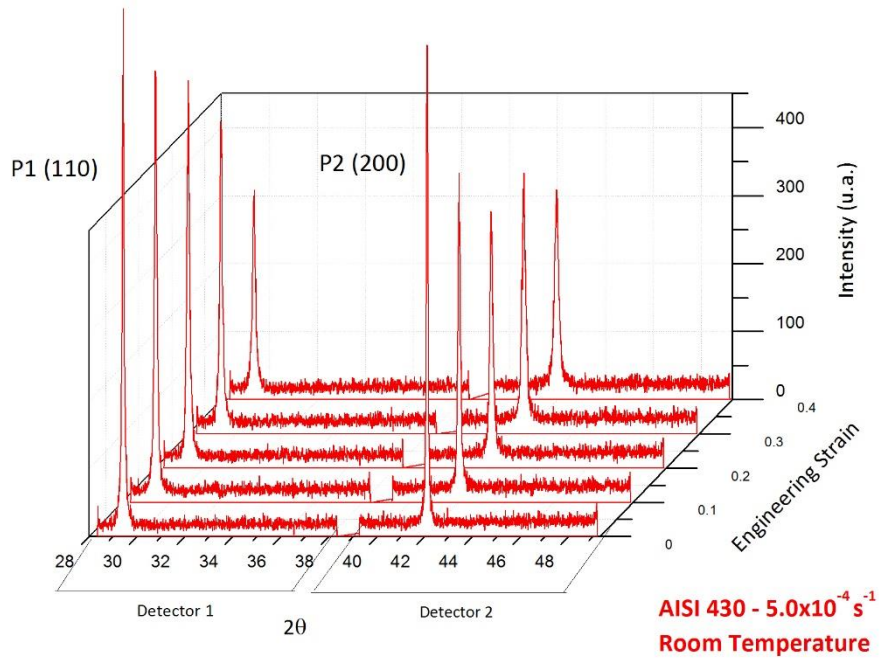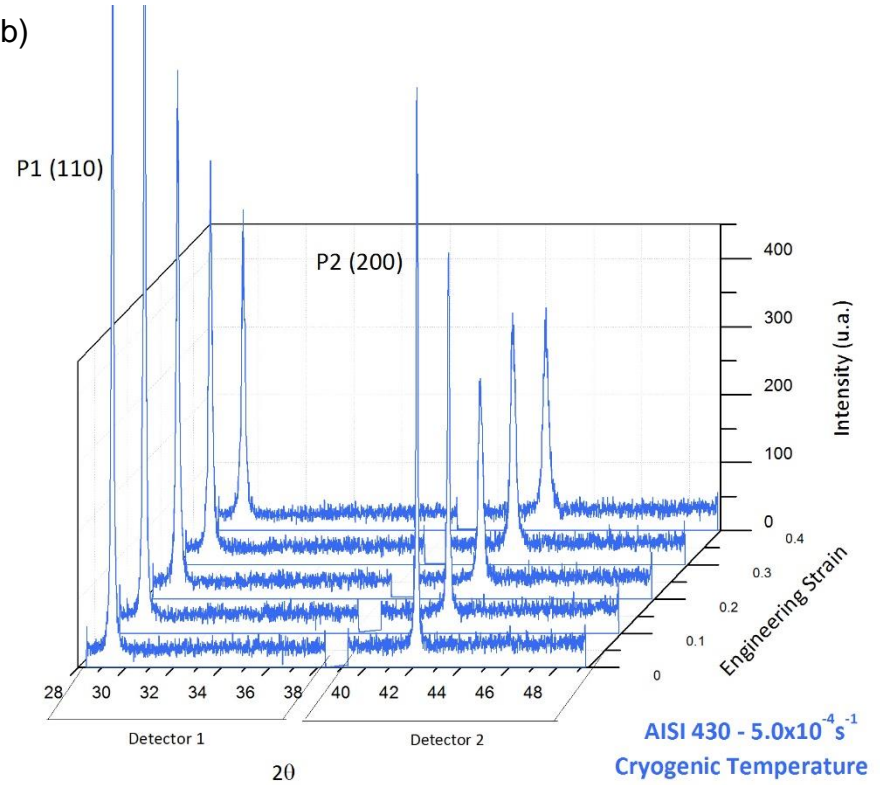
Source: The author.

Figure 75 - Stainless steel AISI 430 peaks (110) and (200), with strain of 0, 0.1, 0.2, 0.3 and 0.4, under strain rate $5.0x10^{-4}$ s^{-1} at room temperature (a) and (b) for peak (110) and (200) respectively, and at cryogenic temperature, (c) and (d) for peak (110) and (200) respectively.
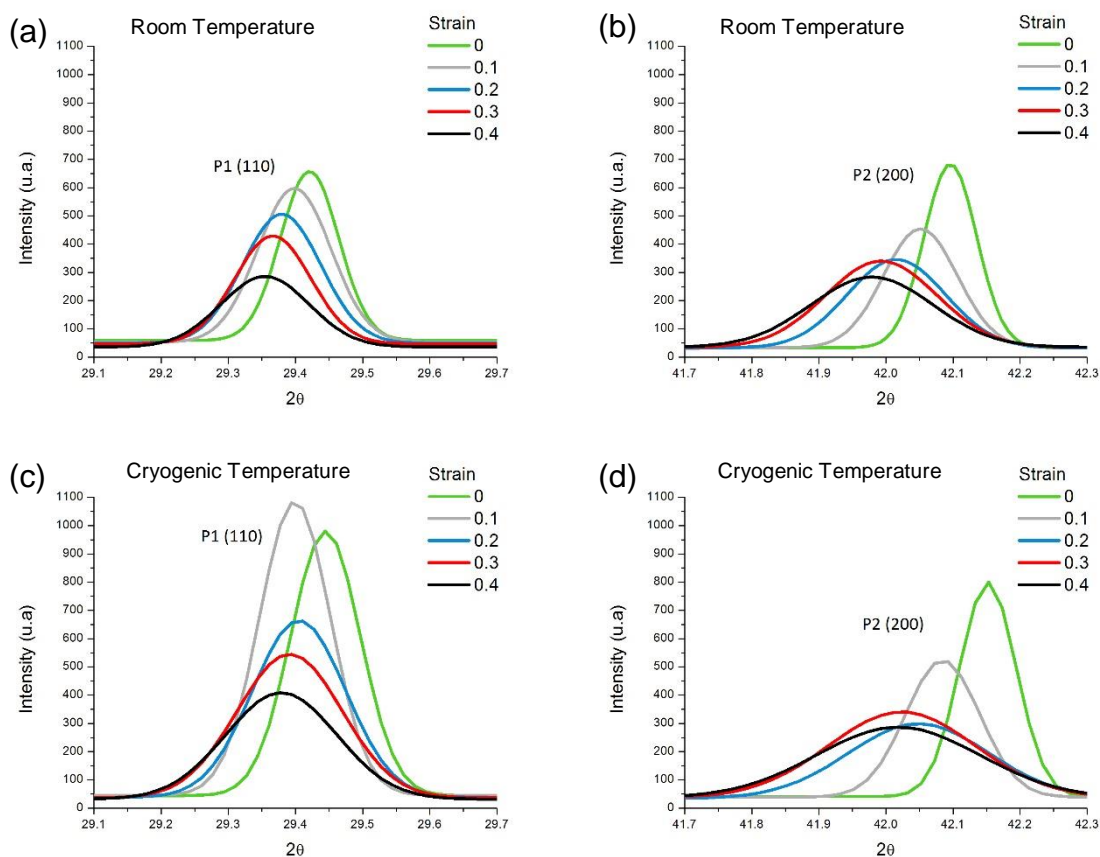
Source: The author.

Due to the similarity of the results obtained with the variation of the strain rate, only a strain rate exemplifies this item.

5.5.2.1 *Microstrain*

Figure 76 shows the AISI 430 steel samples microstrain results. In all test conditions, the microstrain increases with strain increase. The (200) plane exhibits microstrain final values similar to (110) plane. Nevertheless, the more significant microstrain increase is in (200) plane, in all conditions, and, the (200) plane is less dense than (110) plane.

Figure 76 - AISI 430 steel microstrain and stress, by engineering strain. At room temperature with strain rate (a) 1.3x10^{-3} s^{-1}; (b) 5.0x10^{-4} s^{-1}; (c) 2.8x10^{-4} s^{-1} and (d) 1.2x10^{-4} s^{-1} And at cryogenic temperature with strain rate (e) 1.3x10^{-3} s^{-1}; (f) 5.0x10^{-4} s^{-1}; (g) 2.8x10^{-4} s^{-1} and (h) 1.2x10^{-4} s^{-1}.
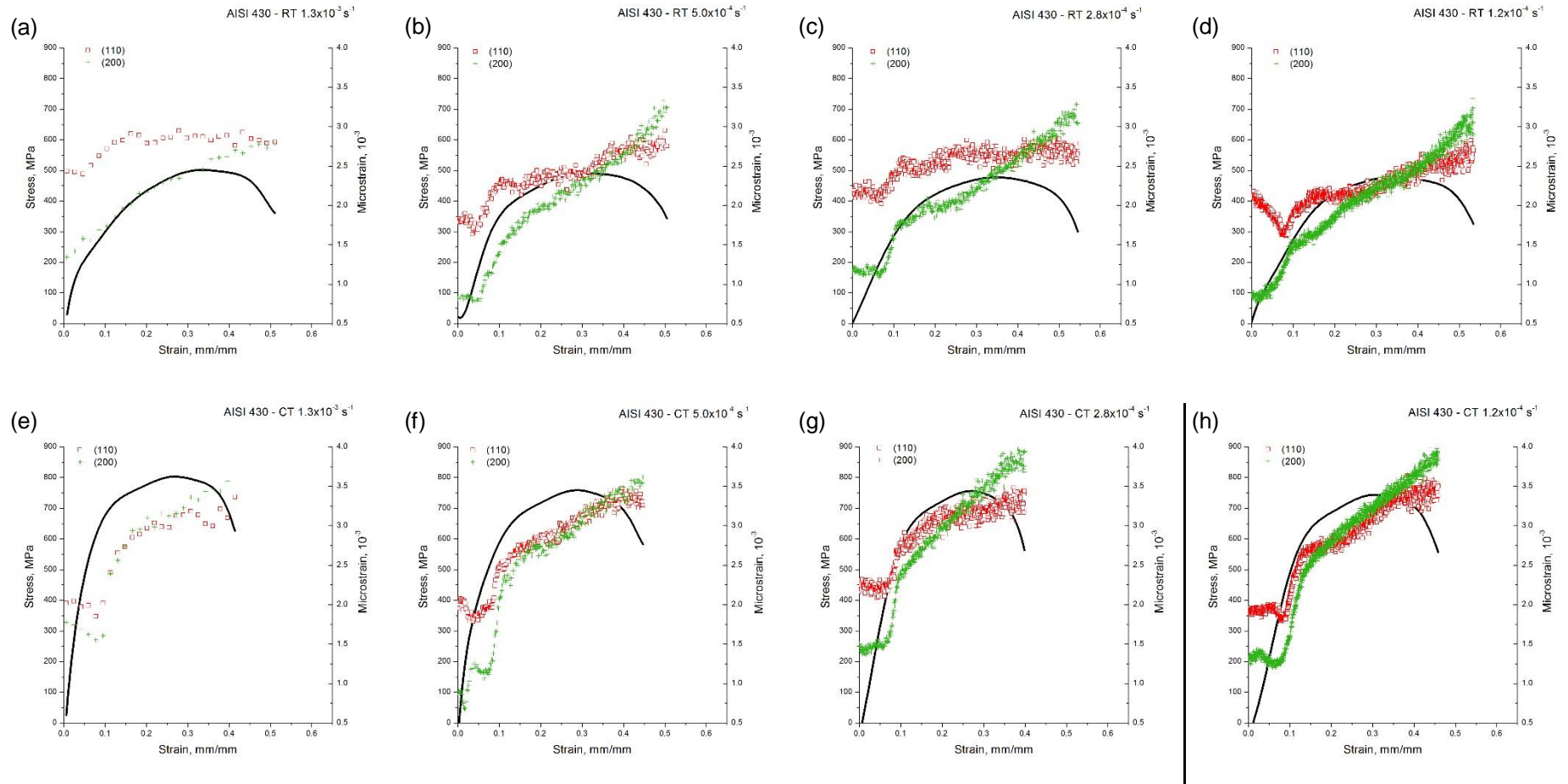
Source: The author.

The microstrain variation (final microstrain - initial microstrain) was calculated, as shown in Figure 77, to improve the visualisation of temperature and strain rate variation influence. In this graph, it is evident that, once again, the bigger variation is in (200) plane, in all conditions.

Figure 77 - Microstrain variation in (110) and (200) planes of AISI 430 steel, at room and cryogenic temperatures, according to strain rate.
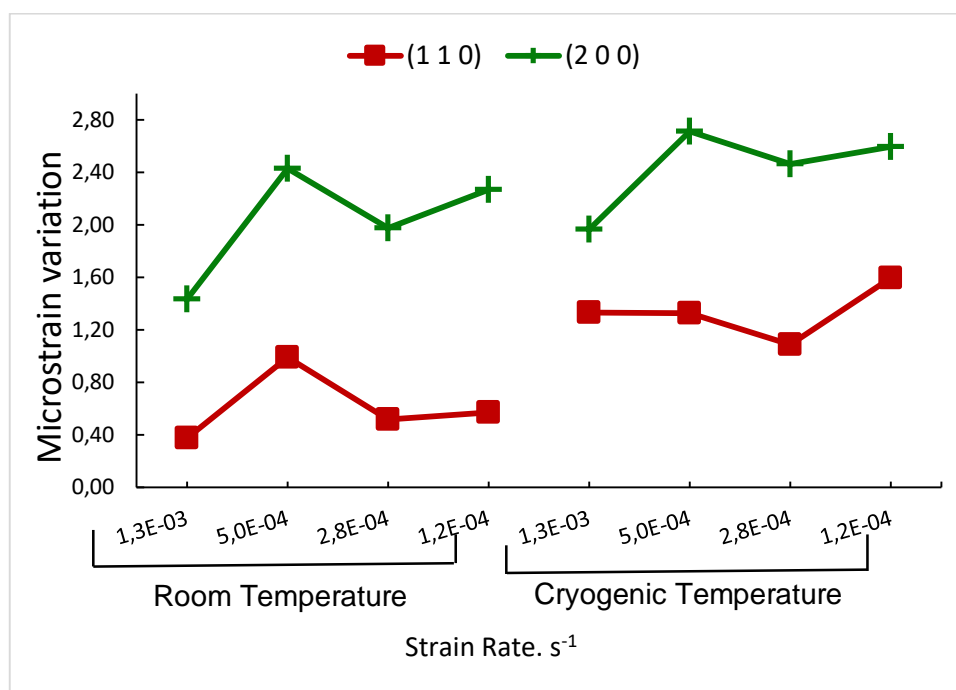
Source: The author.

The result at room and cryogenic temperatures showed that the most significant difference was in (100) plane deformed at CT. There was a small difference for (200) plane at CT. Temperature decrease causes increased difficulty in moving dislocations, favouring twins. Besides that, at room temperature can occur dynamic recovery for BCC metals, that exhibit a high SFE, but temperature reduction causes an SFE reduction, and can promote partial suppression of dynamic recovery, storing more energy.

About strain rate influence, the (100) plane at RT and (200) plane at RT e CT exhibit the same tendency, showing more considerable microstrain variation at 5.0×10^{-4} s^{-1} strain rate. However, the difference between strain rates are small, and the temperature effect is more evident. It is expected that little temperature alterations result in a significant modification in dislocation substructure, while large changes in strain rate influence relatively less [37].

5.5.2.2 *Crystallite Size*

Figure 78 shows the crystallite size with the strain course in all conditions analysed for AISI 430 steel. In all cases, there is a decrease in crystallite size, which it is associated with microstructural refining produced by the subgrains. The initial crystallite values have a high dispersion due to not satisfactory initial diffractograms quality. However, it is possible to perceive a great microstructural refinement from the beginning of the strain until plastic deformation start, around 0.1 mm/mm engineering strain. After that, it reaches a plateau where there is reduction of the crystallite size with strain, but the rate is minor than before. It indicates that the crystallite size is close to the minimum size. At cryogenic temperature, the crystallite size finishes with minor values than at room temperature; it indicates that there is more microstructural refinement at CT.

Figure 78 - AISI 430 steel crystallite size and stress, by engineering strain. At room and cryogenic temperatures, with strain rate: (a) 1.3×10^{-3} s^{-1}; (b) 5.0×10^{-4} s^{-1}; (c) 2.8×10^{-4} s^{-1}; (d) 1.2×10^{-4} s^{-1}
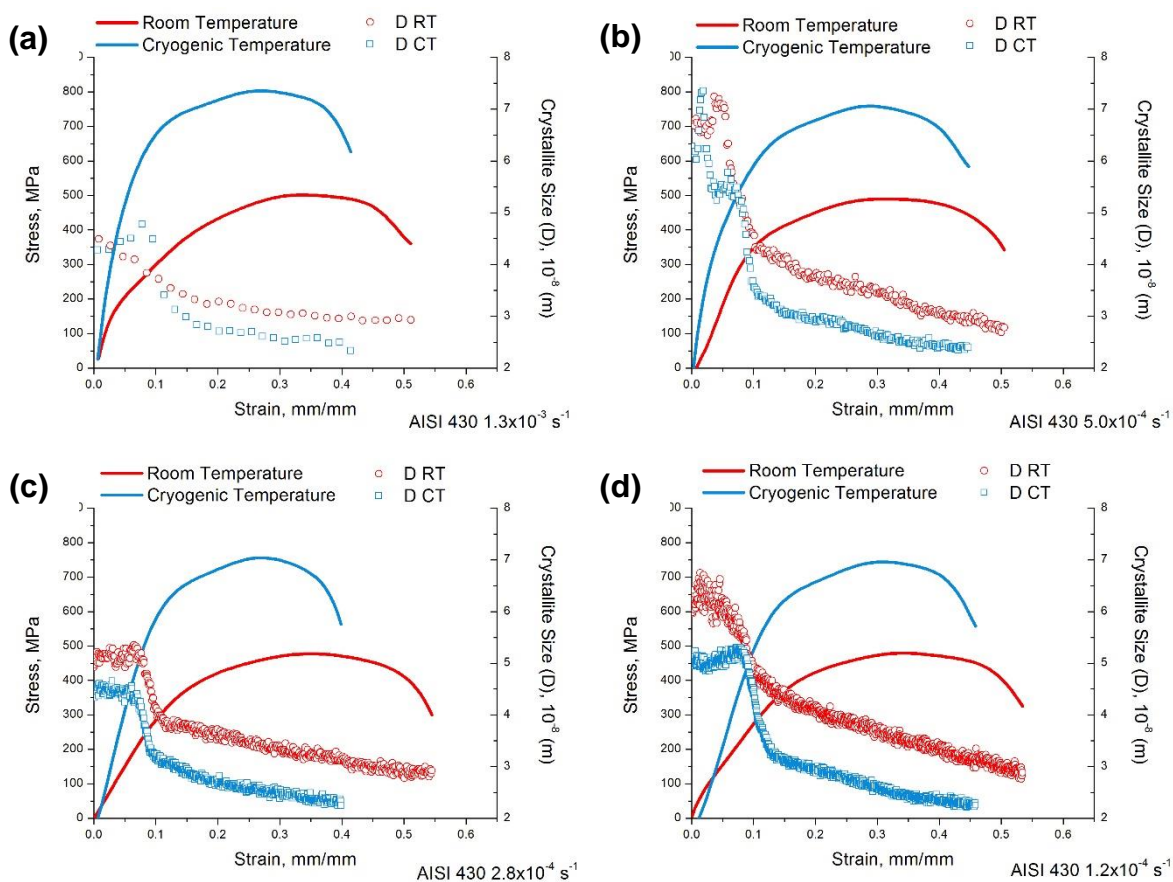
Source: The author.

Recalling that BCC ferrite has fast recovery kinetics at RT due to high dislocation mobility (high SFE), it can be affirmed that at RT dynamic recovery occurred. Decreasing the temperature, there was bigger difficulty to move dislocations, thus occurring dynamic recovery partial suppression. The occurrence or not of this recovery will result in larger or smaller crystallite size, respectively [37,59,63,73].

Figure 79 indicates the final values of crystallite size for AISI 430 according to the strain rate. Comparing the final values, in both temperatures, there is a smaller final crystallite size at the cryogenic temperature. Once again, inferior crystallite size at CT indicates that there is more microstructural refinement.

Figure 79 - Final values of crystallite size for AISI 430 steel according to strain rate, at room and cryogenic temperatures.
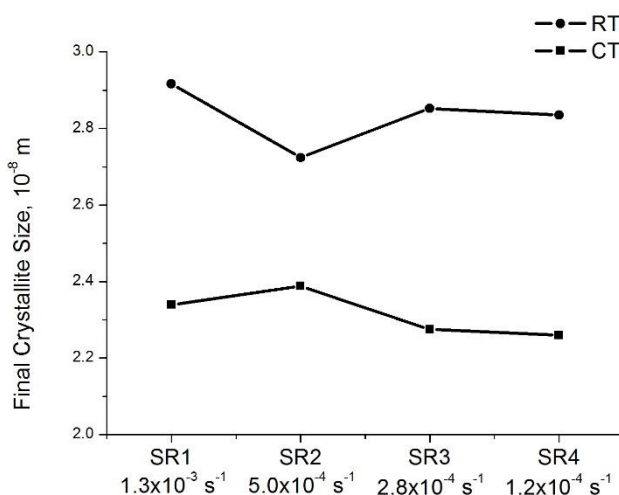
Source: The author.

Analysing the strain rate influence, the final crystallite size has a similar tendency with strain rate at room and cryogenic temperatures, decreases when decreasing strain rate, in general. Thus, it may be affirmed that quicker strain rates result in a more significant dynamic recovery, showing larger crystallite size. For both temperatures, the 5.0×10^{-4} s^{-1} strain rate escapes from the tendency, at CT, the strain rate showed the major final crystallite size, and at RT, this strain rate exhibited the minor value. However, the difference between strain rates may be attributed to the error because final crystallite size and strain rates values are very close.

6 CONCLUSIONS

About AISI 304 stainless steel:

1- In mechanical behaviour, at low temperatures, there are ductility loss and strength increase. At cryogenic temperature, it was possible to verify the slope change in the stress-strain curve, which occurs due to the secondary hardening from the martensitic transformation. At room temperature, this behaviour is not visible, because with temperature increase results in a suppression of strain-induced martensite induced formation, due to a SFE increase and a chemical driving force $\Delta G\gamma\rightarrow\alpha'$ reduction.

2- About EBSD analysis, when comparing the initial condition with deformed at room and cryogenic temperatures, it can be seen a larger presence of the BCC phase (α'-martensite) and a less FCC phase (austenite) when deforming, in addition to a large part not indexed that is the result of high quantities of dislocations due to deformation. At cryogenic temperature, it can also be seen that larger part not indexed, indicating superior work hardening.

3- In both temperatures, the fracture surface was fully presented with dimples, a ductile fracture characteristic. In the samples submitted to the CT tests, dimples are subtly smaller and less deep, where occurred a higher number of void nucleation than at RT, pointing a larger amount of austenite-martensite interfaces available. Comparing both temperatures responses, observed in RT tests; there was a more significant than at CT. This result shows that deformed material at RT has higher ductility than materials deformed at CT.

4- During deformation the (101) ε-martensite peak appeared, at both room and cryogenic temperatures. The microstrain in austenite planes (111), (200) and (220) increased with plastic deformation, because there is an accumulation of defects in this phase, initially being responsible for increasing work hardening. With deformation, driving force intensifies for the stress-induced transformation, which increases work hardening.

Increase of α'-martensite occurred due to defects density increase in austenite. For α'-martensite planes, microstrain increased during the initial yielding and then decreased; it is assumes that dynamic recovery occurred.

5-   Strain values for 50% martensitic transformation at room and cryogenic temperatures showed considerable anticipation at CT. At higher temperature, there is suppression of strain-induced martensite formation, being that rising temperature leads to austenite stability increases.

6-   Martensitic transformation rate (MTR), in both cases, after the start strain, increased to the maximum and decreased after the maximum value. Therefore, MTR at CT increased quickly right at the beginning strain, and there is an advancing to reach maximum MTR value observed when compared with RT. While at RT, the maximum point occurs at larger strain, and there is a lower maximum MTR value.

7- Martensitic transformation rate with the increasing strain rate showed had delayed maximum MTR, which occurs with more considerable strain. It happened due to the more significant effect of adiabatic heating with the strain rate increase, leading to larger austenite stability. The maximum MTR values at CT were smaller with increasing strain rate; the thermal effect causes an increase in the stability of austenitic stainless steel and reduces the saturation fraction of martensite.

8- Looking at the final crystallite size of α'-martensitic phase, at room temperature the deformation resulted in a larger final crystallite size than at cryogenic temperature. At room temperature, this phase has undergone dynamic recovery, and at CT, there was a dynamic recovery partial suppression, with a smaller final crystallite size.

9- With the additional analysis made in the conventional X-ray diffractometer, it can be observed that a large part of the initial martensite volume fraction was removed with grinding and electrolytically polish.

About AISI 430 stainless steel:

1- A reduction in temperature caused an increase in ultimate tensile strength. The effects of an increase in strain rate had a similar impact of decreases in temperature. Considering only the strain rates defined at work initially, 1.3×10^{-3} s^{-1}, 5.0×10^{-4} s^{-1}, 2.8×10^{-4} s^{-1} and 1.2×10^{-4} s^{-1}, a significant increase of 75%, approximately, in the UTS obtained when the material is deformed at cryogenic temperature and only around 15% of loss in total and uniform elongation. However, one more strain rate (6.6×10^{-2} s^{-1}) was tested at cryogenic temperature, and it was able to overcome the point of ductile-brittle transition. It can be affirmed that strain rates utilised at cryogenic temperature were close to the ductile-brittle transition limit.

2- The fracture surface area and fracture aspect indicated a more ductile fracture in RT. The ductile mechanism and cleavage compete with each other in the ductile-brittle transition, and the phenomenon could be observed in fracture surface analyse at CT, where the faster strain rates show a more significant presence of brittle fracture characteristics. All strain rates used at CT were close to the ductile-fragile transition point, but only the 6.6×10^{-2} s^{-1} strain rate was able to overcome the transition and turned brittle. Strain rates revealed to have a little mechanical effect, but influent significant the failure mode.

3- In all tests, there is a decrease in crystallite size and microstrain under deformation. The more significant microstrain increase is in (200) plane, in all conditions. The result at room and cryogenic temperatures showed that the more significant difference in microstrain was in (100) plane deformed at CT. At cryogenic temperature, the crystallite size finishes with minor values than at room temperature; it indicating that there is more microstructural refine at CT.

7 SUGGESTIONS FOR FUTURE WORKS

- Perform tests on AISI 304 and AISI 430 at different low temperatures;
- For both materials, perform analysis of defect density during deformation;
- Use other methods of data processing for X-ray diffractometers;
- Evaluate the material's behaviour, *in situ*, at faster strain rates (possibly in the Sirius, new light ring of the CNPEM);
- Measure SFE through the X-ray diffraction data for several stainless steels by checking / proposing equations;
- Evaluate the stress-induced transformation in other austenitic stainless steels, in order to compare the composition influence;
- Search factors, such as grain size, temperature and strain rate that would change the ductile-brittle transition point of the AISI 430 steel.

REFERENCES

1.   BLAIR, M. Cast Stainless Steels. In: **ASM Metals Handbook 1: Properties and Selection Irons Steels and High-Performance Alloys**. 10ª. ed. ASM International, v. 1, 1990. p. 2195-2248.

2.   ASM METALS HANDBOOK COMMMITE. Alloy Digest Sourcebook: Stainless Steels. **ASM International Bookstore**, 2000. Disponivel em: <www.asminternational.org/bookstore>. Acesso em: 23 abril 2018.

3.   ATLAS SPECIALTY METALS. **The Atlas Specialty Metals:** Technical Handbook of Stainless Steels. Atlas Specialty Metals Technical Services Department, 2008.

4.   BHADESHIA, H. K. D. H.; HONEYCOMBE, R. W. K. **Steels Microstructure and Properties**. 3º. ed. Cambridge: Butterworth-Heinemann, Elsevier Ltd., 2006.

5.   SHISHIRM, P. *et al*. Effect of sintering temperature on the mechanical and electrochemical properties of austenitic stainless steel. **Materials Science & Engineering: A**, Kanpur, UP, Índia, v. 556, p. 271-277, Outubro 2012.

6.   WASHKO, S. D.; AGGEN, G. Wrought Stainless Steels. In: **ASM Metals Handbook 1: Properties and Selection Irons Steel and High-Performance Alloys**. ASM International, v. 1, 1990. p. 2004-2194

7.   PADILHA, A. F.; GUEDES, L. C. **Aços inoxidáveis Austeníticos**. Hemus, 2004.

8.   CHIAVERINI, V. **Aços e Ferros Fundidos**. 7ª. ed. São Paulo: Associação Brasileira de Metalurgia e Materiais - ABM, 2005.

9.   IRON & STEEL SOCIETY. **Steel Products Manual:** Stainless Steels. Iron & Steel Society, 1999.

10.   KLAR, E.; SAMAL, P. K. **Powder Metallurgy Stainless Steels**: **Processing, Microstructures, and Properties**. ASM International, 2007.

11.   TALONEN, J.; HÄNNINEN, H. Formation of shear bands and strain-induced martensite during plastic deformation of metastable austenitic stainless steels. **Acta Materialia**, v. 55, p. 6108–6118, 2007.

12.   HALLER, M. N. Cemented Carbides: Metallographic Techniques and Microstructures. In: **ASM Metals Handbook 9: Metallography and Microstuctures**. ASM International, v. 9, 1992. p. 513-545.

13.   KRAUSS, G. **Steels - Processing, Structure, and Performance**. ASM International, 2005.

14. MEYERS, M.; CHAWLA, K. **Mechanical Behavior of Materials**. 2ª. ed. New York: Cambridge University Press, 2009.

15. PORTER, D. A.; EASTERLING, K. E.; SHERIF, M. Y. **Phase Transformations in Metals and Alloys**. 3ª. Ed. Taylor & Francis Group, 2009.

16. ABBASCHIAN, R. *et al*. **Physical Metallurgy Principles**. 4ª. ed. Cengage Learning, 2009.

17. HECKER, S. S. *et al*. Effects of Strain State and Strain Rate on Deformation-Induced Transformation in 304 Stainless Steel: Part I. Magnetic Measurements and Mchanical Behavior. **Metallurgical Transactions A**, v. 13A, p. 619-626, abril 1982.

18. FERREIRA, P. J. *et al*. Microstructure Development during High-Velocity Deformation. **Metallurgical and Materials Transactions A**, v. 35A, p. 3091-3101, 2004.

19. MANGONON, P. L.; THOMAS, G. Structure and Properties of Thermal-Mechanically Treated 304 Stainless Steel. **Metallurgical Transactions**, v. 1, p. 1587-1594, 1970.

20. MANGONON, P. L.; THOMAS, G. The Martensite Phases in 304 Stainless Steel. **Metallurgical Transactions**, v. 1, p. 1577-1586, 1970.

21. TSUCHIDA, N. *et al*. Effects of Temperature and Strain Rate on TRIP Effect in SUS301L Metastable Austenitic Stainless Steel. **ISIJ International**, v. 53, n. 10, p. 1881–1887, 2013.

22. LISCHKA, F. T.; OLIVEIRA, C. A. S. The study of TRIP effect in an austenitic stainless steel AISI 304. **Journal of Achievements in Materials and Manufacturing Engineering**, v. 71, n. 1, p. 34-38, 2015.

23. TSUCHIDA, N. *et al*. Stress-Induced Martensitic Transformation Behaviors at Various Temperatures and Their TRIP Effects in SUS304 Metastable Austenitic Stainless Steel. **ISIJ International**, v. 51, n. 1, p. 124–129, 2011.

24. LU, J. *et al*. Stacking fault energies in austenitic stainless steels. **Acta Materialia**, v. 111, p. 39-46, 2016.

25. LEFEBVRE, G. **Relationship Between Microstructure, Texture and Ridging in Ferritic Stainless Steels**. A Thesis Submitted in Partial Fulfillment of the Requirements for the Degree of Doctor, The University of British Columbia. p. 203. 2014.

26. DA COSTA, A. L. V.; MEI, P. R. **Aços e Ligas Especiais**. 3ª. ed. Blucher, 2010.

27. GROBNER, P. J. The 885º F (475º C) Embrittlement of Ferritic Stainless Steels. **Metallurgical Transactions**, v. 4, p. 251-260, 1973.

28. ZHAO, Z.; RADOVITZKY, R.; CUITIÑO, A. A study of surface roughening in fcc metals using direct numerical simulation. **Acta Materialia**, v. 52, p. 5791-5804, 2004.

29. SHIN, H. J. *et al*. The effect of texture on ridging of ferritic stainless steel. **Acta Materialia**, v. 51, p. 4693–4706, 2003.

30. MA, X. *et al*. An Analysis of Ridging of ferritic stainless steel 430. **Materials Science & Engineering A**, v. 685, p. 358-366, 2017.

31. WU, P. D. *et al*. Analysis of ridging in ferritic stainless steel sheet. **Materials Science and Engineering A**, v. 423, p. 300–305, 2006.

32. ENGLER, O.; HUH, M.; TOMÉ, C. N. Crystal-Plasticity Analysis of Ridging in Ferritic Stainless Steel Sheets. **Metallurgical and Materials Transactions A**, v. 36A, p. 3127-3139, 2005.

33. WU, P. D.; LLOYD, D. J.; HUANG, Y. Correlation of ridging and texture in ferritic stainless steel sheet. **Materials Science and Engineering A**, v. 427, p. 241–245, 2006.

34. LEFEBVRE, G. *et al*. Accounting for local interactions in the prediction of roping of ferritic stainless steel sheets. **Modelling and Simulation in Materials Science and Engineering**, v. 20, p. 1-16, 2012.

35. TIKHOVSKIY, I.; RAABE, D.; ROTERS, F. Simulation of earing of a 17% Cr stainless steel considering texture gradients. **Materials Science and Engineering A**, v. 488, p. 482–490, 2008.

36. DEFILIPPI, J. D.; CHAO, H. C. Effect of Chromium and Molybdenum Segregation on the Ridging Behavior of Type 434 Stainless Steel. **Metallurgical Transactions**, v. 2, p. 3209-3216, 1971.

37. PADILHA, A. F.; SICILIANO JÚNIOR, F. **Encruamento, Rescristalização, Crescimento de Grão e Textura**. 3ª, rev. e ampl. ed. São Paulo: ABM, 2005.

38. MEYERS, M.; CHAWLA, K. **Princípios de Metalurgia Mecânica**. São Paulo: Edgard Blücher, 1982.

39. DIETER, G. E. **Metalurgia Mecânica**. 2ª. ed. Rio de Janeiro: Guanabara Dois, 1981.

40. HULL, D.; BACON, D. J. **Introduction to Dislocations**. 5ª. ed. Elsevier Ltd., 2011.

41. SANTOS, R. G. **Transformação de Fases em Materiais Metálicos**. Campinas: Editora da Unicamp, 2006.

42. KUHLMANN-WILSDORF, D. Questions you always wanted (or should have wanted) to ask about workhardening. **Materials Research Innovations**, v. 1, n. 4, p. 265-297, 1998.

43. SCHÖN, C. G. **Mecânica dos Materiais**. USP. São Paulo. 2010. Apostila.

44. KUHLMANN-WILSDORF, D. Theory of Plastic Deformation:- properties of low energy dislocation structures. **Materials Science and Engineering**, v. A113, p. 1-41, 1989.

45. TSUCHIDA, N. *et al.* Effects of Temperature and Strain Rate on Tensile Properties of a Lean Duplex Stainless Steel. **ISIJ International**, v. 54, p. 1971-1977, 2014.

46. CAMPOS, M. F.; FARIAS, M. C. M.; PADILHA, A. F. Uma compilação crítica de valores de energia de defeito de empilhamento para diversos metais. In: **Boletim Técnico da Escola Politécnica da USP 9901**. São Paulo: 1999. p. 1-20.

47. MEYERS, M. A.; VÖHRINGER, O.; LUBERDA, V. A. The Onset Of Twinning in Metals: A Constitutive Description. **Acta Materialia**, v. 49, p. 4025-4039, 2001.

48. PADILHA, A. F. **Materiais de Engenharia:** microestrutura e propriedades. São Paulo: Hemus, 1997.

49. HUMPHREYS, F. J.; HATHERLY, M. **Recrystallization and Related Annealing Phenomena**. 2ª. ed. Elsevier, 2004.

50. GONG, Y. L. *et al.* The influence of strain rate, deformation temperature and stacking fault energy on the mechanical properties of Cu alloys. **Materials Science & Engineering A**, v. 583, p. 199-204, 2013.

51. WEERTMAN, J. Zener-Stroh crack, Zener-Hollomon parameter, and other topics. **Journal of Applied Physics**, v. 60, p. 1877-1887, 1986.

52. BEAUDOIN, A. J.; ENGLER, O. Deformation Processing: Texture. In: MARTIN, J. W. **Concise Encyclopedia of the Structures of Materials**. Elsevier, 2007. p. 161-169.

53. WILKINSON, A. J. Deformation Textures. In: MARTIN, J. W. **Concise Encyclopedia of the Structure of Materials.** Elsevier, 2007. p. 169-173.

54. JENSEN, D. J. Annealing Textures. In: MARTIN, J. W. **Concise Encyclopedia of the Structure of Materials**. Elsevier, 2007. p. 7-11.

55. REED, R. P. Trends and Advances in Cryogenic Materials. In: TIMMERHAUS, K. D.; REED, R. P. **Cryogenic Engineering - Fifty Year of Progress**. Springer, 2007. p. 52-83.

56. WALSH, R. P. Tension and compression testing at low temperatures. In: **ASM Metals Handbook 8: Mechanical testing and evaluation**. ASM International, v. 8, 2004. p. 384-402.

57. RADEBAUGH, R. Historical Summary of Cryogenic Activity Prior to 1950. In: TIMMERHAUS, K. D.; REED, R. P. **Cryogenic Engineering:** Fifty Years of Progress. Springer, 2007. p. 3-27.

58. KULA, E. B.; DE SISTO, T. S. Plastic Behavior of Metals at Cryogenic Temperatures. In: MATERIALS, A. S. F. T. A. **Behavior of Materials at Cryogenic Temperatures**. Baltimore: ASM, 1966. p. 3-31.

59. KON'KOVA, T. N.; MIRONOV, S. Y.; KORZNIKOV, A. V. Severe Cryogenic Deformation of Copper. **The Physics of Metals and Metallography**, v. 109, n. 2, p. 171-176, 2010.

60. WIGLEY, D. A. **Mechanical Properties of Materials at Low Temperatures**. New York : Plenum Press , 1971.

61. ROY, B.; KUMAR, R.; DAS, J. Effect of cryorolling on the microstructure and tensile properties of bulk nano-austenitic stainless steel. **Materials Science & Engineering A**, v. 631, p. 241-247, 2015.

62. CHUNA, Y. B. *et al.* Combined effects of grain size and recrystallization on the tensile properties of cryorolled pure vanadium. **Materials Science and Engineering A**, v. 508, p. 253-258, 2009.

63. KON'KOVA, T. *et al.* Microstructural response of pure copper to cryogenic rolling. **Acta Materialia**, v. 58, p. 5262-5273, 2010.

64. SARMA, V. S. *et al.* Role of stacking fault energy in strengthening due to cryo-deformation of FCC. **Materials Science and Engineering A**, n. 527, p. 7624-7630, 2010.

65. HUANG, Y.; PRANGNELL, P. B. The effect of cryogenic temperature and change in deformation mode on the limiting grain size in a severely deformed dilute aluminium alloy. **Acta Materialia**, v. 56, p. 1619-1632, 2008.

66. MAGALHÃES, D. C. C. **Microestrutura e propriedades mecânicas da liga AA6061 processada por deformação plástica severa em temperatura criogênica**. Tese (Doutorado em Ciência e Engenharia de Materiais) - Universidade Federal de São Carlos. São Carlos, p. 145. 2017.

67. AHN, S. H. *et al.* Microstructural refinement and deformation mode of Ti under cryogenic channel die compression. **Materials Science and Engineering A**, v. 528, p. 165-171, 2010.

68. VALIEV, R. Z. *et al.* Producing Bulk Ultrafine-Grained Materials by Severe Plastic. **JOM**, v. 58, n. 4, p. 1216-1226, 2016.

69. ZAHID, G. D.; HUANG, Y.; PRANGNELL, P. B. Microstructure and texture evolution during annealing a cryogenic-SPD processed Al-alloy with a nanoscale lamellar HAGB grain structure. **Acta Materialia**, v. 57, p. 3509–3521, 2009.

70. EDALATI, K. *et al*. Influence of severe plastic deformation at cryogenic temperature on grain refinement and softening of pure metals: investigation using high-pressure torsion. **Materials Science and Engineering: A**, v. 613, p. 103-110, 2014.

71. MAEDA, M. Y. **Estudo da deformação criogênica de alumínio, cobre e prata**. Dissertação (Mestrado em Desenvolvimento e Caracterização de Materiais) - Universidade Estadual de Ponta Grossa. Ponta Grossa, p. 82. 2017.

72. IZUMI, M. T. **Estudo *in situ* da deformação criogênica de metais CFC de diferentes energias de defeito de empilhamento**. Dissertação (Mestrado em Desenvolvimento e Caracterização de Materiais) - Universidade Estadual de Ponta Grossa. Ponta Grossa, p. 87. 2018.

73. MAEDA, M. Y. et al. Study of Cryogenic Rolling of FCC Metals with Different Stacking Fault Energies. **Materials Research**, n. 20, p. 716-721, 2017.

74. IZUMI, M. T. et al. In Situ X-Ray Diffraction Analysis of Face-Centered Cubic Metals Deformed at Room and Cryogenic Temperatures. **Journal of Materials Engineering and Performance**, v. 28, n. 8, p. 4658-4666, 2019.

75. MAGALHÃES, D. C. C. et al. Asymmetric cryorolling of AA6061 Al alloy: Strain distribution, texture and age hardening behavior. **Materials Science & Engineering A**, n. 736, p. 53-60, 2018.

76. CAHN, R. W.; HAASEN, P. (Eds.). **Physical Metallurgy**. 4ª. ed. Elsevier Science B.V., v. 3, 1996.

77. WESSEL, E. T. Some Basic and Engineering Considerations Regarding the Fracture of Metals at Cryogenic Temperatures. In: **Behavior of Materials at Cryogenic Temperatures**. American Society for Testing and Materials, 1966. p. 32-59.

78. ASKELAND, D. R.; FULAY, P. P.; BHATTACHARYA, D. K. **Essentials of Materials Science and Engineering**. 2º. ed. Cengage Learning, 2010.

79. SMIDA, T.; BOSANSKý, J. Deformation twinning and its possible influence on the ductile brittle transition temperature of ferritic steels. **Materials Science and Engineering A**, v. 287, p. 107-115, 2000.

80. RODRIGUES, J. A. **Raios X Difração e Espectroscopia**. São Carlos: EduFSCar, 2005. Série Apontamentos.

81. PADILHA, A. F.; AMBROZIO FILHO, F. **Técnicas de Análise Microestrutural**. Hemus, 2004.

82. JENKINS, R.; SNYNDER, R. I. **Introduction to X-ray Powder Diffractometry**. John Wiley & Sons, Inc, 1996.

83. SURYANARAYANA, C.; NORTON, M. G. **X-Ray Diffraction - A Practical Approach**. Springer Science+Business Media, LLC, 1998.

84. CULLITY, B. D.; STOCK, S. R. **Elementos of X-Ray Diffraction**. 3ª. ed. Person Education Limited, 2014.

85. SANDS, D. E. **Introducción a la Cristalografía**. Editorial Reverté, S. A., 1993.

86. DINNEBIER, R. E.; BILLINGE, S. J. L. Principles of Powder Diffraction. In: DINNEBIER, R. E.; BILLINGE, S. J. L. **Powder Diffraction - Theory and Practice**. RSC Publishing , 2008. p. 1-19.

87. GIACOVAZZO, C. The diffraction of X-rays by crystals. In: GIACOVAZZO, C., *et al*. **Fundamentals of Crystallography**. Oxford University Press, 1992. p. 141-228.

88. ICHIKAWA, R. U. **Aplicações do método de Warren-Averbach de análise de perfis de difração**. Dissertação (Mestrado em Ciências – Área de Tecnologia Nuclear e Materiais) – Instituto de Pesquisas Energéticas e Nucleares (IPEN). São Paulo. 2013.

89. SURYANARAYANA, C. Mechanical alloying and milling. **Progress in Materials Science**, v. 46, p. 1-184, 2001.

90. CNPEM. UVX. **Laboratório Nacional de Luz Síncrotron**. Disponivel em: <https://www.lnls.cnpem.br/uvx/maquina/>. Acesso em: 10 maio 2018.

91. LNNANO, CPM. **XTMS Experimental Station User's Guide**. Centro Nacional de Pesquisa em Energia e Materiais - CNPEM. p. 19. 2017.

92. FARIA, G. *et al*. Advanced Facility for Parallel Thermo-Mechanical Simulation and Synchrotron X-Ray Diffraction. In: **In-situ Studies with Photons, Neutrons and Electrons Scattering II**. Springer International Publishing, 2014. p. 245-259.

93. DOUTHETT, J. Heat Treating of Stainless Steels. In: **Heat Treating**. ASM Metals Handbook, v. 4, 1991. p. 1682-1757.

94. TALONEN, J. *et al*. Effect of Strain Rate on the Strain-Induced y-> alfa' Martensite Transformation and Mechanical Properties of Autenitic Atainless Steels. **Metallurgical and Materials Transactions A**, v. 36 A, p. 421-432, 2005.

95. WARREN, B. E. **X-Ray Diffraction**. New York: Dover Publication, 1990.

96. HOYOS, J. J. *et al*. *In Situ* Synchrotron Radiation Measurements During Axial Strain In Hydrogen Cathodically Charged Duplex Stainless Steel SAF 2205. **Materials Research**, v. 21, n. 2, p. 1-7, 2017.

97. STOKES, A. R.; WILSON, A. J. C. The diffraction of X rays by distorted crystal aggregates – I. **Proceedings of the Physical Society**, v. 56, n. 3, p. 174-181, 1944.

98. GAUSS, C. *et al*. *In situ* synchrotron X-ray evaluation of strain-induced martensite in AISI 201 austenitic stainless steel during tensile testing. **Materials Science and Engineering: A**, v. 651, p. 507-516, 2016.

99. MICHLER, T. *et al*. Microstructural properties controlling hydrogen environment embrittlement of cold worked 316 type austenitic stainless steels. **Materials Science & Engineering A**, v. 628, p. 252-261, 2015.

100. Standard Practice for X-Ray Determination of Retained Austenite in Steel with Near Random Crystallographic Orientation. ASTM International. p. 7. 2013.

101. MATSUMURA, O.; SAKUMA, Y.; TAKECHI, H. TRIP and its kinetic aspects in austempered 0.4C-1.5Si-0.8Mn steel. **Scripta Metallurgica**, EUA, v. 21, p. 1301-1306, 1987.

102. WEIDMANN, E. Electrolytic Polishing. In: **ASM Metals Handbook 9: Metallography and Microstructures**. ASM International, v. 9, 1992. p. 57-75.

103. COLPAERT, H. **Metalografia dos Produtos Siderurgicos Comuns**. Edgard Blücher, 1974.

104. Standard Test Method for Microindentation Hardness of Materials. **American Society for Testing and Materials, ASTM specification E 384 - 17**. 2017.

105. REVANKAR, G. Introduction to Hardness Testing. In: **ASM Metals Handbook 8: Mechanical Testing and Evaluation**. ASM International, v. 8, 2003. p. 416-428. Versão Eletrônica.

106. VOORT, G. F. Microindentation Hardness Testing. In: **ASM Metals Handbook 8 - Mechanical Testing and Evaluation**. ASM International, v. 8, 2003. p. 469-495.

107. Standard Test Method for Determining Average Grain Size. **American Society for Testing and Materials, ASTM specification E112-13**. p. 28. 2013.

108. SCHARAMM, R. E.; REED, R. P. Stacking Fault Energies of Seven Commercial Austenitic Stainless Steels. **Metallurgical Transactions A**, v.6A, p. 1345-1351, 1975.

109. TALONEN, J. **Effect of Strain-Induced alfa'- Martensite Transformation on Mechanical Properties of Metastable Austenitic Stainless Steels**. Doctoral Dissertation - Helsinki University of Technology. Finland, p. 125. 2007.

110. YOO, S. W. *et al*. Temperature and strain rate dependent constitutive model of TRIP steels for low-temperature applications. **Computational Materials Science**, n. 50, p. 2014-2027, 2011.

111. DAS, A.; TARAFDER, S. Experimental investigation on martensitic transformation and fracture morphologies of austenitic stainless steel. **International Journal of Plasticity**, n. 25, p. 2222-2247, 2009.

112. PARK, W. S. *et al*. Strain-rate effects on the mechanical behavior of the AISI 300 series of austenitic stainless steel under cryogenic environments. **Materials and Design**, v. 31, p. 3630-3640, 2010.

113. LEE, K. J. *et al*. A new constitutive model of austenitic stainless steel for cryogenic applications. **Computational Materials Science**, n. 46, p. 1152-1162, 2009.

114. DE, A. K. *et al*. Deformation-Induced Phase Transformation and Strain Hardening in Type 304 Austenitic Stainless Steel. **Metallurgical and Materials Transactions A**, v. 37A, p. 1875-1886, 2006.

115. CLARKE, K. D. *et al*. Effect of Strain Rate on the Yield Stress of Ferritic Stainless Steels. **Metallurgical and Materials Transactions A**, v. 39A, p. 752-762, 2008.

116. LESLIE, W. C. Iron and Its Dilute Substitutional Solid Solutions. **Metallurgical Transactions**, v. 3, p. 5-26, 1972.

117. HARDING, J. The Effect of High Strain Rate on Material Properties. In: BLAZYNSKI, T. Z. **Materials at High Strain Rates**. Elsevier Applied Science, 1987. Cap. 4, p. 133–187.

118. XU, L. *et al*. Forming limit and fracture mechanism of ferritic stainless steel sheets. **Materials Science and Engineering A**, n. 528, p. 3113-3121, 2011.

119. CURRY, D. A. Predicting the Temperature and Strain Rate Dependences of the Cleavage Fracture Toughness of Ferritic Steels. **Materials Science and Engineering**, n. 43, p. 135-144, 1980.

120. GAO, X.; DODDS, R. H. Constraint effects on the ductile-to-brittle transition temperature of ferritic steels: a Weibull stress model. **International Journal of Fracture**, n. 102, p. 43-69, 2000.

121. WAN, D.; BARNOUSH. Plasticity in cryogenic brittle fracture of ferritic steels: Dislocation versus twinning. **Materials Science & Engineering A**, n. 744, p. 335-339, 2019.

122. GIANG, N. A.; KÜNA, M.; HÜTTER, G. Influence of carbide particles on crack initiatio and propagation with competing ductile-brittle transition in ferritic steel. **Theorical and Applied Fracture Mechanics**, n. 92, p. 89-98, 2017.

123. KOVACH, C. W. **High-Performance Stainless Steels**. Canadá: Nickel Institute, 2000.

124. KON'KOVA, T. N.; MIRONOV, S. Y.; KORZNIKOV, A. V. Refining of Grains in Copper by Means of Cryogenic Deformation. **Metal Science and Heat Treatment**, v. 53, p. 95-100, 2011.

125. SORNIN, D. L.; KARCH, A.; LOGÉ, R. E. Competition between intragranular and intergranular deformation mechanisms in ODS ferritic steels during hot deformation at high strain rate. **Journal of Materials Science**, v. 53, p. 2965-2975, 2018.

126. BANDSTRA, J. P. *et al*. Modeling void coalescence during ductile fracture of a steel. **Materials Science and Engineering A**, n. 366, p. 269-281, 2004.

127. BANDSTRA, J. P.; KOSS, D. A. On the influence of void clusters on void growth and coalescence during ductile fracture. **Acta Materialia**, v. 56, p. 4429-4439, 2008.

128. CHAE, D.; KOSS, D. A. Damage accumulation and failure of HSLA-100 steel. **Materials Science and Engineering A**, n. 366, p. 299-309, 2004.

129. BENZERGA, A. A.; BESSON, J.; PINEAU, A. Anisotropic ductile fracture Part I: experiments. **Acta Materialia**, n. 52, p. 4623-4638, 2004.

130. GARRISON JR, W. M.; MOODY, N. R. Ductile Fracture. **Journal of Physics and Chemistry of Solids**, v. 48, n. 11, p. 1035-1074, 1987.

131. HÜTTER, G.; ZYBELL, L.; KUNA, M. Micromechanical modeling of crack propagation with competing ductile and cleavage failure. **Procedia Materials Science** , n. 3, p. 428-433, 2014.

132. OLSON, G. B.; COHEN, M. A General Mechanism of Martensitic Nucleation: Part I. General Concepts and FCC->HCP Transformation. **Metallurgical Transactions A**, v. 7A, p. 1897-1904, 1976.

133. KARIMI, M. B. *et al*. Effect of rolling strain on transformation induced plasticity of austenite to martensite in a high-alloy austenitic steel. **Journal of Materials Processing Technology**, n. 203, p. 349-354, 2008.

134. HEDAYATI, A. *et al*. The effect of cold rolling regime on microstructure and mechanical properties of AISI 304L stainless steel. **Journal of Materials Processing Technology**, n. 210, p. 1017-1022, 2010.

135. SHINTANI, T.; MURATA, Y. Evaluation of the dislocation density and dislocation character in cold rolled Type 304 steel determined by profile analysis of X-ray diffraction. **Acta Materialia**, v. 4314-4322, n. 59, 2011.

136. HEDSTRÖM, P. *et al.* Load Partitioning and Strain-Induced Martensite Formation during Tensile Loading of a Metastable Austenitic Stainless Steel. **Metallurgical and Materials Transactions A**, v. 40A, p. 1039-1048, 2009.